

Alma Mater Studiorum - Università di Bologna

DOTTORATO DI RICERCA IN
INGEGNERIA BIOMEDICA, ELETTRICA E DEI SISTEMI

Ciclo 36

Settore Concorsuale: 09/E4 - MISURE

Settore Scientifico Disciplinare: ING-INF/07 - MISURE ELETTRICHE E ELETTRONICHE

MEASUREMENT TECHNIQUES AND MODELS FOR INTEGRATED THERMAL
MANAGEMENT AND CONTROL IN ELECTRIC VEHICLE DESIGN

Presentata da: Luca Muratori

Coordinatore Dottorato

Michele Monaci

Supervisore

Lorenzo Peretto

Co-supervisore

Beatrice Pulvirenti

Raffaella Di Sante

Esame finale anno 2024

To my parents and my brother

Abstract

The continuous escalation in global pollution, largely driven by traditional gasoline-fueled vehicles, calls for an immediate transition towards more sustainable transportation alternatives. Electric vehicles (EVs) stand out as a viable solution, presenting a clean and environmentally-friendly remedy to the dire ecological issues at hand. Nonetheless, their broader acceptance is frequently hindered by the intrinsic constraint of a lesser driving range when compared to gasoline vehicles. A critical element influencing the driving range and overall efficacy of EVs is the performance of their thermal management system (TMS). An efficient TMS is crucial not only for ensuring passenger comfort but also for maintaining the operational efficacy of critical vehicular subsystems such as batteries and power electronics under diverse environmental conditions.

This study delves into the intricate thermal management challenges in electric vehicles, with a focal exploration of the Electric Thermal Management (e.TM) system. Aiming to augment vehicle efficiency, the e.TM system embodies a holistic approach, unifying traditional individual thermal regulation systems into a singular integrated entity. Central to this investigation is the impact of cabin air recirculation on HVAC energy consumption while ensuring safe CO₂ concentration levels, pursuant to the findings from real-time CO₂ measurements within a crane cabin. The innovative design of the e.TM system facilitates an adaptive thermal regulation mechanism, harmonizing the thermal needs of the passenger cabin, battery system, and PEEM/ECUs, thereby contributing to enhanced vehicle performance, especially under varying environmental conditions.

Through meticulous simulations using the Simscape platform, two distinctive layouts of the secondary loop were examined, focusing on the strategic positioning of the PEEM to optimize waste heat recovery. The findings underscored the potential benefits of a specific layout, particularly under colder environmental conditions. The introduction of an Intelligent Valve system, managed by a variable PI controller, showcased a dynamic regulation of the coolant loop configuration, thereby improving the responsiveness and accuracy in maintaining the desired coolant temperature across different vehicle subsystems.

Additionally, a Hardware-in-the-Loop (HIL) system was employed to amalgamate real heat pump testing with simulation models, providing a robust framework for evaluating the control logic of the thermal management system. Despite certain identified hardware limitations, the HIL system demonstrated the potential for accurate and efficient testing, thereby aiding the advancement of thermal management systems for electric vehicles.

Future research endeavors are delineated towards investigating the accuracy of CO₂ sensors used, the impact on HVAC system energy consumption, and exploring cost-effective sensor solutions. The comprehensive insights garnered from this study accentuate the pivotal role of integrated thermal management systems like e.TM, in propelling the electric vehicle industry towards achieving better efficiency, comfort, and safety, which are instrumental in addressing the range anxiety concerns and fostering broader acceptance of EVs in the quest for a greener future.

Sommario

L'escalation continua dell'inquinamento globale, in gran parte guidata dai veicoli tradizionali alimentati a benzina, richiede una transizione immediata verso modalità di trasporto più sostenibili. I veicoli elettrici (EV) si distinguono come soluzione valida, presentando un rimedio pulito ed ecologico alle gravi questioni ecologiche attuali. Tuttavia, la loro accettazione più ampia è spesso ostacolata dalla limitazione intrinseca di un'autonomia di guida inferiore rispetto ai veicoli a benzina. Un elemento critico che influisce sull'autonomia di guida e sull'efficacia complessiva degli EV è la performance del loro sistema di gestione termica (TMS). Un TMS efficiente è fondamentale non solo per garantire il comfort dei passeggeri, ma anche per mantenere l'efficacia operativa di sottosistemi veicolari critici come le batterie e l'elettronica di potenza in diverse condizioni ambientali.

Questo studio si addentra nelle complesse sfide di gestione termica nei veicoli elettrici, con un'esplorazione focalizzata del sistema Electric Thermal Management (e.TM). Mirando ad aumentare l'efficienza del veicolo, il sistema e.TM incarna un approccio olistico, unificando i tradizionali sistemi di regolazione termica individuali in un'entità integrata singola. Centrale in questa indagine è l'impatto della ricircolazione dell'aria dell'abitacolo sul consumo energetico dell'HVAC, garantendo al contempo livelli sicuri di concentrazione di CO₂, conformemente ai risultati delle misurazioni di CO₂ in tempo reale all'interno di una cabina gru. Il design innovativo del sistema e.TM facilita un meccanismo di regolazione termica adattiva, armonizzando le esigenze termiche dell'abitacolo dei passeggeri, del sistema batteria e dei PEEM/ECU, contribuendo così a migliorare le prestazioni del veicolo, specialmente sotto diverse condizioni ambientali.

Attraverso meticolose simulazioni utilizzando la piattaforma Simscape, sono stati esaminati due layout distintivi del circuito secondario, concentrandosi sulla posizione strategica del PEEM per ottimizzare il recupero del calore di scarto. I risultati hanno sottolineato i potenziali benefici di un particolare layout, in particolare in condizioni ambientali più fredde. L'introduzione di un sistema di valvole intelligenti, gestito da un controller PI variabile, ha mostrato una regolazione dinamica della configurazione del circuito di refrigerante, migliorando così la reattività e l'accuratezza nel mantenere la temperatura del refrigerante desiderata attraverso diversi sottosistemi del veicolo.

Inoltre, è stato impiegato un sistema Hardware-in-the-Loop (HIL) per amalgamare test reali della pompa di calore con modelli di simulazione, fornendo un framework robusto per valutare la logica di controllo del sistema di gestione

termica. Nonostante alcune limitazioni hardware identificate, il sistema HIL ha dimostrato il potenziale per test accurati ed efficienti, contribuendo così a promuovere i sistemi di gestione termica per i veicoli elettrici.

Le future ricerche sono delineate verso l'indagine sull'accuratezza dei sensori di CO₂ utilizzati, l'impatto sul consumo energetico del sistema HVAC, ed esplorando soluzioni di sensori economiche. Le intuizioni complete ottenute da questo studio accentuano il ruolo fondamentale dei sistemi di gestione termica integrati come e.TM, nel propellere l'industria dei veicoli elettrici verso il raggiungimento di una migliore efficienza, comfort e sicurezza, che sono fondamentali per affrontare le preoccupazioni relative all'autonomia e promuovere una più ampia accettazione degli EV nella ricerca di un futuro più verde.

Contents

List of Figures	xv
List of Tables	xix
List of Acronyms	xxi
1 Introduction	1
2 Background on electric vehicle thermal management systems	5
2.1 Heating Ventilation and Air Conditioning systems	6
2.1.1 Vehicle Cabin Climate Control: Thermal, Humidity, and Air Quality Requirements	6
2.1.2 Traditional HVAC system	8
2.1.3 Heat pump air conditioning systems	10
2.2 Battery thermal management systems	13
2.3 Electric motor thermal management systems	14
2.4 Integrated thermal management systems	16
2.4.1 Design Considerations	16
3 In-cabin CO₂ measurement	19
3.1 Experimental set-up	21
3.2 Automatic air recirculation control strategy to improve energy efficiency	26
3.3 Assessment of the Optimal CO ₂ Sensor Position	28
3.4 Determination of the measurement uncertainty of the leakage flow	29
3.4.1 Application of the MCM	30
3.4.2 Parameters of the test	33
3.5 Results	34

CONTENTS

3.5.1	Assessment of energy saving due to the automatic air re-circulation control strategy	35
3.5.2	Evaluation of the optimal CO ₂ sensor position	39
3.5.3	Results of the Monte Carlo Method applied on indirect measurements	45
3.6	Discussion	49
4	Design of the ITMS	51
4.1	Integrated thermal management concept	52
4.2	Model of the vehicle	55
4.2.1	PEEM subsystem	55
4.2.2	Battery subsystem	60
4.2.3	Cabin subsystem	62
4.3	Components of the ITMS	67
4.4	PEEM placement optimization	68
4.4.1	Test condition	70
4.4.2	Results	72
4.4.3	Discussion	75
4.5	Layout of the ITMS	76
5	Control strategy	79
5.1	Working mode selection	79
5.2	Heat pump control system	82
5.2.1	Methods	84
5.2.2	Set-up	85
5.2.3	Results	87
5.2.4	Discussion	88
6	Hardware in the Loop system	91
6.1	HARDWARE-IN-THE-LOOP SIMULATION	92
6.1.1	Simulation environment	93
6.1.2	Test bench	94
6.1.3	Data exchange and control logic	96
6.2	Test conditions	99
6.3	Results	100
6.4	Discussion	104

CONTENTS

7 Conclusions	107
References	111
Acknowledgments	121

List of Figures

2.1	Scheme of a traditional Heating Ventilation and Air Conditioning (HVAC) system with a PTC air heater	11
2.2	Scheme of a traditional HVAC system with a PTC water heater	11
2.3	Changes in COP based on different heat pump configurations and refrigerants at varying ambient temperatures [12].	12
3.1	Schematic representation of the CO ₂ sensors positions inside the crane cabin	25
3.2	Schematic representation of the vent positions. The red arrows indicate the working vents in heating mode. The blue arrows indicate the working vents in cooling mode.	28
3.3	CO ₂ concentration, power absorbed by the HVAC system and cabin temperature measurements at ambient temperature equal to 10 °C	37
3.4	CO ₂ concentration, power absorbed by the HVAC system and cabin temperature measurements at ambient temperature equal to 15 °C	38
3.5	CO ₂ concentration, power absorbed by the HVAC system and cabin temperature measurements at ambient temperature equal to 23 °C	40
3.6	CO ₂ concentration, power absorbed by the HVAC system and cabin temperature measurements at ambient temperature equal to 30 °C	41
3.7	Vertical stratification of the CO ₂ in the breathing zone.	42
3.8	CO ₂ concentration measurements acquired from the 9 sensors that were installed in the cabin compartment in heating mode	43

LIST OF FIGURES

3.9	CO ₂ concentration measurements acquired from the 9 sensors that were installed in the cabin compartment in ventilation mode	44
3.10	CO ₂ concentration measurements acquired from the 9 sensors that were installed in the cabin compartment in cooling mode	44
3.11	Illustration of the propagation of distribution for the input quantities obtained by the application of the MCM in test #1c	46
3.12	Illustration of the propagation of distribution for the input quantities obtained by the application of the MCM in test #2c.	47
4.1	Integrated thermal management system for a 5 m electric bus equipped with 2 Webasto CV (commercial vehicle) standard battery.	53
4.2	Scheme of the secondary loop concept	54
4.3	PEEM model	56
4.4	Battery model	61
4.5	Cabin model	63
4.6	Schematic representation the two different collocations of the PEEM subsystem that are analysed.	69
4.7	Worldwide harmonized Light duty Test Cycle.	71
4.8	Comparison of the recovered power from the PEEM subsystem, between the two secondary loop layouts. These data are showed for the case of environment temperature equal to 0 °C.	73
4.9	Comparison of the evolution in time of the cabin temperature, between the two secondary loop layouts. The data are showed in the cases of environment temperature (T_{env}) equal to 0 °C, 5 °C and 10 °C.	74
4.10	Comparison of the evolution in time of the battery temperature, between the two secondary loop layouts. The data are showed in the cases of environment temperature (T_{env}) equal to 0 °C, 5 °C and 10 °C.	75
4.11	ITMS layout	78
5.1	Example of a EVTMS shifting from cabin cooling to cabin and battery cooling	83
5.2	Test layout.	85
5.3	Tuning of the controller parameters imposing steps on the target coolant temperature at the evaporator outlet.	87

5.4	Performance comparison between the standard PI controller and the variable PI controller.	89
6.1	Illustration of the vehicle thermal management system	92
6.2	Layout of the HIL system. The sensors are identified as T = temperature, P = pressure, V = volume flow rate, TP = temperature and pressure (a single sensor that measures both quantities).	95
6.3	Communication scheme of the HIL system	97
6.4	Interface between the test bench and the simulation environment at the outlet of the condenser and evaporator. $T_{c,o,s}$ and $T_{c,o,m}$ are respectively the coolant temperature at the condenser outlet computed in the simulation environment and measured on the test bench. $T_{e,o,s}$ and $T_{e,o,m}$ are respectively the coolant temperature at the evaporator outlet computed in the simulation environment and measured on the test bench.	101
6.5	Interface between the test bench and the simulation environment at the inlet of the condenser and evaporator. $T_{c,i,s}$ and $T_{c,i,m}$ are respectively the coolant temperature at the condenser inlet computed in the simulation environment and measured on the test bench. $T_{e,i,s}$ and $T_{e,i,m}$ are respectively the coolant temperature at the evaporator inlet computed in the simulation environment and measured on the test bench.	101
6.6	Evolution during the test of the cabin temperature (T_{cab}) and battery temperature (T_{bat}). T_{amb} represents the ambient temperature considered in the simulation environment.	102
6.7	Comparison between the thermal power exchanged computed in the simulation environment and measured on the test bench through the condenser ($W_{c,s}$ and $W_{c,m}$) and the evaporator ($W_{e,s}$ and $W_{e,m}$).	102
6.8	Regulation of the electric heater to maintain the target coolant temperature at the evaporator inlet on the test bench.	103
6.9	Regulation of the radiator fans to maintain the target coolant temperature at the condenser inlet on the test bench.	103

List of Tables

3.1	Settings of the climatic wind tunnel and of the HVAC system for the tests executed in the evaluation of the energy saved thanks to the implementation of a controlled outside air induction.	27
3.2	Settings of the climatic wind tunnel and of the HVAC system for the tests executed in the evaluation of the optimal CO ₂ sensor positioning.	30
3.3	Settings of the climatic wind tunnel and of the HVAC system for the analysis made with the MCM.	34
3.4	Errors relative to the input quantities for test #1c and test #2c. . .	34
3.5	Values of $\bar{\Delta}_i$ (expressed in [%]) for CO ₂ sensors 1 to 5.	42
3.6	Results from test #1c using MCM.	45
3.7	Results for input variables from test #2c using MCM.	48
3.8	Results for the output variable from test #2c using MCM.	48
4.1	Energy consumed and time required values to reach the cabin and battery target temperatures.	74

List of Acronyms

EV Electric Vehicle

HEV Hybrid Electric Vehicle

TMS Thermal Management System

EVTMS Electric Vehicle Thermal Management System

HVAC Heating Ventilation and Air Conditioning

AC Air Conditioning

BTMS Battery Thermal Management System

BTM Battery Thermal Management

PEEM Power Electronics and Electric Motor

ITMS Integrated Thermal Management System

PTC Positive Temperature Coefficient

HP Heat Pump

COP Coefficient of Performance

HPAC Heat Pump Air Conditioning

PCM Phase Change Material

ADAS Advanced Driver Assistance System

HIL Hardware-in-the-Loop

GWP Global Warming Potential



Introduction

In times there has been a growing popularity of electric vehicles (EVs) as an alternative to traditional fuel-powered vehicles. This change is mainly driven by concerns, including the urgent requirement to reduce carbon dioxide (CO₂) emissions and mitigate the harmful effects of climate change. Electric vehicles produce zero emissions from their tailpipes, which can greatly improve the quality of air in urban areas. Electric powertrains often have a higher efficiency compared to internal combustion engines, offering the potential for reduced energy consumption on a per-mile basis.

However, despite the advantages of EVs, they do come with their own set of challenges. One major drawback is the reduced driving range offered by EVs, compared to traditional fuel-powered vehicles. This discrepancy can be attributed to the substantial difference in energy density between the energy storage systems of these two technologies. While a gasoline tank boasts an energy density of approximately 8.76 kWh/l, a lithium-ion battery pack achieves only around 0.4 kWh/l. Moreover, the extended charging times required for EVs, though mitigated by fast charging options, can accelerate the degradation of lithium-ion batteries [1]. Consequently, frequent fast charging is discouraged to ensure battery longevity. There are concerns about the longevity and sustainability of battery technology due, to the quantities of earth elements required and the environmental impact associated with their extraction.

Increasing the driving range by installing larger battery packs seems intuitive, but it comes at the cost of increased vehicle weight and expense. A more pragmatic approach lies in enhancing the energy efficiency of EVs. This

challenge revolves around developing a sophisticated Thermal Management System (TMS) specifically designed for EVs. As demonstrated by Lee et al. [2], the air conditioning, encompassing both cooling and heating, is generally responsible for about a 33% average decrease in driving range for EVs. Similar results were also obtained by other researchers [3][4], with vehicle range drops up to 30%/40%, for temperatures below freezing. In particular, the driving range of an EV is more penalized by the activity of the thermal management system in cold conditions, with respect to a fuel powered vehicle [5]. The reason is that the electric motor does not generate exhaust gasses that can be used to heat up the vehicle cabin. Therefore, the energy needed to heat up the vehicle is mainly taken from the battery pack. Hence, improving the efficiency of this auxiliary system can result in an extended driving range and a decrease in the battery's size and weight. However, designing thermal management systems for EVs is inherently more complex than for fuel-powered vehicles, as they must cater to additional components that require thermal regulation [6]. Aside from providing passenger comfort through Heating, Ventilation, and Air Conditioning (HVAC) heat exchangers, the system must also maintain the battery pack and Power Electronics and Electric Motor (PEEM) within their optimal thermal working conditions. In particular, it is crucial to maintain an optimal operating temperature for the battery as it directly affects its performance, efficiency, safety, and lifespan [7]. The thermal management system has to ensure that the battery operates within a temperature range maximizing its performance while minimizing risks associated with overheating or insufficient cooling [8].

Considering these factors, this thesis aims to explore the development of an Integrated Thermal Management System (ITMS) for EVs with the aid of mathematical models that describe the physical behavior of these systems for simulation purposes.

The thesis was carried out in collaboration with Webasto Thermo & Comfort Italy s.r.l. and its structure unfolds as follows: Chapter 2 delves into the background of TMS for EVs, emphasizing the thermal management across various vehicle subsystems—namely the cabin, battery, power electronics, and electric motor. This chapter also explores the integration of these subsystems. Chapter 3 presents an experimental study evaluating the energy savings derived from an automatic air recirculation control strategy. This strategy is based on in-cabin CO₂ concentration levels, and the chapter further elucidates the methodology behind CO₂ measurement to enhance in-vehicle air quality management. In

Chapter 4, readers are introduced to the thermodynamic model of the ITMS and insights into its layout optimization. The subsequent chapter, Chapter 5, delineates the control system while showcasing the findings from dynamic simulations. In Chapter 6, the vehicle thermal management system's Hardware-in-the-Loop (HIL) simulation is demonstrated, featuring the heat pump as the hardware component. Finally, Chapter 7 synthesizes the study, drawing overall conclusions.



Background on electric vehicle thermal management systems

The Electric Vehicle Thermal Management System (EVTMS) generally consists of Heating Ventilation and Air Conditioning HVAC system, Battery Thermal Management System (BTMS), and PEEM TMS. The PEEM is comprised of the drive motor and the electronic components needed for vehicle traction and battery charging, like inverter, DC/DC converter, and charger. The three factors of the EVTMS directly affect the total energy consumption of pure electric vehicles (EVs). A good TMS not only improves the energy efficiency of the vehicle but also extends the service life of major parts. Therefore, EVTMS has increasingly become one of the key technologies for the development of the automotive industry.

Temperature control of the cabin is done through the Heating Ventilation and Air Conditioning (HVAC) system. Currently, the HVAC systems of EVs are mostly conventional, and only a few of them have started to use Heat Pump Air Conditioning (HPAC) systems. Regarding the BTMS, there are many different types of TMS depending on the heat transfer medium. They are mainly divided into air-cooled TMS, liquid-cooled TMS, and phase change material-cooled TMS. The PEEM cooling system of EVs can be divided into air-cooled and liquid-cooled types according to the cooling medium. As the power of drive motors increases, liquid coolant is frequently used in cooling systems.

If during the designing of the EVTMS, each subsystem is considered independent of the other, we obtain a simple design of the TMS. However, the

2.1. HEATING VENTILATION AND AIR CONDITIONING SYSTEMS

disadvantages of this solution are the high cost of the system and the inability to recycle the waste heat coming from electronic components. Integrating the HVAC system, the BTMS, and the PEEM TMS can improve the above disadvantages. Therefore, the development of an ITMS for electric vehicles is very important.

2.1 HEATING VENTILATION AND AIR CONDITIONING SYSTEMS

The purpose of HVAC systems is to provide a comfortable driving experience for the driver and passengers. They usually execute the functions of air conditioning, heating, filtration, dehumidification, windshield defogging and defrosting.

2.1.1 VEHICLE CABIN CLIMATE CONTROL: THERMAL, HUMIDITY, AND AIR QUALITY REQUIREMENTS

Maintaining a comfortable and safe environment within a vehicles cabin is not just a matter of convenience or luxury; it is integral to the safety and health of the passengers. The cabin climate control system must address three critical aspects: thermal comfort, humidity levels, and air quality. This section elaborates on the necessary requirements in each of these domains to ensure an optimal and comfortable environment for vehicle occupants.

THERMAL COMFORT

Thermal comfort within a vehicle's cabin refers to the sensation of satisfaction or dissatisfaction concerning the surrounding air temperature. It depends on several factors:

- **Ambient Temperature:** The exterior temperature greatly influences the cabin's temperature. Depending on the region and the time of the year, vehicles may need to cope with extremely high or low temperatures.
- **Solar Radiation:** Direct exposure to sunlight, especially in parked vehicles, can cause cabin temperatures to soar, making immediate cooling imperative upon starting the vehicle.
- **Occupant Metabolism:** Passengers in the vehicle produce heat. This is especially significant when there are several occupants.

To address these concerns, vehicle climate control systems employ sensors and responsive mechanisms to adjust the cabin temperature, ensuring it remains within a comfortable range for the occupants, typically between 20 °C and 24 °C.

HUMIDITY CONTROL

Maintaining the right level of humidity in the vehicle's cabin is crucial for several reasons:

- **Comfort:** High humidity can make occupants feel clammy and uncomfortable, while low humidity can lead to dry skin and irritation.
- **Visibility:** High humidity can cause the windows to fog up, impairing the driver's visibility and posing a safety risk.
- **Health:** Maintaining appropriate humidity levels reduces the growth potential of mold, bacteria, and other pathogens that thrive in overly humid or dry environments.

Typically, a relative humidity level between 40% and 60% is considered comfortable and safe for vehicle cabin environments.

AIR QUALITY

Maintaining optimal air quality inside a vehicle's cabin is essential for the well-being and ease of its occupants:

- **Pollutants:** Particularly in city environments, vehicles might encounter a range of outdoor pollutants such as carbon monoxide, nitrogen oxides, and fine particles. Effective filtering systems are essential to keep these pollutants out.
- **Odors:** Unpleasant odors, whether from outside sources or from within the vehicle, can be distracting and uncomfortable. Advanced air filtration and ventilation systems can help in minimizing such odors.
- **CO₂ Levels:** With occupants breathing inside the closed environment of a vehicle, CO₂ levels can rise. Increased levels of CO₂ can lead to fatigue and hinder cognitive abilities. Contemporary vehicles come with systems that track and manage CO₂ concentrations, ensuring they stay under the 1000 ppm limit.

In summary, recognizing and catering to the temperature, moisture, and air quality necessities inside a vehicle's cabin is crucial for the well-being, health, and protection of the passengers. Sensors and control systems, along with an appropriate design of the TMS, are central to realizing these objectives.

2.1. HEATING VENTILATION AND AIR CONDITIONING SYSTEMS

2.1.2 TRADITIONAL HVAC SYSTEM

Traditional HVAC systems for EVs consist only of vapor compression refrigeration systems for cooling (air conditioning) and Positive Temperature Coefficient (PTC) heaters for heating the cabin air. This is an easy way to control the temperature inside the vehicle and the model is similar to the HVAC system of traditional fuel-powered cars.

VAPOR COMPRESSION REFRIGERATION SYSTEM

The vapor compression refrigeration system consists of a compressor, expansion valve, condenser, and evaporator. Generally, the condenser is located outside the cabin, while the evaporator is located inside the cabin. The fundamental objective of this system is to remove heat from a designated space or substance and discharge it elsewhere, typically into the environment. Below is a concise description of this cycle:

- **Compression:** The cycle starts with the low-pressure, low-temperature, superheated vapor refrigerant entering the compressor. In this stage, the refrigerant goes through a compression, which increases its temperature and pressure. After this step, the refrigerant leaves the compressor in the form of a high-temperature, high-pressure vapor.
- **Condensation:** Following this, the heated refrigerant vapor moves to the condenser. Here, it typically gives off heat to the external environment. While relinquishing this heat, the refrigerant changes state, transitioning from a vapor to a liquid, all the while maintaining its high temperature and pressure.
- **Expansion:** This high-pressure liquid refrigerant next enters the expansion valve. Here, the refrigerant undergoes a sudden pressure drop, leading to a significant reduction in its temperature. The refrigerant leaves the expansion valve as a mixture of low-pressure liquid and vapor.
- **Evaporation:** The mixture, now at a low pressure, proceeds to the evaporator. In this component, it draws heat from the environment intended to be cooled. As the refrigerant takes in this heat, it evaporates completely, transitioning into a vapor state with low pressure and temperature. This cooled vapor then circulates back to the compressor, marking the start of the cycle once again.

We can control the cabin temperature by regulating the compressor and fan speed, which blows the cool air into the cabin. The compressor is the main energy-consuming component of the air conditioner.

In a conventional ICEV, the compressor is connected to the engine via a clutch. Therefore, the compressor speed is fixed in proportion to the engine speed and cannot be adjusted as necessary. Since in EVs the compressor is driven by an electric motor, its speed can be adjusted according to the actual needs. For this reason, many researchers have focused on the control of the AC system of EVs in order to save energy while increasing comfort in the vehicle. Generally speaking, control approaches can be divided into four types: on/off control, proportional integral derivative (PID) control, fuzzy control and optimization-based control. On/off controllers are one of the simplest and most widely used control methods. When the cabin temperature is higher than the desired temperature, the compressor turns on to cool down the cabin and turns off when the desired temperature is reached. However, temperature control via on/off switching is not precise and can cause large changes in cabin temperature when the compressor is turned on and off. The PID controller is another widely used control method in EV AC due to its high accuracy and fast response. However, PID controller has disadvantages in terms of robustness and not easy prediction of the effects caused by non-linear parameters such as vehicle speed, sunlight, temperature. Although the control accuracy of fuzzy control is low, it can solve the PID controller problem. A fuzzy-PID controller, which combines fuzzy and PID control methods, has been proposed to improve the control performance of the AC system, but its disadvantages in terms of computational cost cannot be ignored. A two-layer control strategy based on fuzzy-PID algorithm is proposed by Xi et al. to adjust the compressor speed to achieve the target temperature inside the EV. Compared with on/off and PID controllers, the proposed algorithm saves 30.2% and 12.4% energy, respectively. With the development of artificial intelligence in EVs, many control strategies based on optimization-based controllers have been developed in AC systems. Linear quadratic model predictive controller (LMPC), nonlinear model predictive controller (NMPC), reinforcement learning (RL) based controllers have been introduced to control EV AC to save energy. A control strategy based on genetic algorithm optimization was developed by Huang et al. to control the compressor speed. Compared to PID and engineering-applied controllers, the energy consumption of air conditioners using this strategy is said to be reduced by 5.3% and 3.9% respectively.

2.1. HEATING VENTILATION AND AIR CONDITIONING SYSTEMS

PTC HEATER

The PTC heaters are widely used in the automotive industry for their simple structure and control, and low price. Also known as self-regulating heater [9], the PTC heating element consists of an electric resistance heater whose resistance increases significantly with temperature. Therefore, if a constant voltage is applied, the element produces a large amount of heat when its temperature is low, and a smaller amount of heat when its temperature is high. In this way, the heater is able to self-regulate the output power to maintain a fixed temperature, even if the heat load changes. The equilibrium temperature depends on the heating element's material and the applied voltage.

This is the most common type of heating element used in electric vehicles. However, since the heating efficiency is lower than 1, a lot of battery power is used for heating in winter. In a study published by Chowdhury et al. [10], they simulated an electric Fiat 500e running on the Multi-Cycle Test (MCT) drive cycle at an ambient temperature of $-10\text{ }^{\circ}\text{C}$. They obtained a driving range of 174.9 km with the auxiliary heating system off against a driving range of 117.6 km with the usage of a 5 kW PTC air heater to heat up the cabin to the setpoint temperature of $22\text{ }^{\circ}\text{C}$. Therefore, this result showed a driving range reduction of 33%.

The electric heaters adopted in EVs can be divided into two types: PTC air heaters and PTC water heaters based on PTC electric heating method. Figure 2.1 is a schematic representation of a traditional HVAC system with a PTC air heater. In this case, the heater uses electricity to directly heat the air. Its structure is simple and the heating temperature is high, but setting up PTC heater with high voltage and high current inside the cabin poses a significant risk to occupants safety. Figure 2.2 represents the layout of a HVAC system with a PTC water heater. The PTC water heater uses electric heating elements to heat the coolant. Then, through a heat exchanger, the air is heated by the warm coolant. Although the safety factor is higher, the system is more complicated and, because the coolant acts as an intermediate heat transfer medium, the heat losses are higher and the heating temperature is lower.

2.1.3 HEAT PUMP AIR CONDITIONING SYSTEMS

While there have been initiatives to enhance the thermal performance of PTC heaters, their Coefficient of Performance (COP) invariably remains less

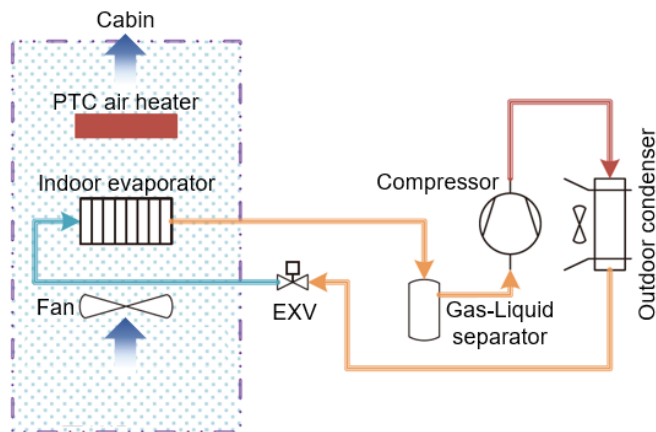


Figure 2.1: Scheme of a traditional HVAC system with a PTC air heater

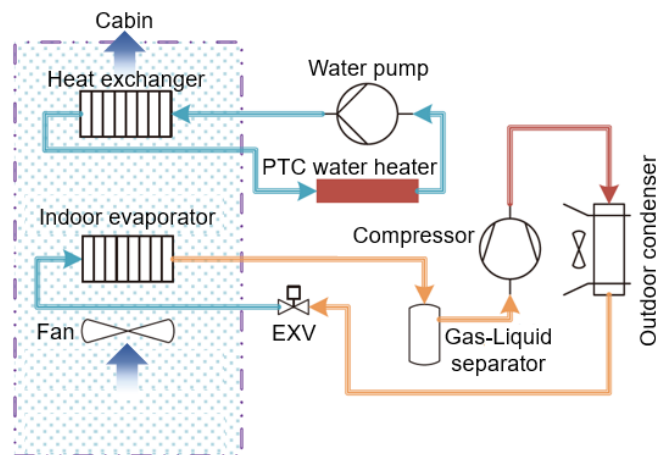


Figure 2.2: Scheme of a traditional HVAC system with a PTC water heater

than or equal to 1. This results in significant power usage, amplifying concerns regarding driving range. Thus, employing heat pumps (HPs) with a superior COP for EV heating has been advocated.

REVERSIBLE HEAT PUMP

The underlying mechanism of HP is essentially an inverted AC circuit. This allows the merging of the HP and AC systems into a unified HPAC system. As opposed to a standalone AC system, the HPAC requires merely an additional four-way reversing valve to change the refrigerant flow direction. This makes HPAC a more streamlined system compared to the combination of AC and PTC heaters. Moreover, the HP harnesses external heat to warm the cabin, allowing its COP to surpass 1. It's documented by Li et al. [11] that EVs incorporating

2.1. HEATING VENTILATION AND AIR CONDITIONING SYSTEMS

HP heating observed a 23% extension in driving range in comparison to those with PTC heaters, particularly in conditions of $-10\text{ }^{\circ}\text{C}$. Yu et al. [12] studied the energy consumption for cabin heating using three distinct heat pump systems and evaluated five refrigerants (R134a, R1234yf, R290, R744, R152a). Their experiments were conducted in a climatic wind tunnel laboratory using the Worldwide harmonized Light-duty vehicle Test Cycle (WLTC) protocol. When benchmarked against a PTC heating system, their findings demonstrated energy savings ranging from 41% to 72% across various scenarios. This led to an enhancement in driving range by 14.2% to 31%. The COP values that they obtained under three different ambient temperatures are shown in Figure 2.3.

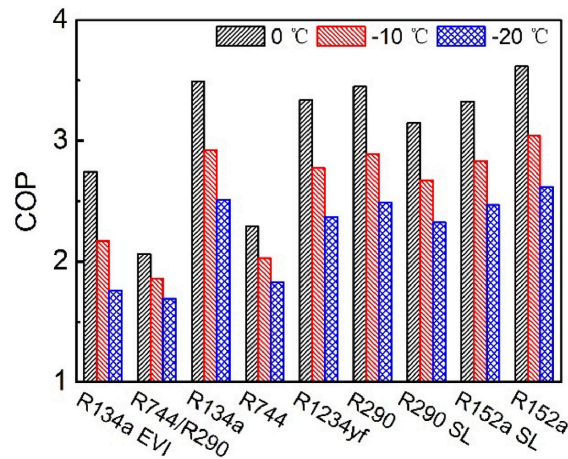


Figure 2.3: Changes in COP based on different heat pump configurations and refrigerants at varying ambient temperatures [12].

As such, the development of HPAC systems has become a focal point in recent EV advancements. Yet, challenges persist.

One issue with EV HPs revolves around the frost buildup on the external surface of the out-cabin heat exchanger in HP mode. The accumulation of this frost layer impedes efficient heat transfer and airflow, compromising the system's efficiency. Several defrosting strategies have been introduced, including electric heating [13],[14], hot gas distribution, [15], [16], and reverse cycle approaches [17], [18], [19], [20], each presenting distinct advantages and limitations.

Another challenge is that HPs can exhibit decreased heating performance in extremely cold ambients. A reduced evaporating temperature results in decreased density at the compressor's intake, and a heightened compression pressure ratio contributes to diminished volumetric efficiency. Consequently, the system's mass flow rate significantly decreases, and the exit temperature

elevates well beyond typical levels. Several innovations, such as the incorporation of waste heat, PTC-backed heating, and vapor-injection mechanisms have been suggested to address these challenges. For instance, integrating waste heat from the powertrain with the HP has shown promise, and this is elaborated upon in Section 2.4. Vapor injection technologies, differentiated by their intermediate stages, come in two primary forms: the economizer and the flash tank system. Within the economizer, refrigerant from the intermediate stage gets divided at the outlet of the condenser, then throttled and superheated within the economizer, prior to being channeled into the compressor's intermediate stage. Conversely, in the flash tank arrangement, refrigerant initially traverses the initial throttling stage post condenser, and subsequently undergoes vapor-liquid separation in the flash tank. The vapor portion progresses into the intermediate compressor stage, whereas the liquid segment advances to the evaporator following a secondary throttling, for evaporation purposes. The vapor's entry into the intermediate compressor stage aids in amplifying the refrigerant flow rate within the condenser, thereby boosting the heating capacity of HP. Concurrently, the vapor refrigerant's temperature within the compressor is moderated by the injected vapor, circumventing potential irreversible damage from compressor overheating.

In terms of refrigerants, R134a has been predominantly used in most EVs. However, its high Global Warming Potential (GWP) of 1300 has led to investigations into alternative refrigerants. Zou et al. [21] posited the use of R1234yf as a more eco-friendly substitute. More recently, natural CO₂ has also emerged as a potential replacement due to its lower GWP and robust heating performance in colder environments [22].

2.2 BATTERY THERMAL MANAGEMENT SYSTEMS

The performance and lifespan of a battery are significantly influenced by its operating temperature. Working in an excessively hot or cold environment could reduce the electrical energy produced and shorten the battery's lifespan. When the temperature drops [23], [24], [25], it has been shown that the discharge capacity and voltage of the lithium-ion battery are significantly reduced. Low temperatures also weaken the diffusion capability of Li-ion in graphite and the reaction rate on the graphite's surface, resulting in decreased battery performance due to increased internal resistance and enhanced electrical polarization.

2.3. ELECTRIC MOTOR THERMAL MANAGEMENT SYSTEMS

However, high temperatures can also damage the battery, as they too lead to an increase in internal resistance and a reduction in voltage, thus decreasing the battery's output power and overall lifespan. Furthermore, high operating temperatures can trigger exothermic reactions between the electrolyte and electrode, increasing the battery's temperature and posing a risk of explosion. For optimal performance and lifespan, the battery should operate within a temperature range of 25 °C to 40 °C [26], while the internal temperature of the battery pack should be kept within 5 °C [26][27]. In case of operation outside the operating range the vehicle control system can reduce the current or activate the cooling / heating system of the batteries. This system requires energy itself from the battery with a consequent reduction in vehicle range [28] [29].

The most commonly used cooling methods in Battery Thermal Management (BTM) are currently air and liquid cooling. Air cooling is simpler and more economical, and is mainly used for Hybrid Electric Vehicles (HEVs) with low heat dissipation requirements because the heat transfer coefficient of air is low. Liquid cooling is superior to air cooling but requires precautions against potential liquid leak issues. A passive cooling method is the Phase Change Material (PCM), as it doesn't need additional electrical energy, but due to its reduced thermal conductivity, it can result in uneven battery temperature distribution and diminished thermal capacity. The heat pipe is favored by BTM for its high thermal conductivity and flexible positioning, but it requires further research. Batteries can be pre-heated during cold starts either through external warming or self-heating: the former is more well-known, while the latter is more sought-after because it uses less energy and fewer auxiliary parts. However, there isn't yet a standardized method for a specific battery.

2.3 ELECTRIC MOTOR THERMAL MANAGEMENT SYSTEMS

In electric vehicles, Permanent Magnet Synchronous Motors (PMSMs) are widely used because they have the advantage of high power density, simple structure, high power factor, and excellent control performance. The motor fundamentally serves as a device that converts electrical energy into mechanical energy to propel the vehicle. In the course of its operation, the motor will experience losses, predominantly manifested as heat, which disperses to different sections of the motor. Studies have indicated that when the temperature rises from 40 °C to 160 °C [30], there's a linear increase in phase resistance and a de-

crease in the back electromotive force coefficient for a brushless electric vehicle. This suggests a decline in the motor's efficiency at elevated temperatures. High temperatures also cause the demagnetization of the permanent magnet that uses electromagnetic fields to convert electrical energy into mechanical energy. Once demagnetization occurs, it is irreversible, resulting in reduced motor life.

The PEEM system of the vehicles operates within a maximum temperature limit and consequently requires a cooling system [31]. Research on Motor Thermal Management (MTM) focuses solely on cooling modes using air and liquid. Other methods such as PCM, heat pipe, and Peltier effect remain in the experimental phase. Air cooling is structurally simple and economical. We have two types of air cooling for Electric Motor (EM): natural convection and forced convection depending on whether we use a fan or not. In natural convection, Asef et al.[32] link the circumferential and axial channels in an air-cooled Permanent magnet synchronous motor (PMSM) in order to reduce the temperature increase of the stator core due to shaft rotation. For better coil cooling, Hyeon et al. [33] inserted flow deflectors at the end of the channel, resulting in simulations showing both a reduction in coil temperature and a reduction in air pressure drop. Forced convection air cooling has superior cooling capacity compared to natural convection. Several studies have been performed to improve the heat transfer of forced convection air cooling, for example through the optimization of fins [34], increasing their number from 6 to 8, and also by equipping a high-speed induction motor with auxiliary fans placed on both sides of the air gap on the shaft [35]. Regarding liquid cooling, it is superior to air: the liquids used are water [36],[37][38] and oil [39],[40],[41]. Water is the most commonly used refrigerant due to its low cost and high thermal capacity. Cooling takes place through water jackets on the motor, but it cannot penetrate central areas, such as coils, resulting in higher local temperatures inside the motor. To improve the cooling conditions of the internal parts of the EM, a dual-cycle cooling method was proposed: air and water [17]. In oil cooling, it is sprayed onto the cores of the stator and rotor through channels, taking advantage of rotational forces and gravity [41], with a reduction in the temperature of the bearings and the resolver. Using the same channel, the water-based MTM is more efficient than the oil-based one because the oil has a higher viscosity, and therefore the oil feed pump must use more energy.

2.4 INTEGRATED THERMAL MANAGEMENT SYSTEMS

The design of an ITMS (Integrated Thermal Management System) that utilizes energy from every part of the EV, such as the waste heat from the power electronics and the electric motor to heat the cabin in winter, is essential. This not only saves energy for cabin heating but also addresses the issue of battery heat dissipation.

2.4.1 DESIGN CONSIDERATIONS

The design involves integrating several systems: either on the air side or on the refrigerant side.

AIR-SIDE INTEGRATION SYSTEMS

In air-side integration systems, the simpler option, there are two types of schemes: internal and external cabin integration. In internal cabin integration, the battery pack is connected in series with the cabin air and placed inside the cabin. This is unfeasible for EVs with large battery packs. Furthermore, this system can lead to uneven temperature distribution within the battery pack due to the low heat transfer coefficient of air. To overcome this, Xie et al. [42] introduced porous channels for airflow between the batteries and organized PCM on the batteries themselves. For air-side integration systems outside the cabin, heat exchangers should be connected in a certain order, and in general, heat exchangers for higher temperature systems should be positioned downstream to minimally impact lower temperature systems.

REFRIGERANT-SIDE INTEGRATION SYSTEMS

In refrigerant-side integration systems, there are two ITMS modes depending on whether the refrigerant is directly exchanging heat with other systems or not: in the former case, another evaporator directly contacting the battery is added, termed the evaporative integration scheme. If the ITMS has another cooling circuit besides the refrigerant circuit, it is called a secondary circuit integration scheme.

Among the various systems analyzed, in theory, the combination of HPAC and BTM provides the highest energy efficiency. However, further research is

required in this direction. For purely electric vehicles without an ICE, in cold conditions, cabin heating poses a significant challenge since the waste heat from the engine is unavailable. The waste heat is primarily collected by the coolant passing through the batteries, fuel cells, or electronic devices and transferred to a heat exchanger connected with cabin thermal management, either on the refrigerant side or the air side. Schmitt et al.[43] demonstrated that, in addition to batteries and electronic devices, waste heat from fuel cells can also be utilized. After comparing six integration designs with various waste heat sources, they found that using waste heat from fuel cells alone provided the highest cabin temperature.

LIQUID-SIDE INTEGRATION SYSTEM

The most significant example of Liquid-side integration systems was presented by the National Renewable Energy Laboratory ([44] [45]). They developed a combined fluid loop (CFL) technology with the goal of improving electric drive vehicles range and reduce thermal system weight and volume by capturing the synergistic benefits of unifying the thermal management systems.

The investigated CFL technology integrates cabin, Energy Storage System (ESS), and Power Electronics and Electric Motor (PEEM) thermal management into a unified coolant-based system. This system utilizes separate hot and cold fluid streams directed to thermal components as needed. A single heat exchanger at the vehicle's front end either absorbs or rejects heat depending on the CFL system's mode of operation. The system's piping design facilitates coolant direction based on operational requirements, such as actively heating or cooling the ESS and using high-temperature coolant to cool the PEEM. Additionally, waste heat from the PEEM can be recovered to aid in cabin heating. The CFL system also allows directing hot or cold coolant to the passenger cabin, functioning as both an air-conditioner and a heat pump without necessitating a reversal of the refrigerant cycle. This approach avoids issues associated with refrigerant cycle reversal, such as refrigerant charge and oil migration problems, and the need for heat exchangers to alternate between condensing and evaporating roles.

The CFL system offers several benefits, including extending the range of cold-weather electric vehicles by reducing electrical resistance heating of the cabin through PEEM waste heat recovery and heat pump operation. By minimizing

2.4. INTEGRATED THERMAL MANAGEMENT SYSTEMS

the number and size of heat exchangers at the vehicle's front end, aerodynamic drag can be decreased. Another advantage of combining fluid loops is the ability to precondition the ESS, passenger compartment, and thermal management fluid loops when the vehicle is plugged into the grid.

Testing confirmed that PEEM waste heat recovery increased the vehicle's range by approximately 2% during both mild and extreme cold weather conditions. Overall, when considering the U.S. national population and annual vehicle usage, the CFL system demonstrated a 9% increase in EV range, representing a 22.5% improvement over the experimental baseline.

In this thesis, a thermal management system was devised utilizing a liquid-side integration solution structured around a modular approach. The objective was to address the challenge of establishing a scalable thermal management system capable of accommodating various vehicle thermal requirements by employing different combinations of existing components, thus ensuring flexibility and optimal performance.



In-cabin CO₂ measurement

A possible solution to reduce the energy consumption is to recirculate the cabin air. In fact, when the air that enters the HVAC unit is taken from inside the cabin, the air temperature differential is lowered in comparison to when it is drawn from outside the vehicle. Li et al. [46] tested a 2012 Prius PHEV (plug-in hybrid electric vehicle) with the Supplemental Federal Test Procedure SC03 driving cycle [47] and, at the same time, measured the power absorbed by the HVAC system. Their results revealed that the air conditioner consumed 28% of the total power when the cabin air was recirculated, which was 6.1% less than in the fresh air mode. Another advantage of the air recirculation is that it isolates the driver and the passengers from the outside air and so reduces their exposure to the particulate matter. The decrease in the in-cabin particle concentration is obtained thanks to the fact that the air passes through the filter multiple times. In the test performed by Li et al. [46], it was found that the particle concentration was reduced by 85% when the air was recirculated.

However, during the air recirculation the CO₂ concentration levels inside the cabin compartment tend to rise. This happens because the driver and the passengers are sources of CO₂, and when the recirculation mode is on, the air exchanged with the outside ambient conditions is not enough to balance this generation. While the fresh air that comes from the external ambient conditions has a CO₂ concentration of about 400 ppm, the air exhaled by a person generally contains from 38,000 ppm to 56,000 ppm [48] of CO₂. Gladyszewska-Fiedoruk [49], fitting the CO₂ mass balance model with the CO₂ measurements performed inside a passenger car cabin, found that a driver and a passenger exhale 66 g/h

and 35 g/h of CO₂, respectively. Thus, the first exhales as much CO₂ as a man during physical exercise, while the second that of a person during light sedentary work. Some researchers performed CO₂ measurements in vehicle cabins and found the typical values reached in different kinds of vehicle cabins. According to Chiu et al. [50], the cabins of tour buses achieve maximum CO₂ concentrations of more than 3000 ppm and maximum daily average concentrations of 2510.6 ppm for the driver zone and 2646.9 ppm for the passenger zone. Regarding passenger vehicles, Lee and Zhu [51] measured in-cabin CO₂ concentrations that ranged from 620 ppm to 930 ppm in the fresh air mode, while they reached levels of 2500–4000 ppm in the recirculation mode. Zhu et al. [52] showed how quickly the CO₂ concentration levels can grow in a confined space such as a vehicle cabin. In particular, they observed that the CO₂ concentration reached levels of 4500 ppm in less than 10 min when the cabin air was recirculated.

If no fresh air is induced into the cabin, the CO₂ concentration can possibly reach levels that can have effects on the health of the driver and the passengers. Some of the effects, due to a prolonged exposition to high CO₂ concentration levels, can be headache, drowsiness, and decrements in decision-making performance. Generally, the CO₂ concentration levels encountered in vehicle cabins are not high enough to be considered harmful to humans. However, according to the study of Satish et al. [53], the exposure of human subjects to 1000 ppm and 2500 ppm for 2.5 h causes relatively moderate and large decrements in decision-making performance. Therefore, in the case of a cabin vehicle of any type, maintaining the indoor CO₂ concentration levels under certain limits is important to prevent accidents due to the lack of attention of the driver. According to ANSI/ASHRAE Standard 62.1 [54], the CO₂ concentration in indoor environments should not exceed 700 ppm above outdoor air levels. Considering that the outdoor CO₂ concentration is ~400 ppm, the limit for indoor environments should be 1100 ppm. NIOSH [55] recommended an exposure limit equal to 5000 ppm of CO₂ for a 10 h workday during a 40 h workweek and a short-term exposure limit of 30,000 ppm.

In the present study, to reduce the HVAC energy consumption, while maintaining the CO₂ levels within safety conditions, we implemented an automatic on/off control strategy of the air recirculation in the cabin of an electric crane. Then, we monitored experimentally the energy saved thanks to this control strategy, in comparison with the operation in a fresh air mode, during tests performed with different ambient conditions in a climatic wind tunnel [56]. The

cabin of an electric crane was chosen for our tests due to its small dimensions, suitable for fitting in a small, available climatic wind tunnel, which also made it possible to keep the costs of the experiment low. Moreover, such a solution represents one of the vehicles for which Webasto designs their HVAC systems. In a recent article, Pan et al. [57] made an annual energy consumption model that calculated the outside ventilation rate in an electric vehicle, based on a CO₂ concentration limit of 1100 ppm and the windshield anti-fog requirements. Consequently, they evaluated the energy saving effect of this strategy in 30 cities across China. Their results showed that utilizing the recirculated air, while maintaining the CO₂ levels within the requirements, can extend the driving range by 11-30% through a year.

Pei et al. [58] demonstrated, both through CFD (Computational Fluid Dynamics) simulations and experiments, that the CO₂ concentration is not evenly distributed across a mechanically ventilated room. Furthermore, they proved that its diffusion changes depending on the ventilation settings. Considering that the required CO₂ concentration levels should be maintained in the air that the occupant is inhaling, in this study we defined a parameter ([59]) to assess the optimal location for the CO₂ sensor inside the cabin.

Finally, we used the Monte Carlo method ([60]) to compute the uncertainty in the leakage flow measurement depending on the number of CO₂ sensors installed in the cabin compartment [61]. The leakage flow represents the exchanged air flow between the cabin compartment and the external ambient conditions. It can be calculated from the CO₂ measurements, inside and outside the cabin, through the CO₂ mass balance equation (Jung, 2013 [62]; Jung et al. 2017 [63]). The purpose of this last work was to give an indication of the maximum number of sensors that, in our opinion, it is convenient to install in the cabin.

3.1 EXPERIMENTAL SET-UP

For the present study, the CO₂ concentration measurements were performed in a ~2 m³ cabin of an electric crane, which was placed inside a climatic wind tunnel. Different ambient conditions could be established in this environment by choosing a combination of the set points for ambient temperature, relative humidity, solar radiation, and wind speed. The ranges considered for these parameters were 10 °C to 30 °C for the ambient temperature, 50% to 60% for

3.1. EXPERIMENTAL SET-UP

the relative humidity, and 590 W/m^2 to 685 W/m^2 for the solar radiation, and the wind speed was fixed at 15 km/h . The cabin HVAC system was made of an electric heater, a refrigeration cycle, a fan, and two flaps. One flap was used to decide whether to induct fresh air or recirculated air in the cabin, while by changing the position of the other, we could vary how the air was distributed to the different vents in the cabin. The electric heater installed inside the HVAC system was a positive temperature coefficient (PTC) heater. Then, when it heats up, the resistivity of the material increases, causing a reduction in the current absorbed and therefore of the heating power produced. The PTC heater was made of three heating elements; so, it could be regulated on three levels of heating power when it was on: 0.8 kW , 1.6 kW , and 2.4 kW . The heating power was controlled using a PI controller on the cabin temperature error: the difference between the set-point temperature and the actual cabin temperature. Another PI controller on the cabin temperature error was used to control the rotational speed of the compressor for the refrigeration cycle. While the PTC heater could be turned off when the actual temperature was inside a set-point temperature interval, the compressor could not: a minimum speed of 800 rpm was set for the purpose of cabin dehumidification. Moreover, a limit on the maximum compressor speed was set to prevent icing on the evaporator (the temperature of the evaporator had to be greater than $4 \text{ }^\circ\text{C}$). The cabin manufacturer placed the temperature sensor that delivers the data of the cabin temperature to the HVAC control unit in the front right space of the cabin, at a height of 0.45 m with respect to the floor level. The resolution of the sensor embedded in the cabin was $0.5 \text{ }^\circ\text{C}$. We then added a type-j thermocouple, with the sensor in the same position as the first one. The temperature measurements reported in the present paper are referred to the type-j thermocouple. This sensor could measure temperatures in the range of $0\text{--}760 \text{ }^\circ\text{C}$ with an accuracy of $2.2 \text{ }^\circ\text{C}$ or 0.75% of the reading, whichever was bigger.

During the experiment, in place of the driver, a manikin was seated in the cabin. To simulate the breathing of the person, in particular the carbon dioxide generated in the cabin during his exhalation, a system to inject CO_2 in the cabin was built. We used a pressurized tank as the source of CO_2 , and the gas flow from the tank to the cabin was controlled thanks to these components put in series: a pressure regulator, a needle valve, and a thermal mass flow sensor. The CO_2 was injected into the cabin near the mouth of the manikin, and the flow was fixed at the value of 66 g/h . Gladyszewska-Fiedoruk [49] stated

through experimental CO₂ measurements in the cabin of a passenger car, that a passenger is responsible for a CO₂ generation equal to a person who is doing light sedentary work (35 g/h), while a driver exhales as much CO₂ as during physical exercise (66 g/h). In this study, the thermal mass flow sensor used to measure the CO₂ mass flow injected into the cabin was the Sensirion SFM 4100 [64]. This is a low-cost digital mass flow meter for gasses that is able to measure up to 20 slm (reference condition for standard liter per minute: 20 °C, 1013 mbar) with an accuracy of the 3% of the reading or 0.15% of the full scale, whichever is bigger. The sensor element, the signal processing, and the digital calibration are combined on a single microchip embedded in the gas flow meter. In addition to the thermal mass flow sensor, this chip contains an amplifier, an A/D converter, an EEPROM memory, and a digital signal processing circuitry and interface. Through its digital I2C interface, the gas flow meter was embedded into a microprocessor environment (Arduino 2560 Mega).

For the measurement of the CO₂ concentration, the non-dispersive infrared (NDIR) sensors Telaire T6713-5k and Telaire T6743-40K-E [65], produced by Amphenol Corporation in Pennsylvania, U.S., were used. NDIR sensors work by doing a specific spectral analysis within the infra-red wavelengths; carbon dioxide absorbs light at a 4.2 μm wavelength. The components of these sensors are an incandescent lamp, used as the infra-red source, a light-detecting thermopile with a narrow bandpass filter, and a gas chamber, located between the source and the detector of the IR radiation. In essence, the more CO₂ there is in the chamber, the less light is received by the thermopile. By filtering the light over the area around the wavelength equal to 4.2 μm, it is possible to observe a change in the output signal as there is more or less CO₂. The correlation between the CO₂ concentration and the difference between the intensity of the radiation emitted by the IR source and of the light detected by the thermopile is given by the Beers Law [66]. The Telaire T6713-5k is a sensor which is ideal for application in an indoor environment where the CO₂ levels need to be measured and controlled for air quality and energy-saving requests. For this purpose, the sensor is factory-calibrated to measure CO₂ concentration levels up to 5000 ppm. In the measurement range, the accuracy is ± 30 ppm ± 3% of the reading. To acquire the output signal, we used the digital I2C interface so that the CO₂ sensor could be embedded into a microprocessor environment. The Telaire T6743-40K-E is a CO₂ sensor used for automotive HVAC applications. In particular, it has two purposes, one for safety and the other for energy saving. For the first purpose,

3.1. EXPERIMENTAL SET-UP

the sensor is used to measure and control the in-cabin CO₂ levels to prevent driver drowsiness; in this case, the sensor can be configured to measure CO₂ concentrations up to 40,000 ppm with an accuracy of $\pm 200 \text{ ppm} \pm 10\%$ of the reading. The second purpose is achieved through demand-control ventilation, based on a target in-cabin CO₂ concentration level. In this situation, the sensor can be configured to operate in the range 400–5000 ppm. In order to communicate with the control unit of a vehicle HVAC system, the T6743-40K-E model implements a LIN interface. Both the models of CO₂ sensors used in this study have received a factory calibration and use an algorithm called ABCLogic (Automatic Background Calibration) to compensate sensor long-term drift. Outside levels of CO₂ are generally around 400 ppm. When an indoor environment is unoccupied for 4 to 8 h, the CO₂ levels will tend to drop to outside background levels. ABCLogic utilizes the computing power in the sensors on-board microprocessor to remember the lowest CO₂ concentration that takes place every 24 h. The sensor assumes this low point is at outside levels. Once the sensor has collected 14 days worth of low concentration points, it performs a statistical analysis to see if there have been any small changes in the sensor reading over the background level that could be attributable to sensor drift. If the analysis concludes there is drift, a small correction factor is made to the sensor calibration to adjust for this change.

The CO₂ concentration in the cabin volume was measured with 9 sensors placed in 9 different locations, as represented schematically in Figure 3.1. Considering the values of height with respect to the level of the floor where the occupant lays the feet, the sensor locations were the following:

1. At the rear bottom space of the cabin, in the proximity of the recirculation vent, at a height of 0.36 m.
2. In the middle-left space of the cabin, at a height of 0.96 m.
3. Near the roof, in the top right space of the cabin, at a height of 1.41 m.
4. In the front-bottom space of the cabin, on the wall at the right of the center console, at a height of 0.45 m.
5. In the same area as the previous sensor, but at a height of 0.30 m.
6. The last 4 sensors were in the middle of the volume in front of the manikin, all on the same vertical axis, at the heights of 0.45 m, 0.92 m, 1.16 m, and 1.40 m. We thought that in these positions we would have been able to measure the CO₂ concentration level of the air inhaled by a possible driver. In fact, as described by ASHRAE 62.1 [54], the volume included by

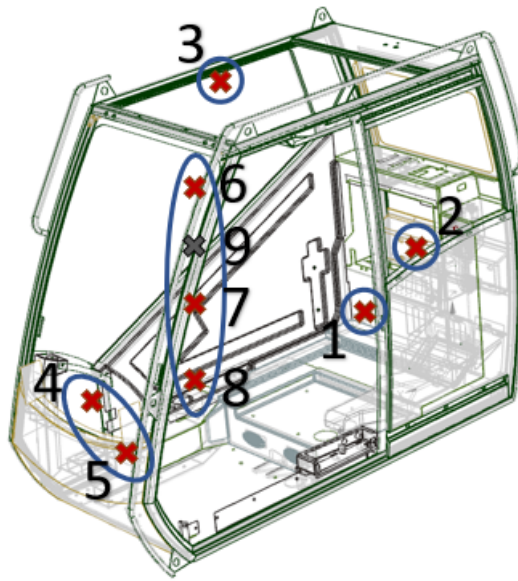


Figure 3.1: Schematic representation of the CO₂ sensors positions inside the crane cabin

the planes at 0.075 m and 1.8 m above the floor, and a surface obtained from a 0.6 m offset of the lateral walls or of fixed air conditioning equipment is defined as the breathing zone. However, the last condition could not be satisfied because the horizontal dimensions of the cabin were too small. Even putting the sensors in the middle of the cabin, the distance between them and the walls on both sides was 0.45 m.

A good position for the sensor could be in the cabin seating. However, this position has not been considered in this paper because it is not easy to implement in a real application. In particular, (i) the CO₂ reading could be perturbed by the occupants emission; (ii) the sensor reading could be perturbed by the seat temperature in the case of a heated seat; and (iii) a custom-made seat would be necessary in order to place the sensor and the cable inside it. Of all the CO₂ sensors installed in the cabin, only the one identified with the number 9 in Figure 3.1 was of the type Telaire T6743-40K-E, while the other 8 sensors were of the model Telaire T6713-5k. The sensor number 9, through its LIN interface, could communicate the value of the CO₂ concentration measured to the HVAC control unit. Thanks to this information, the demanded ventilation of fresh air was controlled by varying the angular position of the recirculation flap. The control strategy that we implemented provided only two positions for the recirculation flap. In the first one, the flap, whose angle of inclination was 0° with respect to the horizontal direction, completely closed the passage for the recirculated air. Thus, the HVAC system would have processed only fresh air. The opposite

3.2. AUTOMATIC AIR RECIRCULATION CONTROL STRATEGY TO IMPROVE ENERGY EFFICIENCY

would have happened with the flap in the second position, with its angle of inclination equal to 90° with respect to the horizontal direction. In this case the HVAC system would have processed only the recirculated air. For the remnant sensors, defined in Figure 3.1 with the numbers 1 to 8, the model Telaire T6713-5k was chosen for its higher accuracy with respect to the other model and for its digital I2C interface. As the aim of these sensors was only to log the data of the measurements, we did not have the need for an LIN interface that would have allowed them to communicate with the HVAC control unit. Moreover, with the digital I2C interface the output signal from the sensors could be easily acquired using a microprocessor. In our case, an STM32F411RE microcontroller was utilized, and we mounted the 8 NDIR CO₂ sensors on two I2C buses; so, there were 4 slave devices on each bus.

3.2 AUTOMATIC AIR RECIRCULATION CONTROL STRATEGY TO IMPROVE ENERGY EFFICIENCY

In the present study, a control strategy for the position of the recirculation flap was implemented. In this way, we could control the amount of air exchanged between the cabins internal volume and the external ambient conditions (here it was the volume of the climatic wind tunnel) in order to contain the in-cabin CO₂ concentration levels within a certain interval of values. In this experiment, the input of the control strategy was the CO₂ measurement inside the cabin, whose reading was from the sensor labelled with the number 9 in Figure 3.1. Concerning this aspect, ASHRAE 62.1 [54] states that the upper limit for the CO₂ concentration level in an indoor environment is 700 ppm over the outdoor CO₂ concentration level, which is generically equal to about 400 ppm. The control strategy that was implemented in the HVAC control unit did not allow a mixture of fresh air and recirculated air. However, the recirculation flap position could only be switched from the recirculation mode to the fresh air mode and vice versa. At the start of the HVAC system, the control unit would have kept the recirculation flap in the position of recirculation mode; then, if the Telaire T6743-40K-E sensor had detected a CO₂ concentration level higher than 1100 ppm, the system would have been switched to the fresh air mode. This configuration would have been maintained until the measured CO₂ concentration level had dropped to under 900 ppm; at this point, the HVAC control unit would have

restored the recirculation flap to the recirculation mode position. In essence, we built an on/off control strategy. The aim of the introduction of a CO₂ sensor to a vehicle cabin is to help reduce the energy consumption of the HVAC unit, as the heating or cooling recirculated air generally requires much less energy because the temperature differential is much less. In this study, we carried out the tests listed in Table 3.1 to determine the energy saved due to the introduction of the controlled outside air induction, as described.

Table 3.1: Settings of the climatic wind tunnel and of the HVAC system for the tests executed in the evaluation of the energy saved thanks to the implementation of a controlled outside air induction.

Test #	T _{amb} ^a [°C]	W _{rad} ^b [W/m ²]	RH ^c [%]	V _{wind} ^d [km/h]	Working mode	Recirc. Flap	S _{CO₂} ^e [g/h]	T _{set-point} ^f [°C]
1a	10	590	70	15	Heating	Fresh air	66	21
2a	10	590	70	15	Heating	Auto ^g	66	21
3a	15	590	60	15	Heating	Fresh air	66	21
4a	15	590	60	15	Heating	Auto ^g	66	21
5a	23	590	55	15	Cooling	Fresh air	66	21
6a	23	590	55	15	Cooling	Auto ^g	66	21
7a	30	685	50	15	Cooling	Fresh air	66	21
8a	30	685	50	15	Cooling	Auto ^g	66	21

^a Ambient temperature. ^b Solar radiation. ^c Relative humidity. ^d Wind speed. ^e CO₂ generation. ^f Cabin set-point temperature. ^g Automatically controlled: the HVAC control unit switches the position of the flap from the recirculation mode to the fresh air mode position depending on the CO₂ concentration level measured.

The measurements of the current absorbed by the HVAC system were made with two Hall-effect probes (Fluke i1010 AC/DC Current Clamps). One was used for the compressor, which worked under a voltage of 400 V, while the other was used for all the remnant elements (fan, electric heater, and cabin electronic components), which operated under a voltage of 27 V. Before the start of each experiment, the cabin door was kept open in order to have the initial conditions of the CO₂ concentration and temperature in the cabin air similar to the external ambient conditions. In the HVAC control unit, two configurations of the flap for the distribution of the air to the different cabin vents were set. In the heating mode, all the air was blown through a diffuser positioned under the seat, as shown by the red arrows in Figure 3.2. While in cooling mode, the air flow was divided among the same diffusers, with the vents near the roof and the vents at the bottom of the lateral window, as shown by the blue arrows in Figure 3.2. In both cases the fan speed was fixed at 50% of its maximum; only in tests 1a and

3.3. ASSESSMENT OF THE OPTIMAL CO₂ SENSOR POSITION

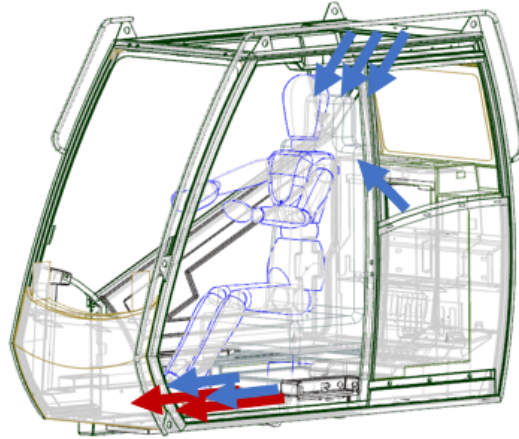


Figure 3.2: Schematic representation of the vent positions. The red arrows indicate the working vents in heating mode. The blue arrows indicate the working vents in cooling mode.

2a was it fixed at 80%.

3.3 ASSESSMENT OF THE OPTIMAL CO₂ SENSOR POSITION

To investigate the optimal location for the CO₂ sensor, the measurements performed by the sensors placed in the breathing zone, defined with the numbers 6, 7, and 8 in Figure 3.1, were used as the reference values. These results were compared, at each time instant, to the CO₂ concentration levels recorded by the five sensors scattered around the cabin, identified in Figure 3.1 with the numbers 1 to 5. The purpose was to evaluate which one of these five positions for the sensor was the best to monitor the in-cabin CO₂ concentration levels. In particular, our aim was to assess which one of these five sensors could measure the closest CO₂ concentration levels to the interval of values logged in the breathing zone, in all the working conditions analysed. Therefore, a parameter was defined to express the positioning performance by quantifying the offset between the measurements made in the spots 1 to 5 and the CO₂ concentration interval measured in the breathing zone. We defined the extremes of this interval as:

$$\begin{aligned} C_{max}(t) &= \max(C_6(t), C_7(t), C_8(t)) \\ C_{min}(t) &= \min(C_6(t), C_7(t), C_8(t)) \end{aligned} \quad (3.1)$$

where t is the time instant, C_i is the CO₂ concentration measured by the sensor i , C_{max} and C_{min} are, respectively, the maximum and minimum CO₂ levels in the breathing zone. Considering the spots 1 to 5 (for $i = 1, \dots, 5$), we calculated, at each time instant, the offset ($\delta(t)$) of the measurement made by sensor i with respect to the breathing zone CO₂ levels as:

$$\begin{aligned} \text{if } C_i(t) < C_{min}(t) &\Rightarrow \delta_i(t) = C_{min}(t) - C_i(t) \\ \text{if } C_i(t) > C_{max}(t) &\Rightarrow \delta_i(t) = C_i(t) - C_{max}(t) \\ \text{if } C_{min}(t) < C_i < C_{max}(t) &\Rightarrow \delta_i(t) = 0 \end{aligned} \quad (3.2)$$

We divided $\delta_i(t)$ by the mean value of the CO₂ concentrations measured at time t by sensors 6, 7, and 8 to calculate the offset in the percentage ($\Delta_i(t)$):

$$\Delta_i(t) = 100 \frac{\delta_i(t)}{\text{mean}(C_6(t), C_7(t), C_8(t))} \quad (3.3)$$

We calculated the mean value ($\bar{\Delta}_i$) of $\Delta_i(t)$ over the time duration of each test ($\tau = 2400$ s) to assess the sensor positioning performance:

$$\bar{\Delta}_i = \frac{1}{\tau} \int_0^{\tau} \Delta_i(t) dt \quad (3.4)$$

Finally, we assumed that the smaller the value of $\bar{\Delta}_i$, the better the performance of the spot i . The settings of the climatic wind tunnel and of the HVAC system for the tests that we performed are listed in Table 3.2. The working conditions examined were the heating, ventilation, and cooling modes, with the fan speed configured at 50% of its maximum. Moreover, for each of these modes, we made the HVAC system operate in the fresh air mode and with the control strategy for the recirculation flap that was described previously. Before the start of each experiment, the cabin door was kept open in order to have the initial conditions of the CO₂ concentration levels in the cabin air similar to the external ambient conditions.

3.4 DETERMINATION OF THE MEASUREMENT UNCERTAINTY OF THE LEAKAGE FLOW

Some standards, related to vehicle air conditioning, define the minimum fresh air flow that must be introduced in the cabin compartment. For example,

3.4. DETERMINATION OF THE MEASUREMENT UNCERTAINTY OF THE LEAKAGE FLOW

Table 3.2: Settings of the climatic wind tunnel and of the HVAC system for the tests executed in the evaluation of the optimal CO₂ sensor positioning.

Test #	T _{amb} [°C]	W _{rad} [W/m ²]	RH [%]	V _{wind} [km/h]	Working mode	Recirc. Flap	S _{CO₂} [g/h]	T _{set-point} [°C]
1b	15	590	60	15	Heating	Fresh air	66	21
2b	15	590	60	15	Heating	Auto	66	21
3b	20	590	55	15	Ventilation	Fresh air	66	–
4b	20	590	55	15	Ventilation	Auto	66	–
5b	30	685	50	15	Cooling	Fresh air	66	21
6b	30	685	50	15	Cooling	Auto	66	21

the standard VDV 236 [67], which refers to buses, says that the HVAC system has to be designed in such a way that at least 15 m³/h per person of fresh air must be provided. With the Monte Carlo method (MCM), we can evaluate the accuracy with which the leakage flow can be estimated from the CO₂ measurement into the cabin compartment. The measurement uncertainty of the leakage flow was used to consider the maximum number of CO₂ sensors that is convenient to install inside the cabin compartment.

3.4.1 APPLICATION OF THE MCM

The MCM, which is defined in Supplement 1 to the Guide to the expression of Uncertainty in Measurements (GUM) [60], was used to determine the estimate and the uncertainty of the measurement of the leakage flow, which could be obtained indirectly from the measurements of the CO₂ concentration levels and of the source of CO₂ in the cabin. The leakage flow is the product between the air exchange rate (AER) and the cabin volume (V_{cab}); in essence, it is the fresh air flow that enters the cabin, which is also equal to the air flow exhausted by the cabin. The model that correlates the leakage flow (Q) to the mean CO₂ concentration (C_{cab}) in the cabin volume is this mass balance equation:

$$V_{cab} \frac{dC_{cab}}{dt} = C_{amb}Q - C_{cab}Q + S \quad (3.5)$$

where C_{amb} is the CO₂ concentration level in the external ambient conditions, S is the source of CO₂, and t is the time instant. With the kind of sensors described in Section 3.1, the measurable quantities are C_{cab} , C_{amb} , and S . Thus, in this equation there are 2 unknowns; these are the leakage flow Q and the

cabin volume V_{cab} . According to Jung [62], when a vehicle is motionless, and the wind speed is therefore zero, and the ventilation fan is off, the leakage flow is negligible and the mass balance Equation 3.5 for the CO₂ becomes, after integrating in time:

$$C_{cab} = \frac{S}{V_{cab}}t + C_{cab,0} \quad (3.6)$$

where $C_{cab,0}$ is the initial value of the CO₂ concentration in the cabin. In this particular condition, we obtain a linear equation with only one unknown, which is the cabin volume. Therefore, from Equation 3.6, considering two time instants, t_1 and t_2 , it is possible to find V_{cab} :

$$V_{cab} = \frac{10^6 Q_{CO_2} (t_2 - t_1)}{C_{cab,2} - C_{cab,1}} \quad (3.7)$$

where $C_{cab,1}$ and $C_{cab,2}$ are the mean CO₂ concentration levels in the cabin volume, respectively, at time t_1 and t_2 . S has been substituted with $10^6 Q_{CO_2}$, where Q_{CO_2} is the CO₂ mass flow injected into the cabin and measured with the mass flow meter. A test was performed where the CO₂ concentration levels were measured with the cabin in this condition. With the results obtained from the measurements at time t_1 and t_2 , we applied the MCM to find the mean and the standard deviation estimations of the cabin volume. We defined M to be equal to 3×10^6 , the number of Monte Carlo trials. Thus, we generated a sequence of M values for each input quantity (Q_{CO_2} , $C_{cab,1}$ and $C_{cab,2}$) by performing M random sampling from their probability distributions. Consecutively, we obtained a sequence of M values for V_{cab} from the calculation of Equation 3.7 for the M trials. We did not corrupt the MCM with the quantities t_1 and t_2 because the error on the timestamp is negligible with respect to the other measurements. The variables $C_{cab,1}$ and $C_{cab,2}$ are obtained from the mean value of the measurements made by the sensors ($C_{i,1}$ and $C_{i,2}$, where i is the sensor counter) placed inside the cabin. The reason is that Equation 3.7 is a lumped-parameter model; so, only one value of the CO₂ concentration level is considered for the entire cabin. For each input quantity, we considered a rectangular distribution, which means the error is uniformly distributed inside the interval of accuracy of each sensor, as given by the datasheet. The output signals of both the CO₂ sensors and the mass flow meter were already processed by their on-board microchips; the microprocessors (Arduino 2560 Mega and STM32F411RE) received a message of zeros and ones from the slave devices.

3.4. DETERMINATION OF THE MEASUREMENT UNCERTAINTY OF THE LEAKAGE FLOW

Therefore, no other errors were added to the ones specified by the datasheets of the sensors. The choice of considering the error as uniformly distributed is motivated by the fact that the manufacturer of the sensors did not provide a PDF (Probability Density Function) associated with the accuracy, but only an interval. As stated in the GUM [68], if the only available information regarding a quantity X is a lower limit a and an upper limit b with $a < b$, then, according to the principle of maximum entropy, a rectangular distribution $R(a, b)$ over the interval $[a, b]$ would be assigned to X . Let us define x_j as a generic input quantity with a_j and b_j as its lower and upper limits, respectively. We can write the generic element $\hat{x}_j(m)$ of the corrupted sequence \hat{x}_j as:

$$\hat{x}_j(m) = a_j + (b_j - a_j) r_j(m) \quad (3.8)$$

where m is the element counter and $r_j(m)$ is a random draw from the standard rectangular distribution whose lower and upper limits are 0 and 1, respectively. As $C_{cab,1}$ ($C_{cab,2}$) was calculated as the mean value of the measurements made in N_s spots inside the cabin, the element of the corrupted sequence $\hat{C}_{cab,1}$ can be written as:

$$\hat{C}_{cab,1}(m) = \frac{1}{N_s} \sum_{i=1}^{N_s} a_{C_{i,1}} + (b_{C_{i,1}} - a_{C_{i,1}}) r_{C_{i,1}}(m) \quad (3.9)$$

where $a_{C_{i,1}}$ and $b_{C_{i,1}}$ are the lower and upper limits for $C_{i,1}$ (CO₂ measurement in the spot number i). The same formula can also be written for $\hat{C}_{cab,2}(m)$. Substituting the input quantities in Equation 3.7 with the respective M corrupted values, we obtained a sequence of M corrupted elements $\hat{V}_{cab}(m)$. Finally, from these M samples of the cabin volume obtained through the MCM, we could calculate the estimation of the mean value and of the standard deviation for the cabin volume: $\mu_{V_{cab}}$ and $\sigma_{V_{cab}}$.

At this point, in Equation 3.5 only Q remains unknown. Integrating in time Equation 3.5 and rewriting it considering 2 time instants, t_1 and t_2 , we have:

$$C_{cab,2} - \left(C_{cab,1} - C_{amb} - \frac{10^6 Q_{CO_2}}{Q} \right) \exp \left[\frac{Q}{V_{cab}} (t_2 - t_1) \right] - C_{amb} - \frac{10^6 Q_{CO_2}}{Q} = 0 \quad (3.10)$$

The same procedure used for the cabin volume was now repeated to find the estimate and the coverage interval for the leakage flow Q . This time, we performed a test with the ventilation fan speed fixed at 50% of its maximum, where

the CO₂ concentration levels were measured in the various spots inside the cabin and in the external ambient conditions; moreover, the CO₂ mass flow injected into the cabin was measured. We used rectangular distributions for the input quantities $C_{i,1}$, $C_{i,2}$, C_{amb} , and Q_{CO_2} . As shown in Section 3.5.3, a Gaussian distribution was obtained for V_{cab} ; so, the element of the corrupted sequence $\hat{V}_{cab}(m)$ was calculated at each trial of the MCM as:

$$\hat{V}_{cab}(m) = \mu_{V_{cab}} + \sigma_{V_{cab}} z_{V_{cab}}(m) \quad (3.11)$$

where $z_{V_{cab}}(m)$ is a random draw from the standard Gaussian distribution that has the best estimate equal to 0 and the variance equal to 1. Finally, substituting in Equation 3.10 the input quantities with their corrupted sequences $\hat{C}_{cab,1}$, $\hat{C}_{cab,2}$, \hat{C}_{amb} , \hat{Q}_{CO_2} , and \hat{V}_{cab} , a sequence \hat{Q} of M elements was obtained by solving Equation 3.10 numerically. From these M samples of the leakage flow, we could calculate the mean value (μ_Q) and the 95% coverage interval for \hat{Q} .

The code used to apply the MCM to Equations 3.7 and 3.10, was written in the Matlab environment. Moreover, to calculate the mean value and standard deviation of a variable, the Matlab tools mean and std were used, respectively. Another Matlab tool, fzero, was utilized to find numerically the value of \hat{Q} that solves Equation 3.10 at each Monte Carlo trial. Finally, the probability distribution of each variable was obtained thanks to the Matlab tool histogram.

3.4.2 PARAMETERS OF THE TEST

For this examination, two types of tests were analysed. The first was to find the PDF for the cabin volume, while the second was to compute the PDF for the leakage flow. The settings for the cabin and the climatic wind tunnel are listed in Table 3.3. Each one of these tests was carried out 8 times. From the first to the eighth case, we changed the number of CO₂ sensors considered inside the cabin from 1 to 8 sensors, respectively. The aim was to observe how the uncertainty in the prediction of the fresh air flow that enters the cabin is affected by the number of CO₂ sensors installed in the cabin. The errors relative to the measurements made in each test are listed in Table 3.4. The time intervals between t_1 and t_2 in test #1c and test #2c were, respectively, 700 s and 2447 s.

3.5. RESULTS

Table 3.3: Settings of the climatic wind tunnel and of the HVAC system for the analysis made with the MCM.

Test #	T_{amb} [°C]	W_{rad} [W/m ²]	RH [%]	V_{wind} [km/h]	V_{fan}^a [%]	Recirc. flap
1c	20	0	55	0	0	Recirc.
2c	20	0	55	15	50	Fresh air

^a Fan speed, expressed as % of its maximum value

Table 3.4: Errors relative to the input quantities for test #1c and test #2c.

Test #	$e_{C_{i,1}}^a$ [ppm]	$e_{C_{i,2}}^a$ [ppm]	$e_{C_{amb}}^a$ [ppm]	$e_{C_{QCO_2}}^a$ [m ³ /s]	$\sigma_{V_{cab}}^b$ [ppm]
1c	77	171	–	3×10^{-7}	–
2c	43	51	43	3×10^{-7}	Found from Test #1c

^a $e_j = (b_j - a_j) / 2$. ^b This value was found from Test #1c, and it is shown in Table 3.6; as shown in Section 3.5.3, the cabin volume PDF was Gaussian, so we indicated its standard deviation.

3.5 RESULTS

In this section, a description of the experimental results is provided for the three topics explained previously. In the first part, a comparison is made between the results of the energy consumed by the HVAC system when working in the fresh air mode and when operating with the automatic control of the fresh air inducted into the cabin activated. In the second part, we show how the CO₂ concentration varies in the breathing zone and around the rest of the cabin volume. Also evaluated is the optimal position for the CO₂ sensor among the five spots analysed, thanks to the introduction of a parameter. In the third part, the results of the application of the Monte Carlo method to find the estimate and the uncertainty of the two indirect measurements, the cabin volume and the leakage flow, are shown.

3.5.1 ASSESSMENT OF ENERGY SAVING DUE TO THE AUTOMATIC AIR RECIRCULATION CONTROL STRATEGY

HEATING MODE

Test #1a and test #3a were executed in the fresh air mode, while during test #2a and test #4a, the cabin air recirculation was automatically controlled, as described in Section 3.2. The ambient temperature in the climatic wind tunnel was set at 10 °C for test #1a and test #2a, and at 15 °C for test #3a and test #4a.

Figures 3.3a, 3.3b, 3.4a and 3.4b show that in the first two tests the CO₂ concentration levels measured were lower compared to the other tests, due to the higher fan speed. In particular, it was equal to 80% of the maximum value in the first case and 50% in the second. As the maximum CO₂ concentration level is limited at 1100 ppm when the air recirculation control strategy is activated, during test #4a the HVAC control unit triggered the fresh air mode more frequently than during test #2a. Looking at the temperature plots in Figures 3.3 and 3.4, when the system operated in the fresh air mode and the steady-state condition was reached, the cabin temperature kept oscillating with almost the same amplitude around a constant value. Conversely, when the air recirculation control strategy was activated, a small temperature drop was recorded every time the fresh air mode was turned on. In both test #2a and test #4a, the system could work for most of the time in recirculation mode, and consequently, we obtained a considerable reduction in the energy consumption with respect to test #1a and test #3a, respectively. When the ambient temperature was 10 °C, the energy consumed by the HVAC system was 1.092 kWh at the end of test #1a and 0.505 kWh at the end of test #2a. Therefore, the air recirculation control strategy allowed an energy saving of the 53.8%. When the ambient temperature was 15 °C, the energy consumed by the HVAC system was 0.514 kWh at the end of test #3a and 0.141 kWh at the end of test #4a. Therefore, the air recirculation control strategy allowed an energy saving of the 72.6%. The reason behind this high value of energy consumption reduction can be found by looking at the plot at the bottom of Figure 3.4b. The figure shows that, when the recirculation mode is on, the cabin temperature curve is not decreasing and at the same time the PTC heater is not delivering any heating power. In these instants, the only source of heat for the cabin is the solar radiation. Therefore, we can understand that the heat dissipated by the cabin, due to the 6 °C of temperature difference between

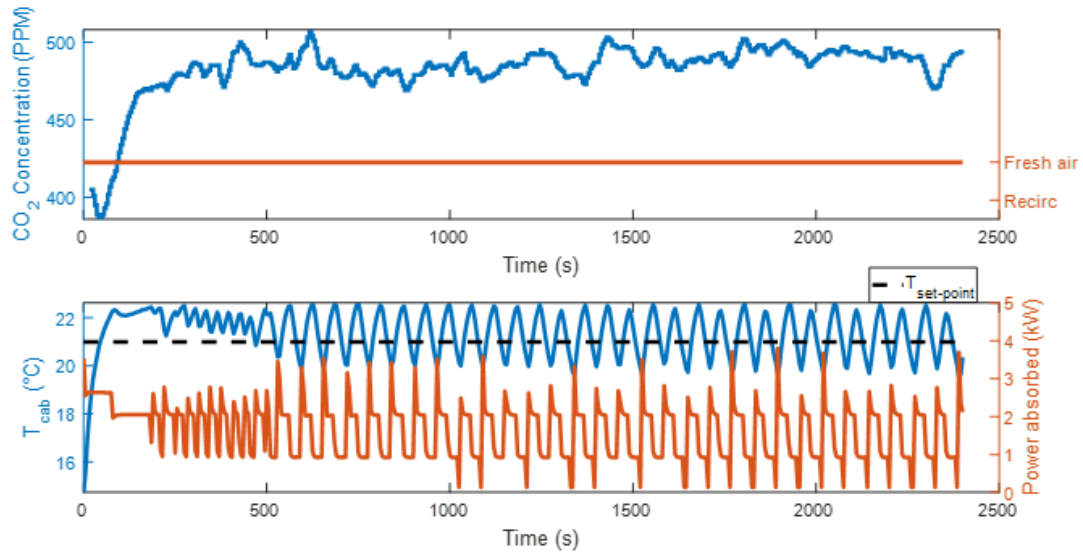
3.5. RESULTS

the inside and the outside environments, is balanced by the solar radiation. As shown in Figure 3.4b, the control system kept the PTC heater off for almost all the duration of test #4a, and it turned the heater on only in those short instants when the fresh air mode was activated. Every time the fresh air mode is turned on, the HVAC system starts to introduce air at 15 °C into the cabin, and therefore, a fall of the cabin temperature is observed. When the HVAC control unit notices this change, it sends the command to activate one of the heaters heating elements.

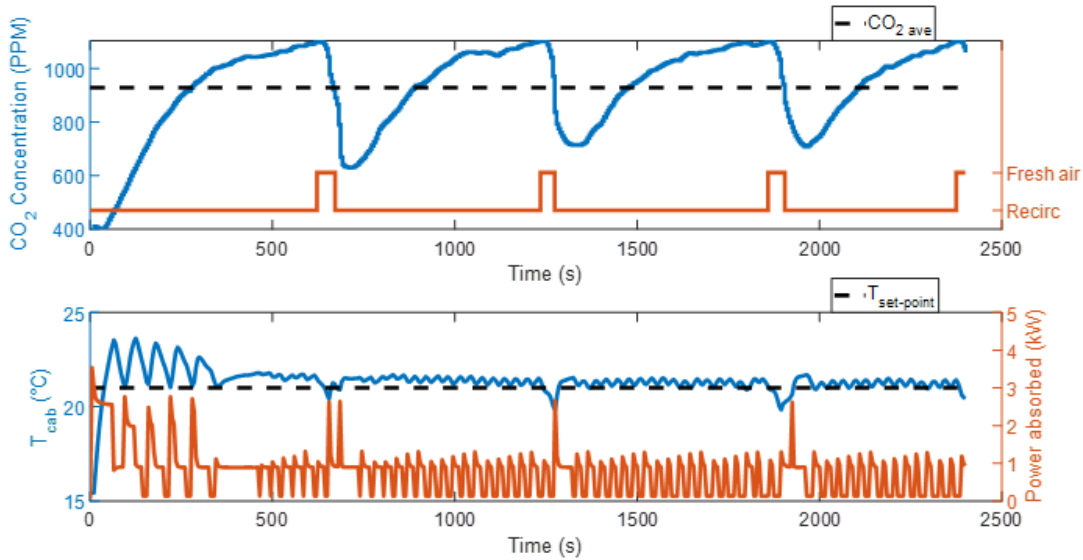
COOLING MODE

With the ventilation distribution set in cooling mode, we measured higher CO₂ concentration levels with respect to the heating mode cases, even if the fan speed was the same (50% of the maximum value), as shown in Figures 3.5 and 3.6. The reason was probably an accumulation of CO₂ in the breathing zone, where the CO₂ sensor was placed (sensor 9 in Figure 3.1), due to the different internal movement of air. In cooling mode, the air distribution flap within the HVAC system divides the fan's airflow into more vents than in heating mode. Consequently, the air velocity from each vent is reduced. We suspect that this reduced airflow velocity may lead to less ventilation in the breathing zone, potentially causing an accelerated accumulation of CO₂ in that area. When the air recirculation control strategy was used, this caused a faster increase in the measured CO₂ levels when the air recirculation mode was on and a slower decrease when the fresh air mode was taking place. This phenomenon triggered a more frequent on/off of the recirculation mode, with respect to the heating condition, as shown in Figures 3.5b and 3.6b. When the air recirculation control strategy was on, the HVAC system spent about half the time of the experiment in the fresh air mode. This implied that the energy saving could not be as great as in the heating mode.

In test #5a and test #6a, the ambient temperature (23 °C) was close to the cabin set-point temperature. In both cases, the steady-state conditions were reached with an actual cabin temperature lower than the set-point temperature. At the steady-state condition, the compressor worked constantly at the minimum rotational speed (800 rpm), delivering more power than needed. So, the cabin temperature measurements and the energy consumption obtained in these two experiments were very similar. The HVAC system consumed 0.502 kWh in test



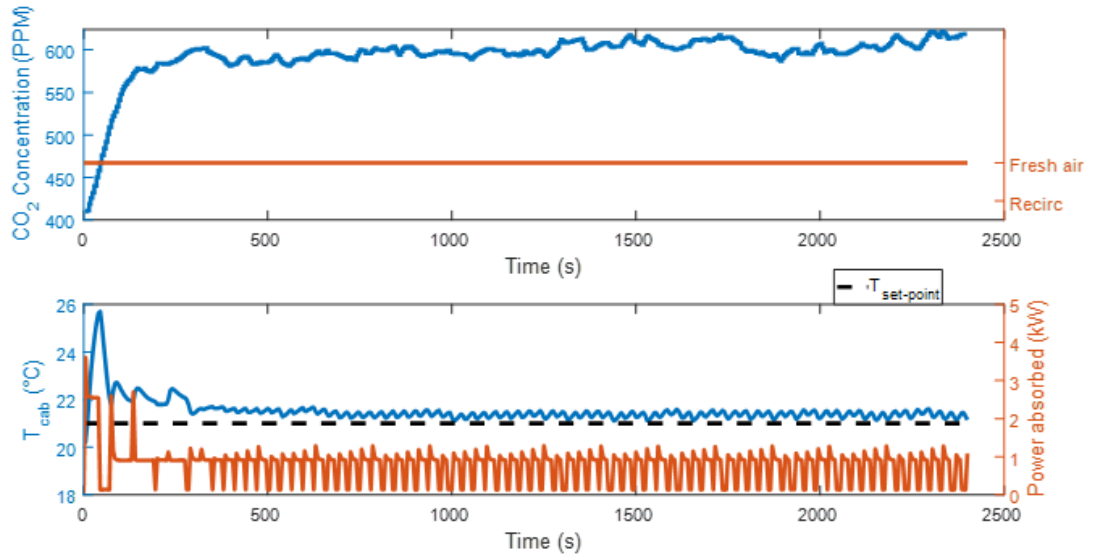
(a) Test #1a



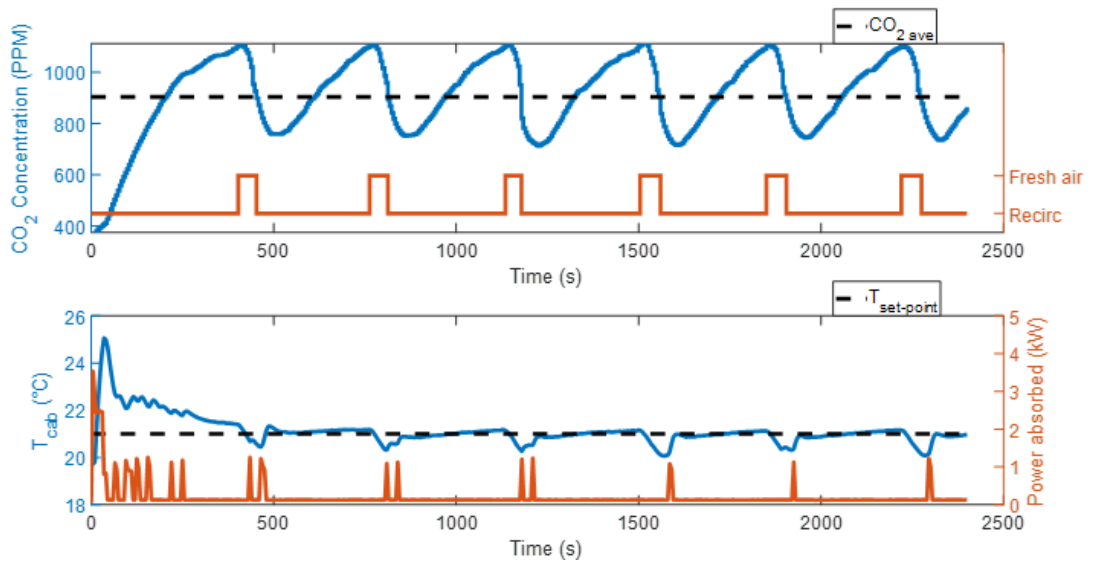
(b) Test #2a

Figure 3.3: CO₂ concentration, power absorbed by the HVAC system and cabin temperature measurements at ambient temperature equal to 10 °C

3.5. RESULTS



(a) Test #3a



(b) Test #4a

Figure 3.4: CO₂ concentration, power absorbed by the HVAC system and cabin temperature measurements at ambient temperature equal to 15 °C

#5a and 0.498 kWh in test #6a. Therefore, only 0.8% of the energy was saved thanks to the introduction of the air recirculation control strategy.

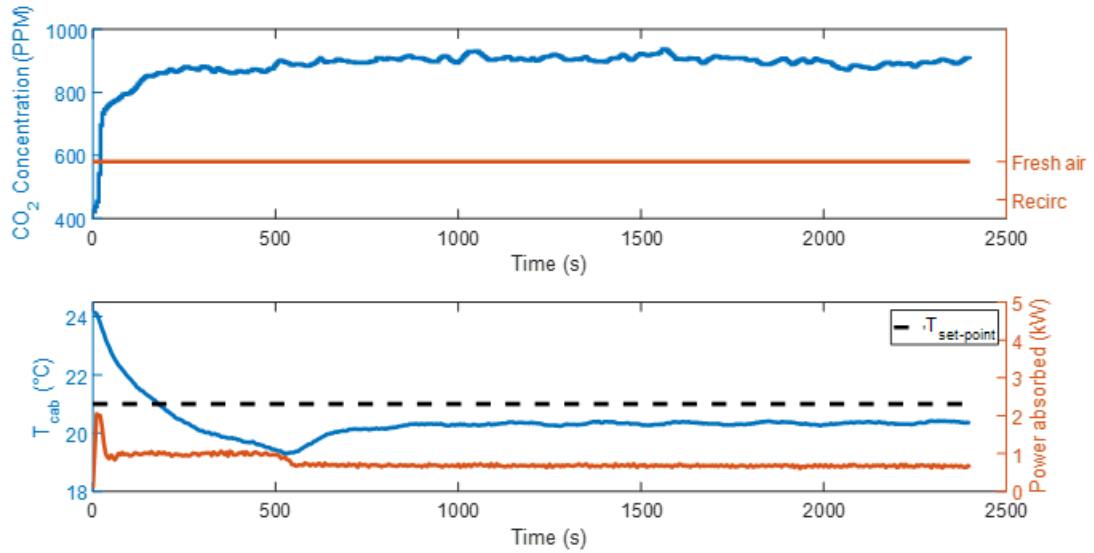
During test #7a, the cabin temperature reached the set-point temperature only at the end of the test (2400 s). In test #8a, the implementation of the air recirculation control strategy allowed the reaching of the cabin set-point temperature after 1300 s. As shown in Figure 3.6b, we can see some oscillations in the cabin temperature curve of test #8a due to the opening and closing of the fresh air flow. At the end of the experiment, the energy consumptions in test #7a and test #8a were, respectively, 0.818 kWh and 0.744 kWh. Therefore, the air recirculation control strategy allowed us to save 9.0% of the energy consumed.

3.5.2 EVALUATION OF THE OPTIMAL CO₂ SENSOR POSITION

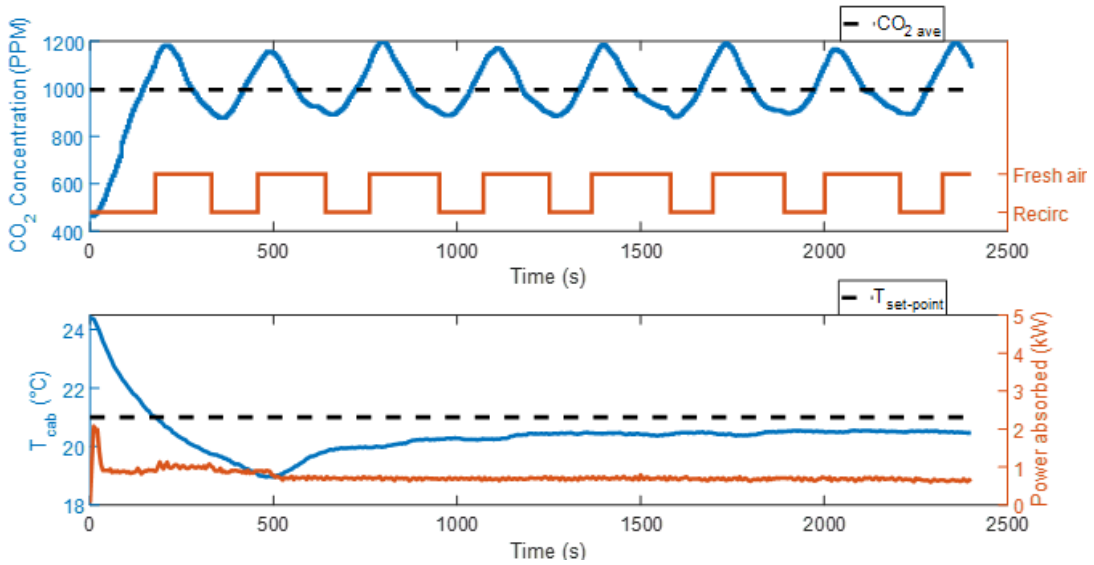
CO₂ STRATIFICATION IN THE BREATHING ZONE

Test #1b and test #2b were executed in heating mode, and all the air was blown by the fan through the vents placed under the seat of the passenger. In contrast, in the ventilation and cooling modes the same air flow was also blown through the vents at the left of the manikin (as shown in Figure 3.2). In Figure 3.7 are represented the values of the CO₂ concentration measured in the breathing zone against the height of the installation of the sensors with respect to the floor level. For the experiments where the HVAC system operated in the fresh air mode, we plotted the value of the CO₂ concentration measured when we reached the steady-state condition for Equation 3.5. For the tests where the air recirculation control strategy was activated, the evolution in time of the CO₂ concentration was always in a dynamic condition. Therefore, we plotted the time-averaged values measured by sensors 6, 7, and 8. The results in Figure 3.7 show different vertical stratifications of the CO₂ levels in the breathing zone. In the heating mode, the CO₂ concentration increased going from the roof level to the floor level, while in the ventilation and cooling modes the maximum values of the CO₂ concentration were measured near the manikins shoulder level. It seems that in the last case, the air was more stationary in the breathing zone, causing an accumulation of CO₂ in that area. Figure 3.7 shows that the CO₂ stratification profile was similar in the ventilation and in the cooling modes

3.5. RESULTS

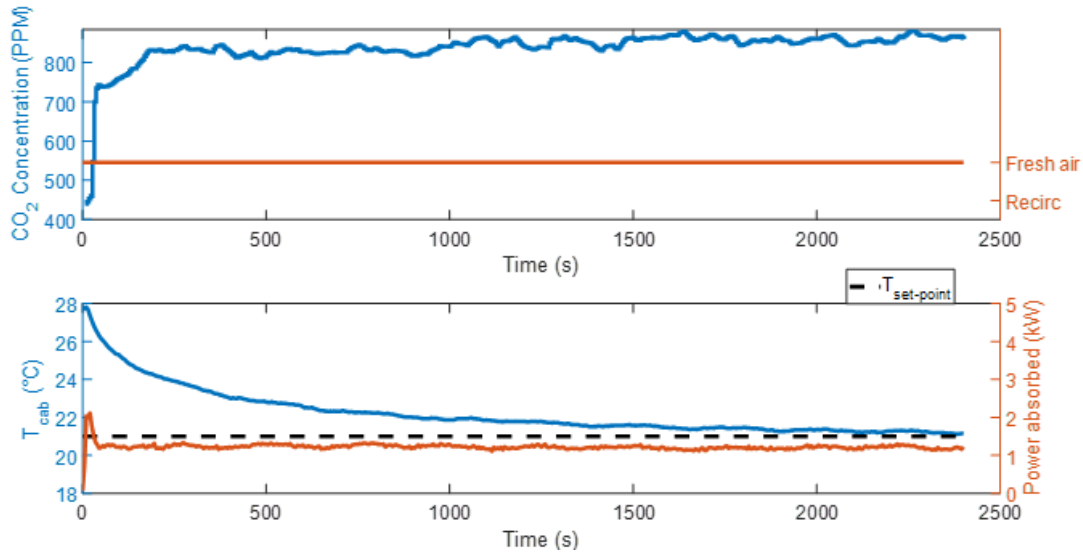


(a) Test #5a

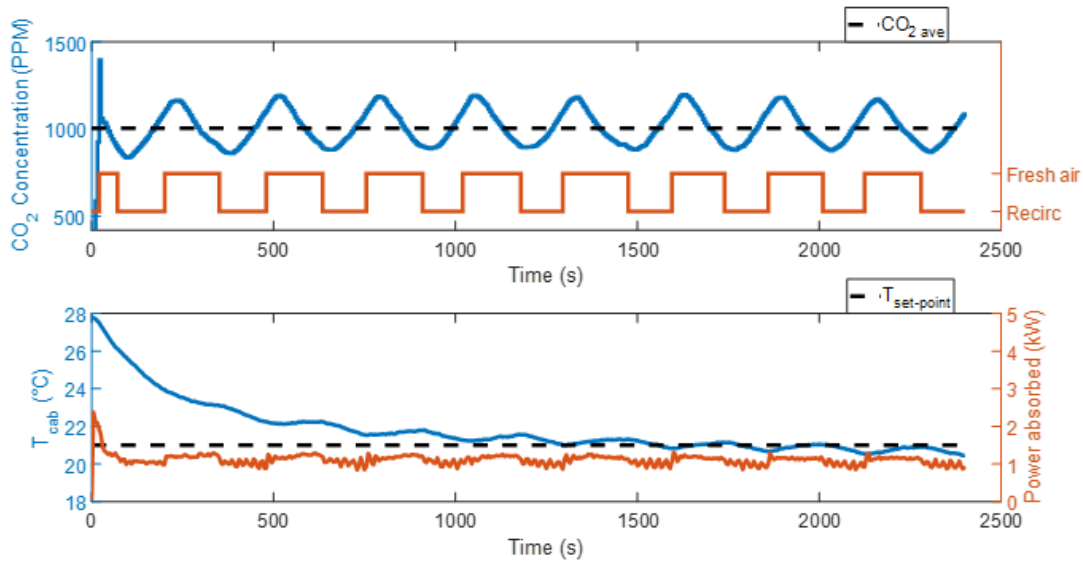


(b) Test #6a

Figure 3.5: CO₂ concentration, power absorbed by the HVAC system and cabin temperature measurements at ambient temperature equal to 23 °C



(a) Test #7a



(b) Test #8a

Figure 3.6: CO₂ concentration, power absorbed by the HVAC system and cabin temperature measurements at ambient temperature equal to 30 °C

3.5. RESULTS

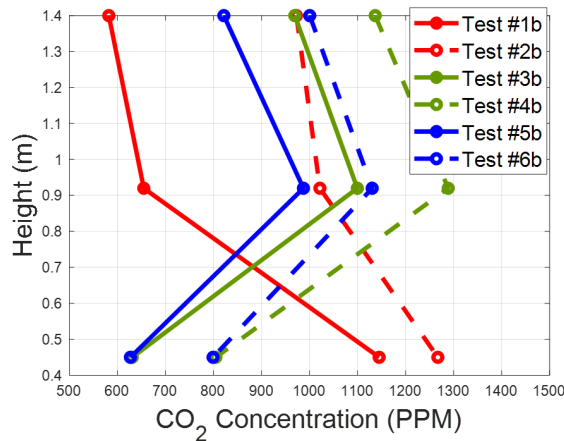


Figure 3.7: Vertical stratification of the CO₂ in the breathing zone.

because the air blown by the fan was distributed to the same vents. So, the internal aerodynamics of the cabin were almost alike; the difference was due to the convection effect. We can say that the diffusion of the CO₂ in the cabin compartment is principally dependent on how we distribute the air flow between the various cabin vents.

CO₂ SENSOR POSITIONING PERFORMANCE

Table 3.5 shows the calculated values of the parameter $\bar{\Delta}_i$ which is an indicator of the difference, due to the sensor position, between the CO₂ measurements performed by sensors 1 to 5 and the CO₂ concentration measured in the breathing zone (sensors 6, 7, and 8). For the evaluation of the optimal sensor positioning, we considered the tests performed for the cases of internal ventilation in the fresh air mode and with the air recirculation automatically controlled, for each operating condition: the heating, ventilation, and cooling modes.

Table 3.5: Values of $\bar{\Delta}_i$ (expressed in [%]) for CO₂ sensors 1 to 5.

Sensor	Heating mode		Ventilation mode		Cooling mode	
	Fresh air	Auto	Fresh air	Auto	Fresh air	Auto
1	2.57	1.20	9.10	5.82	4.32	4.61
2	2.49	7.22	1.36	2.79	0.15	1.54
3	1.31	3.23	1.51	1.72	0.17	2.19
4	0.00	1.56	10.54	6.45	12.22	8.87
5	4.47	8.64	24.24	19.15	22.84	18.97

In all the tests performed, sensor 5 was the one characterized by the greatest

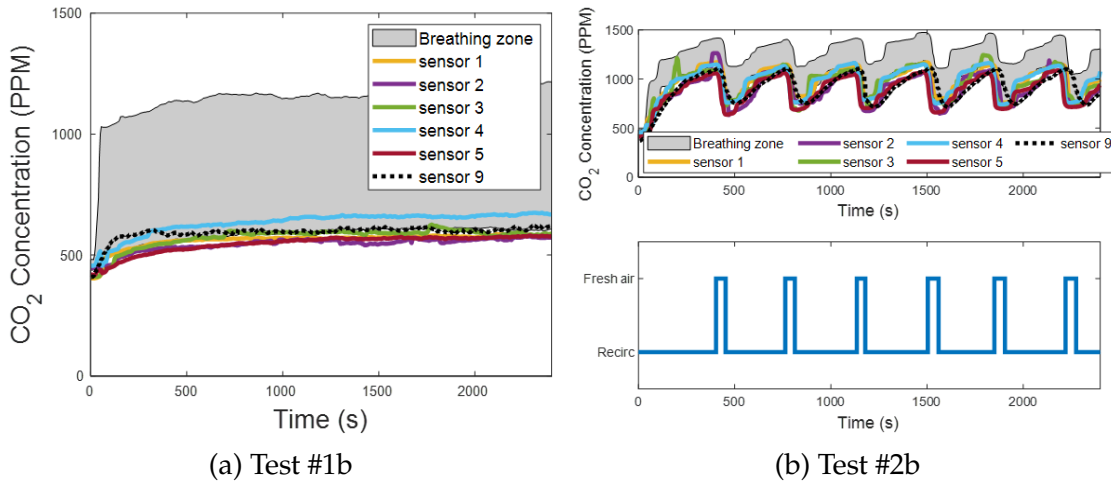


Figure 3.8: CO₂ concentration measurements acquired from the 9 sensors that were installed in the cabin compartment in heating mode

values of $\bar{\Delta}_i$ because it was positioned in the direction of the air flow blown through the diffuser under the drivers seat. In fact, it was always the one that recorded the lowest values of CO₂ concentration because it was almost directly hit by the fresh air flow induced in the cabin. Figure 3.8a, Figure 3.9a, and Figure 3.10a show the evolution in time of the CO₂ concentrations measured by sensors 1 to 9 in the fresh air mode. Figure 3.8b, Figure 3.9b, and Figure 3.10b show the same measurements performed when the automatic control of the recirculation mode was activated. When the fresh air mode was on, sensors 2 and 3, which were the nearest to the head level, were the ones that registered the lowest values of $\bar{\Delta}_i$. Instead, when the recirculation mode was on, the ones that recorded the lowest values of $\bar{\Delta}_i$ were sensors 1 and 4. Figure 3.8b, Figure 3.9b, and Figure 3.10b show that during test #2b, the HVAC system worked in recirculation mode for most of the time, while in test #4b and test #6b, the time spent in fresh air mode was about half the duration of the experiment. The results obtained in Table 3.5 were similar between the ventilation and the cooling operating conditions, while they were quite different between the heating operating condition and the other two, due to the diverse internal aerodynamics of the cabin. In the heating mode, the sensors that recorded the lowest values of $\bar{\Delta}_i$ were sensors 1 and 4, while in the other two operating conditions were sensors 2 and 3. Considering the mean between the values of $\bar{\Delta}_i$ calculated in tests #1b, #2b, #3b, #4b, #5b, and #6b, the minimum result was calculated for sensor 3, and it was 1.69%. Therefore, we concluded that the position of sensor 3 was the best one for this cabin.

3.5. RESULTS

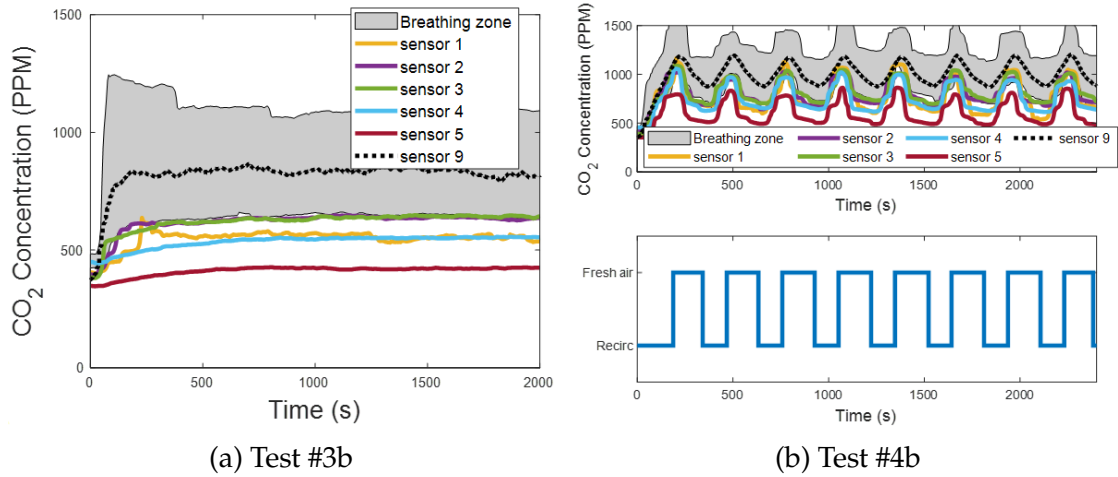


Figure 3.9: CO₂ concentration measurements acquired from the 9 sensors that were installed in the cabin compartment in ventilation mode

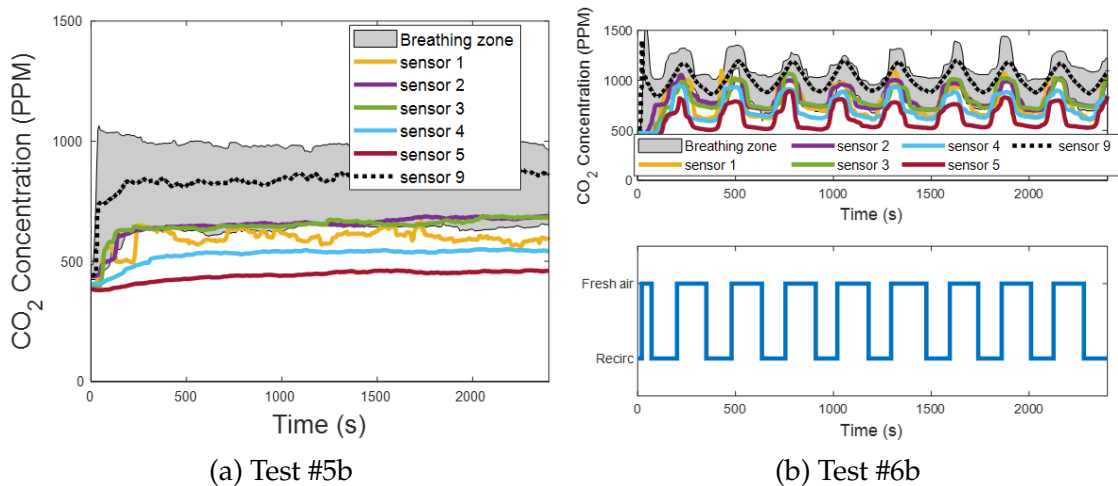


Figure 3.10: CO₂ concentration measurements acquired from the 9 sensors that were installed in the cabin compartment in cooling mode

When contemplating various cabins with different geometries, these findings imply that it is generally wise to position the CO₂ sensor at a height near the driver's head and in a location away from vents. This is because, when fresh air is introduced into the cabin, placing the sensor close to a vent might yield a CO₂ concentration measurement lower than that in the breathing zone.

3.5.3 RESULTS OF THE MONTE CARLO METHOD APPLIED ON INDIRECT MEASUREMENTS

When two CO₂ sensors are used, the probability distribution of the variables $\hat{C}_{cab,1}$ and $\hat{C}_{cab,2}$ becomes triangular, while with three or more CO₂ sensors, it becomes Gaussian. The results from test #1c showed that the probability distribution of \hat{V}_{cab} is Gaussian in all the tests performed, with a decreasing standard deviation as the number of CO₂ sensors considered (N_s) increases. In Figure 3.11, the propagation of distributions for the input variables that appear in Equation 3.7 is plotted. On the left, there are the probability distributions for the input quantities: the in-cabin CO₂ concentration levels at t_1 and t_2 and the source of CO₂. On the right, there is the probability distribution for the indirect measurement of test #1c, which is the cabin volume. The curves related to each value of N_s are plotted, and the results in the x-axis of Figure 3.11 have been normalized in this way:

$$x^* = \frac{x - \mu_x}{\mu_x} \quad (3.12)$$

where x is a generic variable and μ_x is the mean value of x .

Table 3.6: Results from test #1c using MCM.

N_s	$\mu_{C_{cab,1}}$ [ppm]	$\sigma_{C_{cab,1}}$ [ppm]	$\mu_{C_{cab,2}}$ [ppm]	$\sigma_{C_{cab,2}}$ [ppm]	$\mu_{Q_{CO_2}}$ [m ³ /s]	$\sigma_{Q_{CO_2}}$ [m ³ /s]	$\mu_{V_{cab}}$ [m ³]	$\sigma_{V_{cab}}$ [m ³]
1	1560	40	4700	100	1.00x10 ⁻⁵	2.00x10 ⁻⁷	2.23	0.09
2	1560	30	4700	70	1.00x10 ⁻⁵	2.00x10 ⁻⁷	2.23	0.07
3	1560	30	4700	60	1.00x10 ⁻⁵	2.00x10 ⁻⁷	2.23	0.06
4	1560	20	4700	50	1.00x10 ⁻⁵	2.00x10 ⁻⁷	2.23	0.05
5	1560	20	4700	40	1.00x10 ⁻⁵	2.00x10 ⁻⁷	2.23	0.05
6	1560	20	4700	40	1.00x10 ⁻⁵	2.00x10 ⁻⁷	2.23	0.05
7	1560	20	4700	40	1.00x10 ⁻⁵	2.00x10 ⁻⁷	2.23	0.05
8	1560	20	4700	30	1.00x10 ⁻⁵	2.00x10 ⁻⁷	2.23	0.05

3.5. RESULTS

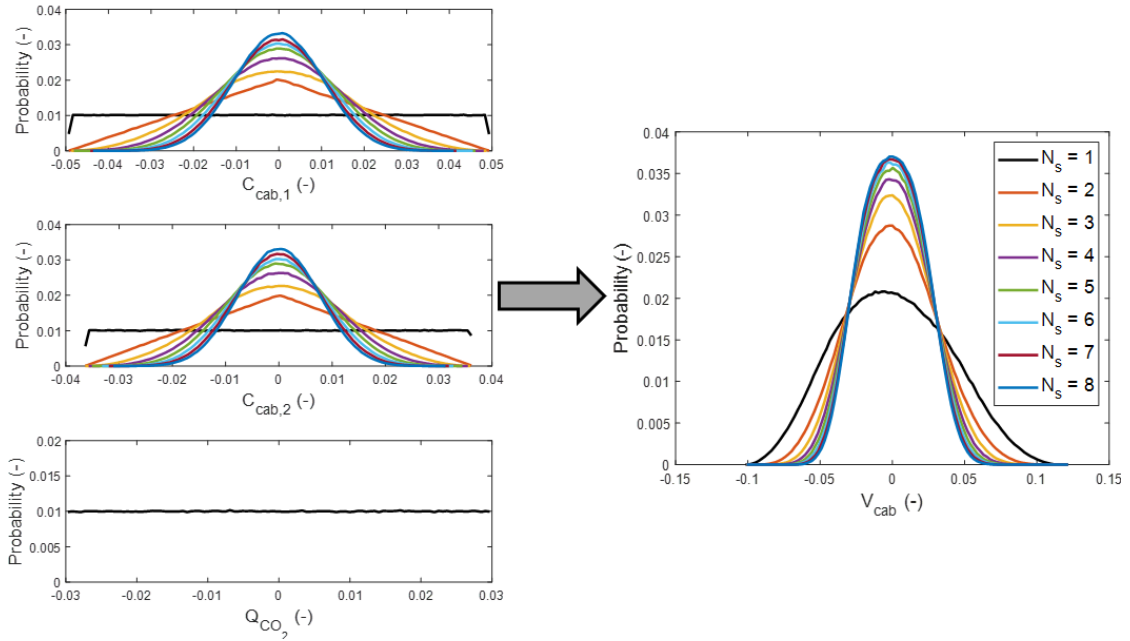


Figure 3.11: Illustration of the propagation of distribution for the input quantities obtained by the application of the MCM in test #1c

Table 3.6 lists the results from test #1c performed by using the MCM. The values contained in the table are the mean value and the standard deviation for the variables $\hat{C}_{cab,1}$, $\hat{C}_{cab,2}$, \hat{Q}_{CO_2} , and \hat{V}_{cab} . They were found for the eight cases studied where the number of CO₂ sensors considered in the cabin was changed from 1 to 8. The standard deviation values have been written with one significant digit, as suggested by the GUM [68]. For N_s greater than 4, it is not possible to observe changes in $\sigma_{V_{cab}}$.

The findings obtained from test #1c for the variable \hat{V}_{cab} were used in test #2c to define the Gaussian distribution from which the element $\hat{V}_{cab}(m)$ was sampled at each Monte Carlo trial. The outcomes found from test #2c revealed that the probability distribution of \hat{Q} is not symmetric around the mean value μ_Q . In Figure 3.12, the propagation of distributions for the variables that appear in Equation 3.10 is plotted. On the left, there are the probability distributions for the input quantities: the in-cabin CO₂ concentration levels at t_1 and t_2 , the CO₂ concentration levels in the external ambient conditions, the source of CO₂, and the cabin volume. On the right, there is the probability distribution for the indirect measurement of test #2c, which is the leakage flow. Moreover, in this figure, the curves related to each value of N_s are plotted, and the results have

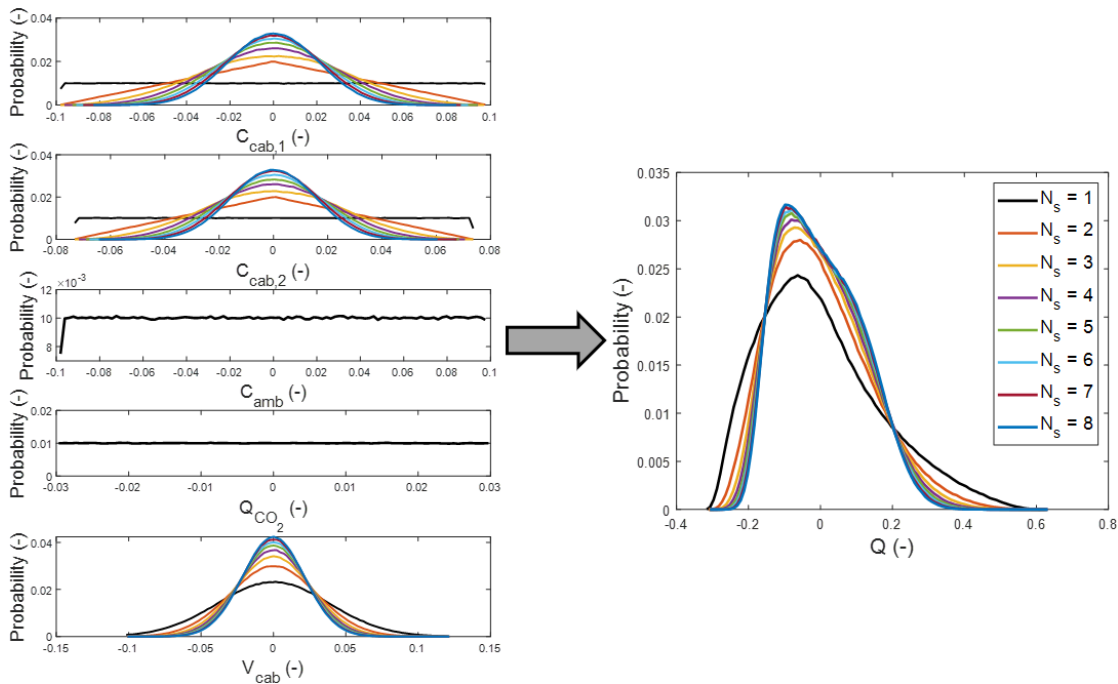


Figure 3.12: Illustration of the propagation of distribution for the input quantities obtained by the application of the MCM in test #2c.

been normalized as defined in Equation 3.12.

The results obtained from test #2c, by using the MCM, are listed in Tables 3.7 and 3.8. Moreover, in this case the standard deviations values have been written with one significant digit. In Table 3.7, the mean value and the standard deviation of the input variables are recorded, for the N_s values equal to 1 to 8: $\hat{C}_{cab,1}$, $\hat{C}_{cab,2}$, \hat{C}_{amb} , \hat{Q}_{CO_2} , and \hat{V}_{cab} .

As \hat{Q} was not symmetrically distributed around the mean value, we used the shortest 95% coverage interval to define its measurement uncertainty. In Table 3.8, we listed the estimate μ_Q and the endpoints of the coverage interval for the leakage flow (the output variable).

Every time we increase the number of CO₂ sensors installed into the cabin, the benefit in terms of the measurement uncertainty improvement of the leakage flow is smaller. Hence, at a certain point, it is not convenient to add other CO₂ sensors, considering that we are increasing the cost of the HVAC system. Increasing the value of N_s , the 95% coverage interval tended to become symmetric around the mean value μ_Q , until N_s was equal to 7. When N_s was equal to 8, a shift to the right of the 95% coverage interval was observed. The reported results in Table 3.8, corresponding to declaring one significant digit in the standard un-

3.5. RESULTS

Table 3.7: Results for input variables from test #2c using MCM.

N_s	$\mu_{C_{cab,1}}$ [ppm]	$\sigma_{C_{cab,1}}$ [ppm]	$\mu_{C_{cab,2}}$ [ppm]	$\sigma_{C_{cab,2}}$ [ppm]	$\mu_{C_{amb}}$ [ppm]	$\sigma_{C_{amb}}$ [ppm]	$\mu_{Q_{CO_2}}$ [m ³ /s]	$\sigma_{Q_{CO_2}}$ [m ³ /s]	$\mu_{V_{cab}}$ [m ³]	$\sigma_{V_{cab}}$ [m ³]
1	440	20	690	30	440	20	1.00x10 ⁻⁵	2.00x10 ⁻⁷	2.23	0.09
2	440	20	690	20	440	20	1.00x10 ⁻⁵	2.00x10 ⁻⁷	2.23	0.07
3	440	10	690	20	440	20	1.00x10 ⁻⁵	2.00x10 ⁻⁷	2.23	0.06
4	440	10	690	10	440	20	1.00x10 ⁻⁵	2.00x10 ⁻⁷	2.23	0.05
5	440	10	690	10	440	20	1.00x10 ⁻⁵	2.00x10 ⁻⁷	2.23	0.05
6	440	10	690	10	440	20	1.00x10 ⁻⁵	2.00x10 ⁻⁷	2.23	0.05
7	438	9	690	10	440	20	1.00x10 ⁻⁵	2.00x10 ⁻⁷	2.23	0.05
8	438	9	690	10	440	20	1.00x10 ⁻⁵	2.00x10 ⁻⁷	2.23	0.05

Table 3.8: Results for the output variable from test #2c using MCM.

		95% Coverage Interval	
N_s	μ_Q [m ³ /h]	Lower Endpoint [m ³ /h]	Upper Endpoint [m ³ /h]
1	140	110	190
2	140	110	180
3	140	110	180
4	140	110	170
5	140	110	170
6	140	110	170
7	140	110	170
8	140	120	170

certainty, show that we cannot appreciate a change in the 95% coverage interval for N_s greater than 4, apart from when N_s was equal to 8. Even in Figure 3.12, we can see that the curves of the probability distributions for N_s greater than 4 are pretty much superimposed. Therefore, we think that it is not convenient to install more than four CO₂ sensors inside the cabin compartment.

This conclusion can be applied to cabins of varying dimensions and geometries. Notably, the measurement uncertainty of the cabin volume is independent of its shape or geometry; rather, it hinges solely on the accuracy of the CO₂ sensors and of the mass flow meter responsible for measuring the injected CO₂ amount. However, the optimal quantity of CO₂ sensors to install in the cabin is contingent on the quality of these sensors. In such cases, one should assess whether it is more cost-effective to deploy a higher number of less expensive

(and less accurate) sensors compared to a reduced number of pricier ones, taking into account the sensors' lifespan as well.

3.6 DISCUSSION

In this study, we implemented a control strategy for the air recirculation that allowed a reduction in the HVAC system energy consumption, while keeping the cabin CO₂ concentration under 1100 ppm. Compared to the passenger vehicles used by other researchers, the CO₂ measurements that we performed in our crane cabin revealed a slower increase in the CO₂ concentration levels. This means that a crane cabin is less hermetic than a generic passenger vehicle cabin. We also paid attention to the propagation of the CO₂ inside the cabin volume, in different operating modes, because generally it is not uniformly distributed. The results showed that the propagation is mainly dependent on how the air flow coming from the HVAC unit is spread to the various cabin vents. As we were interested in maintaining safe conditions regarding the CO₂ concentration levels in the breathing zone, the ventilation setting influenced the demanded fresh air flow. Consequently, it affected the energy saving due to the execution of the air recirculation control strategy. As in a real application, we cannot place the CO₂ sensor in the breathing zone, we studied five potential spots for the sensor. The purpose was to determine in which of these positions we could measure the closest CO₂ concentration levels to the breathing zone, in the operating modes analysed. By defining a parameter that compared the CO₂ measurements in these five locations with the ones in the breathing zone, we found that the spot at the top right space of the cabin was the optimal one. Finally, considering that some standards related to vehicle air conditioning define the minimum fresh air flow that must be introduced in the cabin compartment, we used the MCM to compute the measurement uncertainty of the leakage flow. In particular, we observed how the confidence interval for the leakage flow changed depending on the number of CO₂ sensors installed inside the cabin. The confidence interval depends on the accuracy of each sensor and the number of sensors used. In this regard, we made tests varying the number of sensors considered while keeping unchanged the type of sensors (in other words the accuracy of each sensor), and we found that using more than four sensors did not produce an appreciable further improvement in the confidence interval. To sum up, we can assume four is the optimal number of CO₂ sensors to improve the accuracy of our

3.6. DISCUSSION

measurement.



Design of the ITMS

The Electric Thermal Management (e.TM) system is a technological advancement in the thermal regulation of electric vehicles. It significantly enhances vehicle efficiency by minimizing the efficiency loss due to external temperature effects on the batteries, particularly in harsh conditions.

Research primarily focuses on enhancing the vehicle's range and overall efficiency by unifying individual thermal regulation systems. Traditional approaches had separate thermal management for three key areas: cabin air conditioning, battery temperature regulation, and PEEM/ECUs (Electronic Control Units) cooling. The innovation behind e.TM lies in its holistic approach, combining all these functions into a singular integrated system, offering an optimized solution for the entire vehicle [44] [69] [70] [71].

Key functionalities of the e.TM system include:

- Passenger compartment Heating, Ventilation, and Air Conditioning (HVAC) to manage temperature, humidity, and CO₂ levels.
- Driver-specific HVAC.
- Battery thermal management.
- Thermal control of PEEM and ECUs (covering aspects such as the electric motor, DC/DC Converter, Charger, Autonomous Driving System, etc.) that only requires the function of cooling [31].

This integrated approach ensures that passenger and driver comfort coexists seamlessly with the temperature needs of the battery and vehicular electronic systems. Unlike conventional electric vehicle thermal systems that operate as

4.1. INTEGRATED THERMAL MANAGEMENT CONCEPT

an ensemble of multiple components managing various thermal loads, e.TM provides a cohesive solution. A non-integrated e.TM system is traditionally designed with each subsystem sized for its specific needs, not taking advantage of potential synergistic benefits. An integrated e.TM system, however, can capitalize on overlaps in thermal demands, resulting in reduced overall power needs, component size, and weight. For instance, the primary need for battery cooling is during its fast-charging phase, a time when passengers are typically not in the vehicle. With an integrated e.TM system, the power can be prioritized for battery cooling during charging and redirected to HVAC during driving. Additionally, a centralized control in the integrated system enables better management of potential failures, adjusting or prioritizing thermal demands as required.

Benefits of a fully integrated e.TM system include:

- Enhanced comfort by fine-tuning heating and cooling according to demand.
- Heightened safety through centralized diagnostics.
- Improved efficiency and reduced energy consumption.
- Extended battery life.
- Shorter battery charging times.

4.1 INTEGRATED THERMAL MANAGEMENT CONCEPT

The vehicle integrated thermal management system that is presented in this thesis is based on the secondary loop concept. In particular it consists in a primary loop, that is a vapor compression refrigeration system (it works also as a heat pump), which exchange heat with two secondary loops, that are liquid coolant circuits. A concept of the complete e.TM integrated system for a passenger vehicle is indicated in Figure 4.1.

The primary loop is used to transfer heat between the two circuits of the secondary loop. As shown in Figure 4.2, the primary loop is a conventional vapor compression refrigeration system, composed of a compressor, a condenser, a receiver integrated with the condenser, an expansion valve and an evaporator. The secondary loop is made by two interconnected coolant liquid circuits; one is a hot coolant circuit that receives heat from the condenser, the other is a

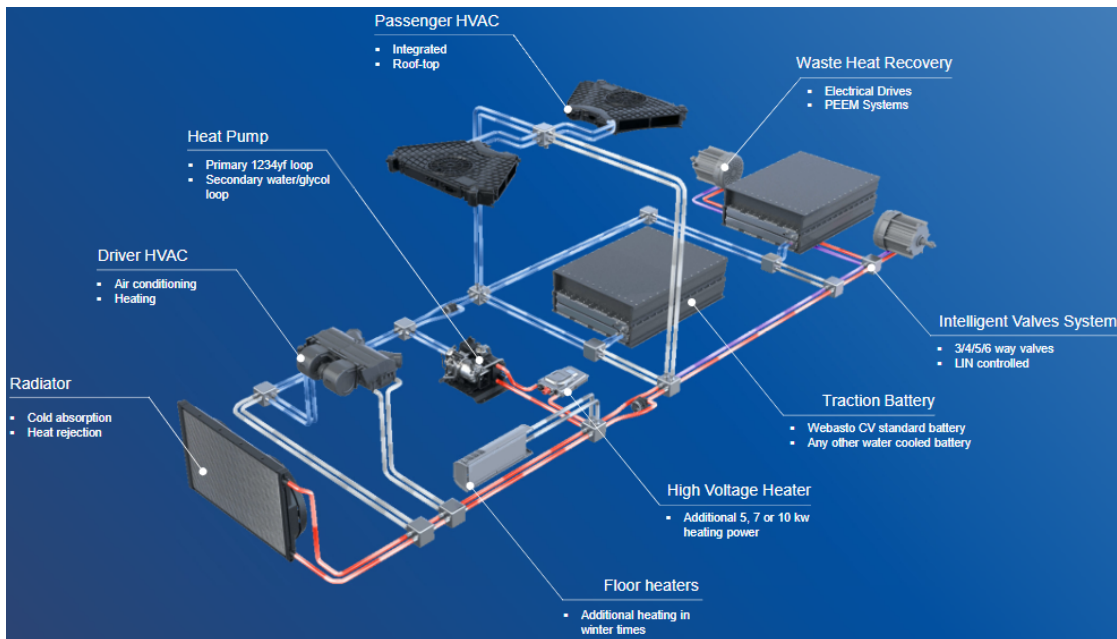


Figure 4.1: Integrated thermal management system for a 5 m electric bus equipped with 2 Webasto CV (commercial vehicle) standard battery.

cold coolant circuit that exchanges heat to the evaporator. The secondary loops are used to connect all the thermal loads of the vehicle - conditioning units, battery, PEEM – to the primary loop, removing heat from where it is generated and exchanging it with the internal vehicle devices using a heat exchanger or the external air by a radiator. The flow within the secondary loop is done by a mechanical pumping of the coolant. The integration of an Intelligent Valve system, managed by LIN (Local Interconnect Network) controlled valves, enables dynamic adjustments to the coolant loop configuration. This adaptation alters heat distribution across vehicle components based on its operational state (e.g., charging, parked, driving) and the specific needs of its subsystems. The configuration of the two circuits of the secondary loop varies according to the request from the vehicle thermal loads and to the external ambient conditions. This feature allows the system to switch between AC and heat pump mode without reversing the refrigerant flow.

A characteristic of the vehicle integrated e.TM system is that it is based on a modular approach, facing the challenge to define a scalable thermal management system and using different combination of existing parts in order to be flexible to fulfil the best vehicle thermal requests.

In a nutshell, with the thermal model defined, it could be possible to meet

4.1. INTEGRATED THERMAL MANAGEMENT CONCEPT

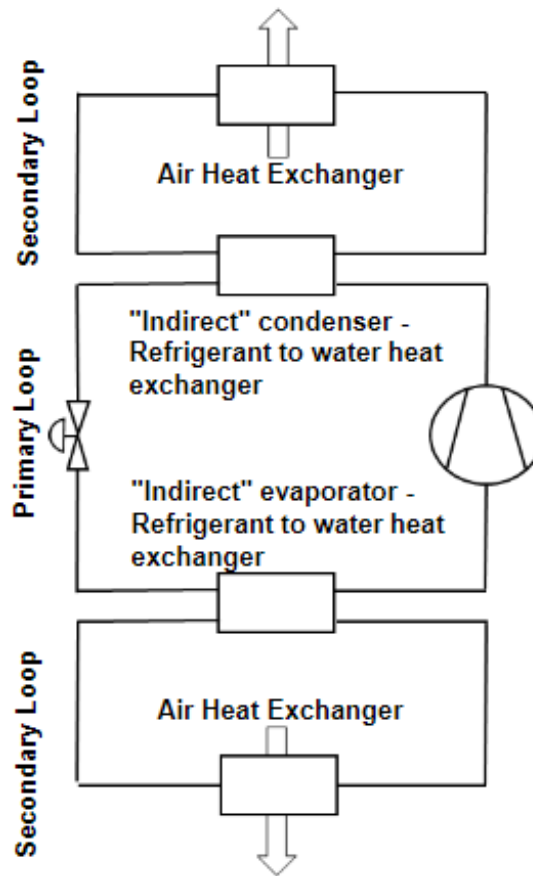


Figure 4.2: Scheme of the secondary loop concept

several customer specifications – i.e. Light Commercial Vehicles (LCVs), Heavy Duty Commercial vehicle (HDCVs), different busses sizes – and by means of defined model, as a cherry-picking, different components could be chosen to achieve the different thermal requests:

- Heat Pump (with defined thermal power),
- Coolant heaters,
- Passenger HVAC units,
- Driver HVAC units,
- Floor Heater units,
- Radiator,
- Battery,
- PEEM / electronic devices.

4.2 MODEL OF THE VEHICLE

The EVTMS analyzed in this thesis has been designed for a compact electric shuttle bus with dimensions of 5 m in length, 2 m in width and a height of 2.1 m. The distinctive feature of this bus is its autonomous driving technology which eliminates the need for a driver's compartment, thereby dedicating the entire cabin space to passengers. Therefore, the design forgoes a separate HVAC system for a driver.

The electric shuttle bus hosts several crucial subsystems including the PEEM, the battery system, and the cabin, all of which interact to maintain optimal operational performance. These subsystems, along with the integrated thermal management (e.TM) system, have been digitally modeled using Simscape, a simulation platform. This platform allows for an in-depth evaluation of the vehicle's performance, and facilitates the testing and development of the control system governing the e.TM system. Through Simscape, engineers can analyze the dynamic interactions between these subsystems under varying conditions, and refine the control algorithms to ensure reliable and efficient operation of the thermal management system.

4.2.1 PEEM SUBSYSTEM

The Power Electronics and Electric Motor (PEEM) subsystem is a vital component of the electric shuttle bus, responsible for the conversion and efficient management of electrical power within the vehicle. It encompasses several integral parts:

Electric Motor: Central to the PEEM, the electric motor boasts a peak power output of 130 kW. This motor powers the shuttle's wheels by transforming the electrical energy from the battery into kinetic force.

Inverter: Acting as an intermediary between the battery and the electric motor, the inverter changes the battery's DC output into AC for the motor's use. It's crucial in adjusting the motor's velocity and power output.

DC/DC Converters: There are two of these converters within the subsystem. Their primary function is to adjust the voltage levels to meet the specific needs of different electronic components within the shuttle. Collectively, they have a typical dissipation of about 585 W.

ADAS CPU: Standing for Advanced Driver Assistance Systems, the ADAS

4.2. MODEL OF THE VEHICLE

CPU is a crucial element that manages and processes data related to the shuttle's autonomous driving capabilities. This component is particularly notable for its heat dissipation, which amounts to around 850 W.

For the purpose of understanding and predicting the thermal behavior of the vehicle during operation, these components within the PEEM subsystem are modeled as thermal masses that exchange heat with the water/glycol coolant, as shown in Figure 4.3.

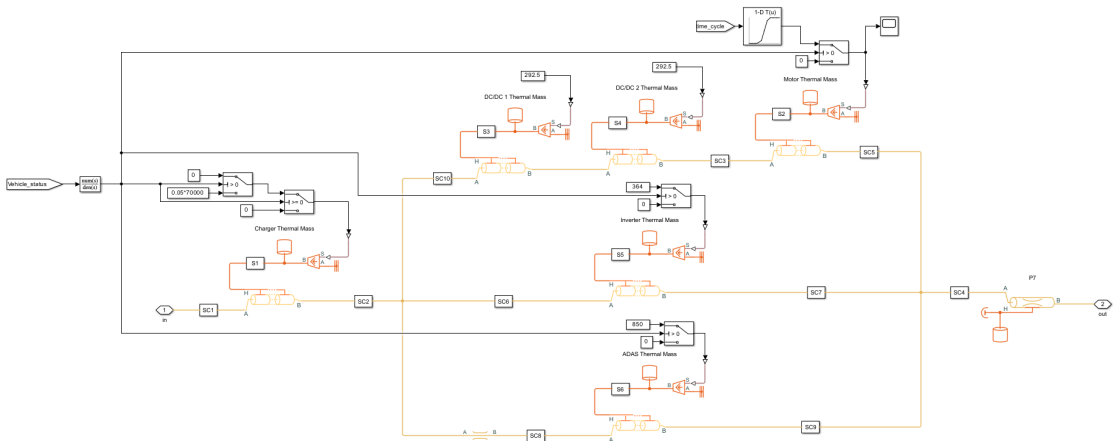


Figure 4.3: PEEM model

Each thermal mass is described by the equation:

$$W = m_H c_H \frac{dT_H}{dt} \quad (4.1)$$

where:

- m_H is the mass of the electronic device (kg).
- c_H is the specific heat of the mass material (J/ kg K).
- $\frac{dT_H}{dt}$ is the derivative over time of the mass temperature (K/s).
- W is the heat flow (W). This quantity is equal to the difference between the internal heat generation and the heat transferred from the mass to the coolant (W_H).

This model considers the internal heat generation of these components, which can be designated either as a consistent value or as a variable profile contingent on the specific driving cycle the vehicle is undergoing. Importantly, this internally generated heat doesn't remain trapped within these components.

Instead, it is effectively dissipated through convection and conduction mechanisms to a water-glycol coolant that is actively pumped through channels carved inside them. This ensures that the components remain within their optimal temperature range, preserving their efficiency and lifespan, while also preventing any potential thermal-related malfunctions or damages.

Below are listed all the equations pertaining to the water-glycol coolant in the PEEM model.

HEAT TRANSFER AT THE CHANNEL WALL

The heat transfer between the coolant and the channel wall is modelled as:

$$W_H = W_{conv} + W_{cond} \quad (4.2)$$

where:

- W_{conv} is the heat transfer that occurs through convection (W).
- W_{cond} is the heat transfer that occurs through conduction (W).

The conduction component is:

$$W_{cond} = \frac{k_l S_H}{D} (T_H - T_l) \quad (4.3)$$

where:

- k_l is the thermal conductivity of the water/glycol coolant (W/m K).
- S_H is the surface area of the coolant channel inside a PEEM component (m^2).
- D is the hydraulic diameter of the channel (m).
- T_H is the channel wall temperature (K).
- T_l is the coolant temperature inside the channel (K).

The convection component is:

$$W_{conv} = |\dot{m}_{avg}| c_{p,avg} (T_H - T_{in}) \left[1 - \exp\left(-\frac{h S_H}{|\dot{m}_{avg}| c_{p,avg}}\right) \right] \quad (4.4)$$

where:

- \dot{m}_{avg} is the average mass flow rate through the channel (kg/s).

4.2. MODEL OF THE VEHICLE

- $c_{p,avg}$ is the average coolant specific heat (J/kg K).
- T_{in} is the coolant inlet temperature (K).
- h is the convective heat transfer coefficient at the channel wall (J/ m² K).

The convective heat transfer coefficient (h), in equation 4.4, is equal to:

$$h = \frac{Nu k_{avg}}{D} \quad (4.5)$$

where k_{avg} represents the average thermal conductivity of the coolant throughout the channel, and Nu denotes the average Nusselt number in the channel, calculated using the Dittus-Boelter correlation:

$$Nu = a Re^b Pr^c. \quad (4.6)$$

Here, a , b and c are adjustable coefficients, while Re and Pr are the Reynolds number and the Prandtl number, respectively.

PRESSURE LOSS DUE TO FRICTION

To model pressure losses within the channels, we applied the Haaland Correlation, which is computed within the pipe block of Simscape separately for each half of the channel. The first half corresponds to the section adjacent to the inlet, while the second half corresponds to the section adjacent to the outlet. In laminar flow conditions, pressure losses are calculated as follows:

$$\begin{aligned} \Delta p_{f,in} &= \frac{\nu \lambda}{2D^2 S} \frac{L+L_{add}}{2} \dot{m}_{in} \\ \Delta p_{f,out} &= \frac{\nu \lambda}{2D^2 S} \frac{L+L_{add}}{2} \dot{m}_{out} \end{aligned} \quad (4.7)$$

where:

- ν is the fluid kinematic viscosity (m²/s).
- λ is the value of the laminar friction constant for Darcy friction factor parameter (-).
- S is the channel cross-section area (m²).
- L is the channel length (m).
- L_{add} is the value of the aggregate equivalent length of local resistances parameter (m), i.e. an added straight-pipe length that results in equivalent losses to the resistances due to nonuniformities of the channel.

- \dot{m}_{in} is the inlet mass flow rate (kg/s).
- \dot{m}_{out} is the outlet mass flow rate (kg/s).

In turbulent flow conditions, pressure losses are calculated as follows:

$$\begin{aligned}\Delta p_{f,in} &= \frac{f}{2\rho S^2} \frac{L+L_{add}}{2} \dot{m}_{in} |\dot{m}_{in}| \\ \Delta p_{f,out} &= \frac{f}{2\rho S^2} \frac{L+L_{add}}{2} \dot{m}_{out} |\dot{m}_{out}|\end{aligned}\quad (4.8)$$

where:

- f is the Darcy friction factor (-). This is approximated by the empirical Haaland equation and is based on the surface roughness specification, ϵ , and the channels hydraulic diameter:

$$f = \left\{ -1.8 \log_{10} \left[\frac{6.9}{Re} + \left(\frac{\epsilon}{3.7D} \right)^{1.11} \right] \right\}^{-2} \quad (4.9)$$

- ρ = fluid density in the channel (kg/m³).

MOMENTUM BALANCE

The momentum conservation equation for the water-glycol coolant flowing through the channels accounts for fluid dynamic compressibility while disregarding fluid inertia and hydrostatic changes resulting from elevation differences between the inlet and outlet of the PEEM components. This equation is computed for each half of the channel length as follows:

$$\begin{aligned}p_{in} - p &= \Delta p_{f,in} \\ p_{out} - p &= \Delta p_{f,out}\end{aligned}\quad (4.10)$$

where p , p_{in} and p_{out} are the coolant pressures in the channel (internal node of the pipe block), at the channel inlet and at the channel outlet.

MASS BALANCE

Considering the channel wall as rigid, the mass conservation equation is defined as:

$$\dot{m}_{in} + \dot{m}_{out} = V\rho \left(\frac{1}{\beta} \frac{dp}{dt} - \alpha \frac{dT}{dt} \right) \quad (4.11)$$

where:

4.2. MODEL OF THE VEHICLE

- V is the channel fluid volume (m^3).
- β is the isothermal bulk modulus in the channel (Pa).
- α is the isobaric thermal expansion coefficient in the channel (K^{-1}).
- T is the coolant temperature in the channel (K).
- t is the time (s).

ENERGY BALANCE

Accounting for the same assumptions made for the momentum and mass conservation equations, the energy conservation equation for the channel is formulated as:

$$\left. \frac{\partial(\rho u)}{\partial p} \right|_T \frac{d(p)}{dt} V + \left. \frac{\partial(\rho u)}{\partial T} \right|_p \frac{d(T)}{dt} V = \phi_{in} + \phi_{out} + W_H \quad (4.12)$$

where:

- $\left. \frac{\partial(\rho u)}{\partial p} \right|_T = \left(\frac{\rho h}{\beta} - T\alpha \right) V$
- $\left. \frac{\partial(\rho u)}{\partial T} \right|_p = (c_p - h\alpha) V$
- u is the specific internal energy (J/kg).
- ϕ_{in} is the energy flow at the channel inlet (W).
- ϕ_{out} is the energy flow at the channel output (W).
- h is the specific enthalpy in the channel (J/kg).

4.2.2 BATTERY SUBSYSTEM

The battery pack of this shuttle bus is made of two Webasto CV standard batteries with a capacity of 35 kWh for each of them. The battery's architecture is split into two distinct modules. Each module is equipped with coolant plates that play a crucial role in maintaining the temperature of the battery by either cooling or heating it. As shown in Figure 4.4, each battery module has been

modeled in Simscape as a thermal mass with an internal heat generation that exchanges heat through a convection mechanism with the coolant plate and through conduction with the battery case.

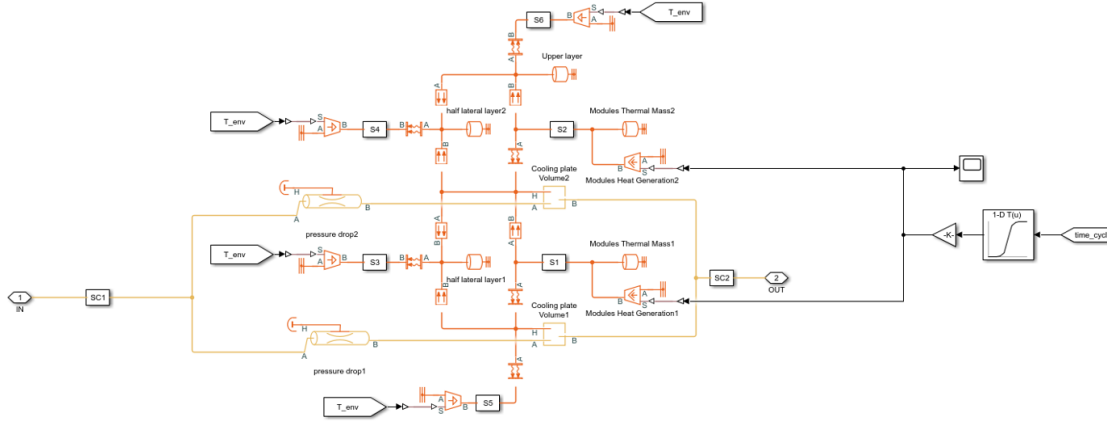


Figure 4.4: Battery model

INTERNAL HEAT GENERATION

The heat generated by the battery varies based on whether the vehicle is charging or in motion:

- **Charging Mode:** The magnitude of heat produced during the charging phase is influenced by two primary factors: the ambient temperature and the rate of charging. A higher charging speed or a more elevated ambient temperature would typically lead to increased heat generation.
- **Driving Mode:** When the vehicle is on the move, the heat generation is primarily dictated by the driving cycle, specifically the vehicle's velocity and acceleration profiles.

ENERGY BALANCE

Although the equations governing energy conservation in the thermal masses, as well as mass conservation, momentum conservation, and pressure losses in the coolant, remain consistent with those employed in the PEEM model (subsection 4.2.1), the rate of energy accumulation in the coolant plate volume is described by the following equation:

$$\left[\left(\frac{h}{\beta} - \frac{T\alpha}{\rho} \right) \frac{dp}{dt} + (c_p - h\alpha) \frac{dT}{dt} \right] pV = \phi_{in} + \phi_{out} + W_H \quad (4.13)$$

4.2. MODEL OF THE VEHICLE

The heat transfer rate (W_H) between the battery module and the coolant plate is determined by using the overall heat transfer coefficient (U_H) for the multi-layered section extending from the center of the battery module to the center of the coolant plate. Therefore, W_H is calculated as follows:

$$W_H = U_H S_H (T_{batt} - T) \quad (4.14)$$

where:

- S_H is the contact area between the battery module and the coolant plate.
- T_{batt} is the temperature at the battery module center.
- T is the water-glycol coolant temperature.

Apart from the convection mechanism between the battery and the coolant plates, the model also integrates other vital thermal dynamics:

- **Conduction:** The model considers the thermal conduction that takes place between the battery module and the casing, which can play a significant role in temperature fluctuations, especially during peak load conditions.
- **External Convection:** In addition to the internal thermal mechanisms, the battery's convection towards the external environment is also modeled. This ensures that the model provides a comprehensive understanding of the battery's temperature dynamics in varied ambient conditions.

These two heat transfer mechanisms are calculated similarly to equation 4.14, with the distinction lying in the sequence of layers being considered. In summation, this Simscape-based thermal model offers an intricate depiction of a battery's thermal behavior, considering both internal and external influences.

4.2.3 CABIN SUBSYSTEM

The cabin of the electric shuttle bus is modeled in Simscape to ensure a comprehensive understanding of its thermal dynamics. A picture of the model is shown in figure 4.5.

The intricacies of this model can be understood as follows:

Passenger Dynamics: For a realistic simulation, the model factors in the presence of passengers within the cabin. Each passenger:

- Occupies an approximate volume of 0.375 m^3 .

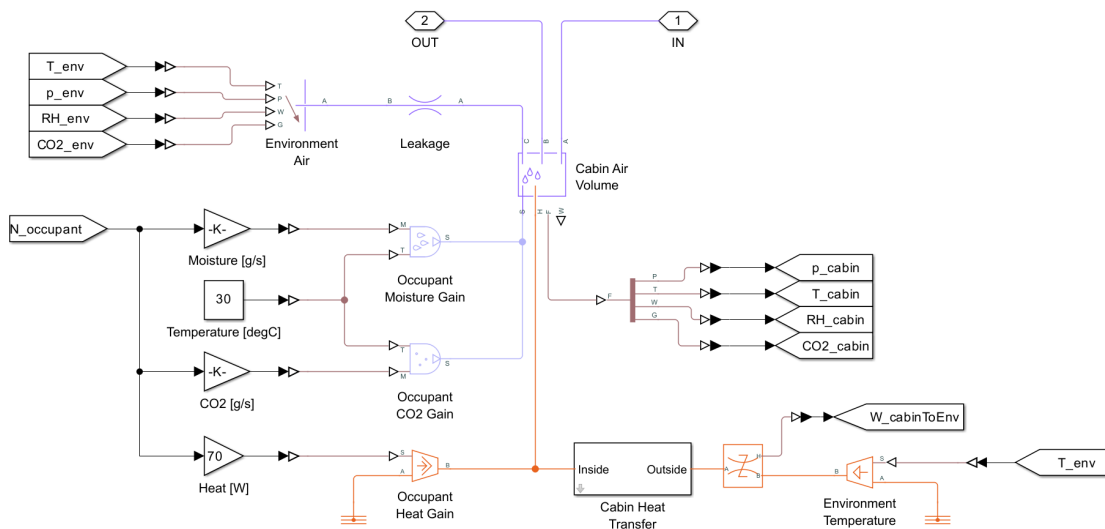


Figure 4.5: Cabin model

- Contributes 70 W of sensible heat.
- Emits 0.04 g/s of water vapor at 30 °C.
- Releases 0.01 g/s of CO₂ at 30 °C.

Cabin Structure: The cabin's external surface area amounts to 33 m². Notably, 17.9 m² of this area is made up of glass. The remaining portion of the cabin wall comprises a multi-layered structure. Moving from the inside outwards, these layers include:

- Polypropylene
- Insulation
- Steel
- Air
- Another layer of Steel

Each surface of the cabin – front, back, right, left, top, and bottom – is modeled to account for energy exchange with the external environment. This exchange is calculated similarly to equation 4.14, considering internal convection, wall conduction, and external convection.

4.2. MODEL OF THE VEHICLE

Solar Radiation: Solar radiation is modeled using a heat flow rate source block in Simscape, as primarily vertical, targeting the top surface of the cabin. The internal equipment and floor are heated by the sun's rays that pass through the top glass surface, which covers an area of 2.5 m². The transmission coefficient for this glass is 0.486, indicating the proportion of solar radiation that penetrates through.

Air Exchange: Air exchange with the outside environment is facilitated in two ways:

1. Through the HVAC system which regulates and maintains the internal air quality and temperature.
2. Via a resistance model that mimics the natural air leakage of the cabin, representing minor imperfections in sealing or intentional ventilation gaps.

Moist Air Volume: The cabin's internal air volume is represented as a 0-dimensional space where both mass and energy conservation equations are applied. This volume measures 18.7 m³. Additionally, the seats and internal equipment within the cabin occupy a space of 0.48 m³. The pressure and temperature inside the cabin evolve based on the compressibility and thermal capacity of the moist air volume. Liquid water condenses out of the moist air volume when it reaches saturation.

The net flow rates into the moist air volume inside the cabin are:

$$\begin{aligned}
 \dot{m}_{net} &= \dot{m}_{in} - \dot{m}_{out} + \dot{m}_{leakage} - \dot{m}_{condense} + \dot{m}_{wS} + \dot{m}_{gS} \\
 \phi_{net} &= \phi_{in} - \phi_{out} + \phi_{leakage} + W_H - \phi_{condense} + \phi_S \\
 \dot{m}_{w,net} &= \dot{m}_{w,in} - \dot{m}_{w,out} + \dot{m}_{w,leakage} - \dot{m}_{condense} + \dot{m}_{wS} \\
 \dot{m}_{g,net} &= \dot{m}_{g,in} - \dot{m}_{g,out} + \dot{m}_{g,leakage} + \dot{m}_{gS}
 \end{aligned} \tag{4.15}$$

where:

- \dot{m} refers to a mass flow rate (kg/s).
- ϕ refers to an energy flow rate (W).
- The subscripts w and g indicates the properties of water vapor and trace gas, respectively.
- $\dot{m}_{leakage}$ is the air mass flow that leaks through the cabin structure.

- $\dot{m}_{condense}$ is the rate of condensation.
- $\phi_{condense}$ is the rate of energy loss from the condensed water.
- ϕ_S is the rate of energy added by the sources of moisture and trace gas.
- \dot{m}_{wS} and \dot{m}_{gS} are mass flow rates of water and gas, respectively, determined by the moisture and trace gas sources.

Water vapor mass conservation relates the water vapor mass flow rate to the dynamics of the moisture level in the internal moist air volume:

$$\frac{dx_{wI}}{dt} \rho_I V + x_{wI} \dot{m}_{net} = \dot{m}_{w,net} \quad (4.16)$$

where:

- x refers to the mass fraction.
- The subscript I indicates the properties of the internal moist air volume.
- V is the moist air volume inside the cabin (m^3).

Similarly, trace gas mass conservation relates the trace gas mass flow rate to the dynamics of the trace gas level in the internal moist air volume:

$$\frac{dx_{gI}}{dt} \rho_I V + x_{gI} \dot{m}_{net} = \dot{m}_{g,net} \quad (4.17)$$

Mixture mass conservation relates the mixture mass flow rate to the dynamics of the pressure, temperature, and mass fractions of the internal moist air volume:

$$\left(\frac{1}{p_I} \frac{dp_I}{dt} - \frac{1}{T_I} \frac{dT_I}{dt} \right) \rho_I V + \frac{R_a - R_w}{R_I} (\dot{m}_{w,net} - x_w \dot{m}_{net}) + \frac{R_a - R_g}{R_I} (\dot{m}_{g,net} - x_g \dot{m}_{net}) = \dot{m}_{net} \quad (4.18)$$

where:

- R refers to the specific gas constant.
- The subscript a indicates the properties of dry air

The equation of state relates the mixture density to the pressure and temperature:

$$p_I = \rho_I R_I T_I \quad (4.19)$$

The mixture specific gas constant is:

$$R_I = x_{aI} R_a + x_{wI} R_w + x_{gI} R_g \quad (4.20)$$

4.2. MODEL OF THE VEHICLE

Flow resistance and thermal resistance are not modeled in the chamber, so we have that $p_{in} = p_{out} = p_{leakage} = p_I$.

When the moist air volume reaches saturation, condensation may occur. The specific humidity at saturation (subscript ws) is:

$$x_{wsI} = \psi_{ws} \frac{R_I}{R_w} \frac{p_{wsI}}{p_I} \quad (4.21)$$

where:

- ψ_{ws} is the relative humidity at saturation (typically 1).
- p_{wsI} is the water vapor saturation pressure evaluated at T_I .

The rate of condensation is:

$$\begin{aligned} \dot{m}_{condense} &= 0, \text{ if } x_{wI} \leq x_{wsI} \\ \dot{m}_{condense} &= \frac{x_{wI} - x_{wsI}}{\tau_{condense}} \rho_I V, \text{ if } x_{wI} > x_{wsI} \end{aligned} \quad (4.22)$$

where $\tau_{condense}$ is the value of the condensation time constant.

The condensed water is subtracted from the moist air volume, as shown in the conservation equations. The energy associated with the condensed water is:

$$\phi_{condense} = \dot{m}_{condense} (h_{wI} - \Delta h_{vapI}) \quad (4.23)$$

where Δh_{vapI} is the specific enthalpy of vaporization evaluated at T_I .

Other moisture and trace gas quantities are related to each other as follows:

$$\begin{aligned} \psi_{wI} &= \frac{y_{wI} p_I}{p_{wsI}} \\ y_{wI} &= \frac{x_{wI} R_w}{R_I} \\ r_{wI} &= \frac{x_{wI}}{1 - x_{wI}} \\ y_{gI} &= \frac{x_{gI} R_g}{R_I} \\ x_{aI} + x_{wI} + x_{gI} &= 1 \end{aligned} \quad (4.24)$$

where y refers to the mole fraction.

This Simscape model of the cabin is integral for understanding and optimizing the thermal comfort and safety of the passengers, ensuring that the electric shuttle bus operates efficiently under various external conditions. While modeling the cabin as a 0-dimensional volume ensures a fast computational speed, the drawback is that it is not possible to test operating modes such as the defrosting

and defogging of the windshield. To do that we would need a 3-dimensional model of the cabin to simulate the air ventilation directed towards the glass.

4.3 COMPONENTS OF THE ITMS

The thermal management system (TMS) of the electric shuttle bus is engineered to ensure optimal performance and comfort by regulating temperatures across various components. The major elements of this system include:

Liquid Coolant Loop: The liquid coolant loop comprises pipes, two-way and three-way valves, and T-joints. These components work in harmony to uphold the principles of mass, momentum, and energy conservation (modelled similarly to the equations listed in the subsection 4.2.1), while the effects of fluid inertia and heat dissipation to the ambient are disregarded for simplicity.

Heat Exchangers: The TMS incorporates a radiator and other air/liquid heat exchangers, tasked with managing the temperatures of the cabin, battery, and PEEM subsystem.

- **Radiator:** An air/liquid microchannel heat exchanger in which the two fluids are moving perpendicular to each other (cross flow). It is engineered with a heat rejection capacity of 26.9 kW to effectively dissipate excess heat into the ambient.
- **Battery, and PEEM Heat Exchangers:** liquid/liquid plate heat exchangers in which the two fluids are moving in parallel, but in opposite directions (counter flow).

The effectiveness-NTU method is employed to calculate the heat transfer between fluids within each heat exchanger. The mass conservation, momentum conservation, and energy conservation equations for the fluids, remain consistent with those employed in subsection 4.2.1.

HVAC System: The Heating, Ventilation, and Air Conditioning (HVAC) system is segmented into roof heat exchanger units, known as SP80, and floor heaters, all of which are air/liquid tube-fin heat exchangers in which the two fluids are moving perpendicular to each other (cross flow).

- **SP80 Units:** Each SP80 unit consists of four banks of tubes - two dedicated for heating and two for cooling. They are characterized by a nominal heating capacity of 4.32 kW and a nominal cooling capacity of 4.2 kW.

4.4. PEEM PLACEMENT OPTIMIZATION

During cooling scenarios, the condensation of humidity on the air side of the cabin heat exchanger is taken into account.

- **Floor Heaters:** These are banks of tubes with a nominal heating capacity of 2.2 kW, designed to provide supplementary heating to the cabin.

Heat Pump: Utilizing the refrigerant R1234yf, the heat pump is a pivotal part of the TMS.

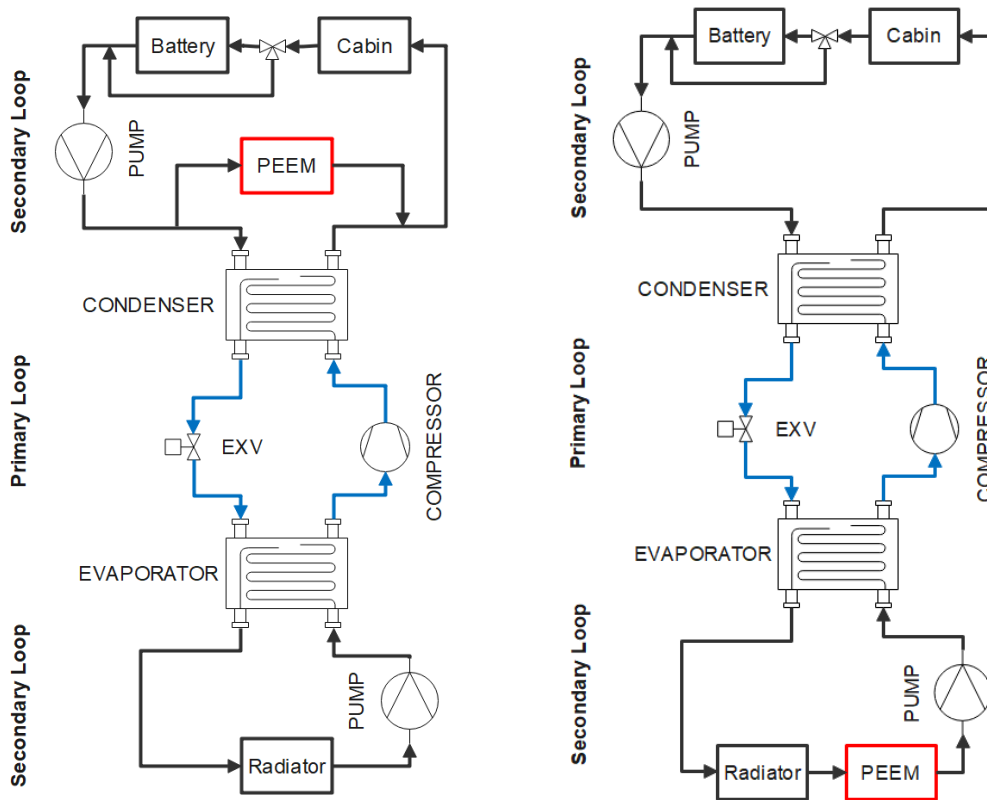
- **Power Supply and Consumption:** The compressor within the heat pump operates on a 400V supply, with a maximum electrical consumption of 3.5 kW.
- **Heat Exchangers:** Both the condenser and evaporator within the heat pump are designed as gasketed plate heat exchangers.
- **Heating and Cooling Capacities:** The heat pump can provide a maximum heating capacity of 11.5 kW and a maximum cooling capacity of 7.5 kW, ensuring a comfortable cabin environment across a broad range of external conditions.

The integration of these components within the thermal management system ensures a harmonious interaction between the vehicles subsystems. Through sophisticated control and effective heat transfer mechanisms, the TMS significantly contributes to the vehicles performance, longevity, and the comfort of its occupants.

4.4 PEEM PLACEMENT OPTIMIZATION

Integrating thermal sources and loads within a singular liquid loop offers the flexibility to alter the system's layout by adjusting the valves' states either open or closed. This adjustment allows for the alteration of the coolant's flow path to optimize the system's energy balance. To maximise the waste heat recovery, especially in cold environments, and thus elevate the system's energy efficiency, we assessed the placement of the PEEM system within the coolant circuit. This is vital as the PEEM system is the primary contributor to energy dissipation. We explored the positioning of the PEEM in two distinct configurations for the ITMS working in heat pump mode, illustrated in Figure 4.6:

- **Layout 1:** PEEM positioned within the hot coolant circuit, i.e. on the condenser side, in parallel to the heat pump's condenser (See Figure 4.6a).



(a) Layout 1: PEEM subsystem on the con-

(b) Layout 2: PEEM subsystem on the evaporator side.

Figure 4.6: Schematic representation the two different collocations of the PEEM subsystem that are analysed.

- Layout 2: PEEM located within the cold coolant loop, i.e. on the evaporator side, sequentially connected to the radiator (Refer to Figure 4.6b).

In heat pump mode, the first configuration directly contributes to heating both the cabin and the battery. The contribution of the PEEM in the second configuration is indirect, as it exchanges heat with the coolant on the evaporator side. This exchange leads to a rise in the coolant temperature at the evaporator, which in turn improves the heat pump's coefficient of performance (COP). Hence, with the same power supplied to the compressor, a higher heating power is achieved at the condenser. Essentially, the heat dissipated by the PEEM is absorbed by the refrigerant evaporating through the evaporator and is then transported to the condenser.

Kiss et al. [72] conducted a study employing steady-state simulations of their ITMS. Their results demonstrated that when the PEEM is positioned within the hot coolant loop, the system's efficiency in heat pump mode is enhanced.

4.4. PEEM PLACEMENT OPTIMIZATION

However, vehicles often operate outside of steady-state conditions. Typically, a vehicle's battery requires heating primarily at startup, as subsequent internal heat generation enables it to maintain its temperature. Given this, our goal is to validate the findings of Kiss et al. in dynamic conditions.

In a steady-state scenario, the temperature of a mass with intrinsic heat generation, such as the PEEM, is greater than the temperature of the circulating coolant. In this context, all internally generated heat is transferred to the fluid. On the other hand, this isn't necessarily the case under dynamic conditions. Therefore, we are yet to ascertain whether, with the PEEM positioned on the condenser side, the ITMS can effectively recover the waste heat.

4.4.1 TEST CONDITION

The e.TM system was simulated using the software Matlab Simscape. In particular, we considered the integrated thermal management system of a 5 m electric bus, working in heat pump mode. In the first layout of the e.TM system, the valves make the hot coolant circuit passes through the condenser, the PEEM, the cabin HVAC units and the battery, while the cold coolant circuit through the evaporator and the radiator. In the second layout, the hot coolant circuit passes through the condenser, the cabin HVAC units and the battery, while the cold coolant circuit though the evaporator, the radiator and the PEEM.

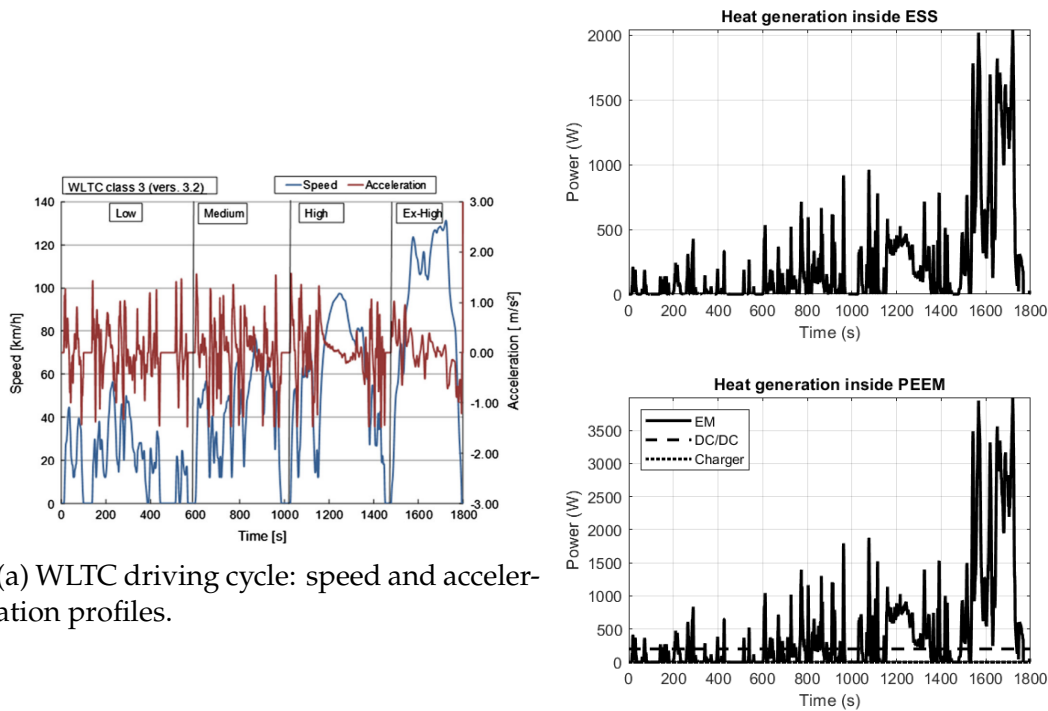
The PEEM subsystem is composed, in the present study, of three elements placed in series along the coolant pipe; they are an AC/DC charger, an e-machine (consisting in the electric motor and the inverter) and a DC/DC converter. The electric motor is a 3-phase, 6-pole induction machine, whose peak power and efficiency are 150 kW and ~95% respectively.

The battery pack is made of 2 batteries of 35 kWh, each one cooled or heated by a cold plate.

The cabin compartment is modelled as a volume of 24 m³ of air, which is heated up by 2 floor heaters and 3 HVAC units, located in the roof.

All these three subsystems are modelled as thermal masses that exchange heat with the coolant loop and the environment, and have an internal heat generation. To define the power dissipation profile of the electric motor and of the battery, we considered the vehicle running on the WLTC (Worldwide harmonized Light duty Test Cycle) driving cycle [73]. This is a driving cycle that has a duration of 1800 s, which is divided into 4 segments: (i) a low speed

segment that lasts 589 s, (ii) a medium speed segment that lasts 433 s, (iii) a high speed segment that lasts 455 s and finally (iv) an extra high speed segment that lasts 323 s. The driving cycle speed and heat generation profiles are illustrated in Figure 4.7. Regarding the AC/DC charger, the DC/DC converter and the



(a) WLTC driving cycle: speed and acceleration profiles.

(b) WLTC driving cycle: battery (ESS) and motor heat generation profiles.

Figure 4.7: Worldwide harmonized Light duty Test Cycle.

cabin, the internal heat generations were defined as follows:

- 0 W in the charger, because we are simulating a driving condition, so the charger is not working,
- 200 W in the DC/DC converter,
- 700 W in the cabin, due to the presence of 10 passengers.

The e.TM system was simulated in 3 cold climate conditions, where the environment temperature was set to 0 °C, 5 °C and 10 °C. The same values of temperature were set for the initial condition of the system. In all these tests, the percentage of cabin air recirculation was fixed to guarantee 15 m³/h of fresh air per person, as written in the standard VDV 236 [67], in order to maintain a

4.4. PEEM PLACEMENT OPTIMIZATION

certain air quality inside the cabin [59] [56] [61]. The heating mode was analysed considering the thermal management system working with the heat pump at the maximum capacity, therefore with the compressor operating at the maximum speed; while the electric heaters were kept off. So, the heating source comes from the condenser and the PEEM waste heat which is recovered to heat up the cabin and the battery pack.

To analyse the performance of the two e.TM system layouts, we fixed the target temperatures of the cabin and the battery at 20 °C and 10 °C respectively. If the cabin temperature is still smaller than 20 °C, but the battery temperature has already reached 10 °C, the valves would change the hot coolant circuit path to switch the battery from heating mode to equalization. In this mode, the battery is separated from the primary coolant circuit and is linked to a separate loop, where a pump makes the coolant circulate through the battery. The aim of the equalization mode is to homogenise the temperature field inside the battery pack, so that all the battery cells maintain the same performance. We stopped the simulation when both the target temperatures were reached and we used the electric energy spent and the elapsed time until this point, as key parameters to assess the performance of the system.

4.4.2 RESULTS

The results of these simulations are reported in Figure 4.8, Figure 4.9 and Figure 4.10.

Figure 4.8 shows the amount of power that is recovered from the PEEM every instant and is used to heat up the cabin and the battery. In particular, the curves are relative to the two layouts described previously, operating at environment temperature equal to 0 °C. They show that in the first configuration, the e.TM system is not able to remove heat from the PEEM components, which is, instead, heated up by the coolant. Contrary, in the second configuration, the e.TM system cools down the PEEM. But it can recover a considerable amount of power only in the period of time close to the end of the WLTC driving cycle (1800 s), when the vehicle speed is higher (therefore the heat generation inside the PEEM components is greater). The results in the cases of environment temperature of 5 °C and 10 °C have not been plotted because they would have shown the same behaviour for the two secondary loop layouts.

Figure 4.9 reveals the evolution in time of the cabin temperature, in the cases

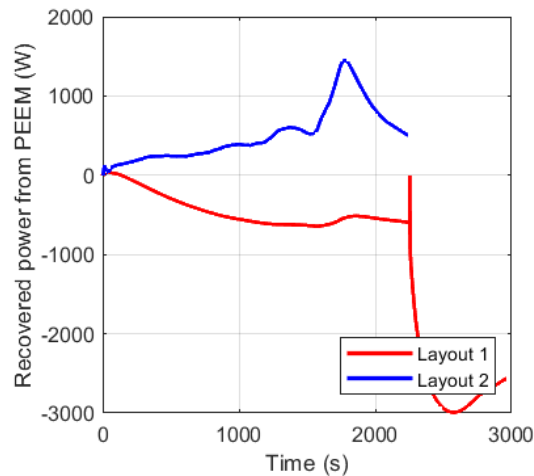


Figure 4.8: Comparison of the recovered power from the PEEM subsystem, between the two secondary loop layouts. These data are showed for the case of environment temperature equal to 0 °C.

of environment temperature equal to 0 °C, 5 °C and 10 °C. As a consequence of the results in Figure 4.8, with the second layout of the system, the heating power delivered to the cabin is greater compared to the first configuration. Therefore, the cabin temperature reaches the target value after a shorter period. When the battery reach 10 °C, the battery is bypassed, thanks to valves regulation, and switches in equalization mode. As a result, an immediate reduction of the thermal load occurs, increasing the heating power delivered to the cabin. Therefore, the temperature curves in Figure 4.8 become steeper.

In Figure 4.10, the comparison of the battery temperature between the two system layouts is shown for all the environment conditions studied. In the cases of environment temperature equal to 0 °C and 5 °C, the battery heating process is slightly faster with the second system configuration, while at 10 °C the two curves are superimposed because the battery is in equalization mode for all the duration of the test. Therefore, in this last case, the evolution of the temperature is dependent only on the heat generated inside the battery and on the dissipation towards the environment.

Finally, in table 4.1 are reported the two most significant results for comparing the performance of the two system layouts, therefore the electric energy consumed by the e.TM system and the time required to reach the target cabin and battery temperatures. These data show that the convenience of the second layout over the first one is significant only at 0 °C because, in the other two cases,

4.4. PEEM PLACEMENT OPTIMIZATION

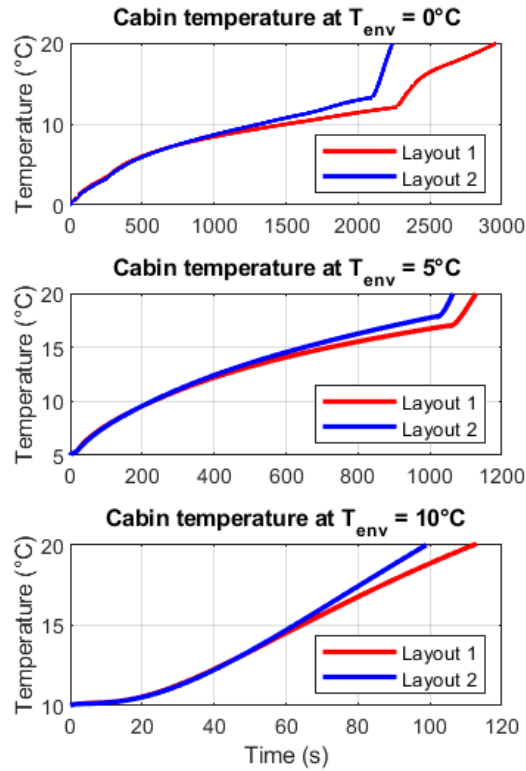


Figure 4.9: Comparison of the evolution in time of the cabin temperature, between the two secondary loop layouts. The data are showed in the cases of environment temperature (T_{env}) equal to 0°C , 5°C and 10°C .

the target conditions are reached before the beginning of the last two segments of the WLTC driving cycle, which are the most demanding. Being the speed of the vehicle quite low in the first period of the driving cycle, in this phase we do not have a significant heat generation inside the electric motor, which is the principal thermal load of the PEEM.

Table 4.1: Energy consumed and time required values to reach the cabin and battery target temperatures.

	Environment temperature					
	0°C		5°C		10°C	
Results	Layout 1	Layout 2	Layout 1	Layout 2	Layout 1	Layout 2
Energy (Wh)	4980	3631	2014	1873	197	165
Time (s)	2965	2239	1128	1064	113	99

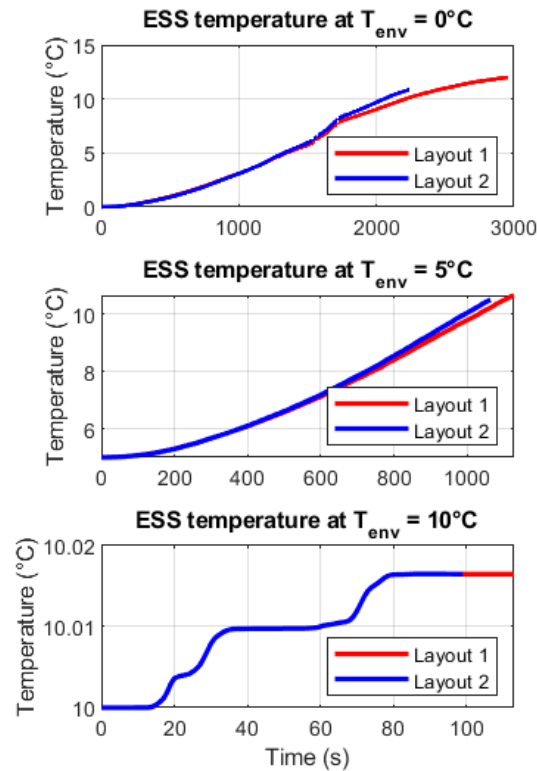


Figure 4.10: Comparison of the evolution in time of the battery temperature, between the two secondary loop layouts. The data are showed in the cases of environment temperature (T_{env}) equal to 0°C , 5°C and 10°C .

4.4.3 DISCUSSION

We studied the thermal behaviour of a 5 m electric bus, running on the WLTC driving cycle in a cold weather, and we observed the benefits in terms of waste heat recovery given by a vehicle integrated thermal management system. Our focus was on the evaluation of the possibility, thanks to the secondary loop concept, to recover the power dissipated in heat by the PEEM. In particular, two different layouts for the secondary loop were examined. In the first one, the PEEM was placed along the hot coolant circuit, parallel to the heat pump condenser, while in the second one, it was connected in series to the radiator. Regarding this last configuration, the PEEM can be moved upstream and downstream the radiator during the cooling and heating modes respectively, by switching the opening and closing of the valves.

We simulated the heating mode of our e.TM system in three environment conditions (i) 0°C , (ii) 5°C , (iii) 10°C and we tested its performance, in terms

4.5. LAYOUT OF THE ITMS

of electric energy consumed and time required to heat the battery and the cabin until 10 °C and 20 °C, respectively. The results for the layout 1 showed that, during the WLTC driving cycle and in all ambient conditions studied, it is not possible to recover heat from the PEEM, because the hot coolant circuit temperature is higher than the temperature of the various PEEMs subsystems. On the contrary, the PEEM is cooled down adopting the layout 2, especially when the environment temperature is 0 °C.

As a consequence, implementing the layout 2, we obtained an improvement in the performance of the e.TM system, with respect to the layout 1. Both the electric energy and the time required to reach the cabin and battery target temperatures were reduced.

4.5 LAYOUT OF THE ITMS

The Integrated Thermal Management System (ITMS) of the electric shuttle bus, shown in Figure 4.11, is a comprehensive network aimed at ensuring optimal thermal conditions across various vehicle components. Heres a detailed layout of the system:

Core Components:

- **Radiators:** Two radiators are incorporated within the system. The primary radiator is part of the central thermal management, while an additional radiator, with a nominal heat rejection capacity of 6 kW, is specifically devoted to the passive cooling of the PEEM subsystem.
- **Heat Pumps:** The system houses two heat pumps that actively regulate the temperature across various zones within the vehicle.
- **Electric Coolant Heater:** Positioned within the hot coolant loop, this heater is crucial for compensating the heating power shortfall of the heat pump, particularly under extremely cold conditions.
- **SP80 Units and Floor Heater:** Two SP80 units and a floor heater are designated for managing cabin temperature, ensuring a comfortable environment for the passengers.
- **Liquid/Liquid Plate Heat Exchangers:** These are employed to actively control the temperature of both the PEEM and battery, ensuring they operate within the specified temperature ranges set by the manufacturers.

Dedicated Coolant Loops: Given the manufacturer specifications requiring a minimum coolant flow for both the battery and PEEM under all conditions, dedicated coolant loops have been designed. This ensures the necessary coolant flow, even when there's no immediate need for thermal management.

Placement of PEEM: Drawing from the insights of a previous study, the PEEM subsystem is strategically placed within the coolant loop on the evaporator side. This layout facilitates both waste heat recovery and efficient thermal management, especially crucial for the PEEMs performance and longevity.

Valve Management: The liquid coolant loop is precisely controlled by eight two-way valves and three three-way valves. This setup enables a broad spectrum of thermal management operations including:

- Cabin heating, ventilation, cooling, and dehumidification.
- Battery heating, cooling, and temperature equalization.
- Passive cooling (via the radiator) and active cooling (primarily utilized for waste heat recovery during heat pump mode) of the PEEM.

The design and layout of the ITMS are reflective of a holistic approach to thermal management, ensuring each critical component of the vehicle operates within its thermal comfort zone. This, in turn, significantly contributes to the overall efficiency, safety, and comfort features of the electric shuttle bus, making it a robust and reliable choice for autonomous public transportation.

4.5. LAYOUT OF THE ITMS

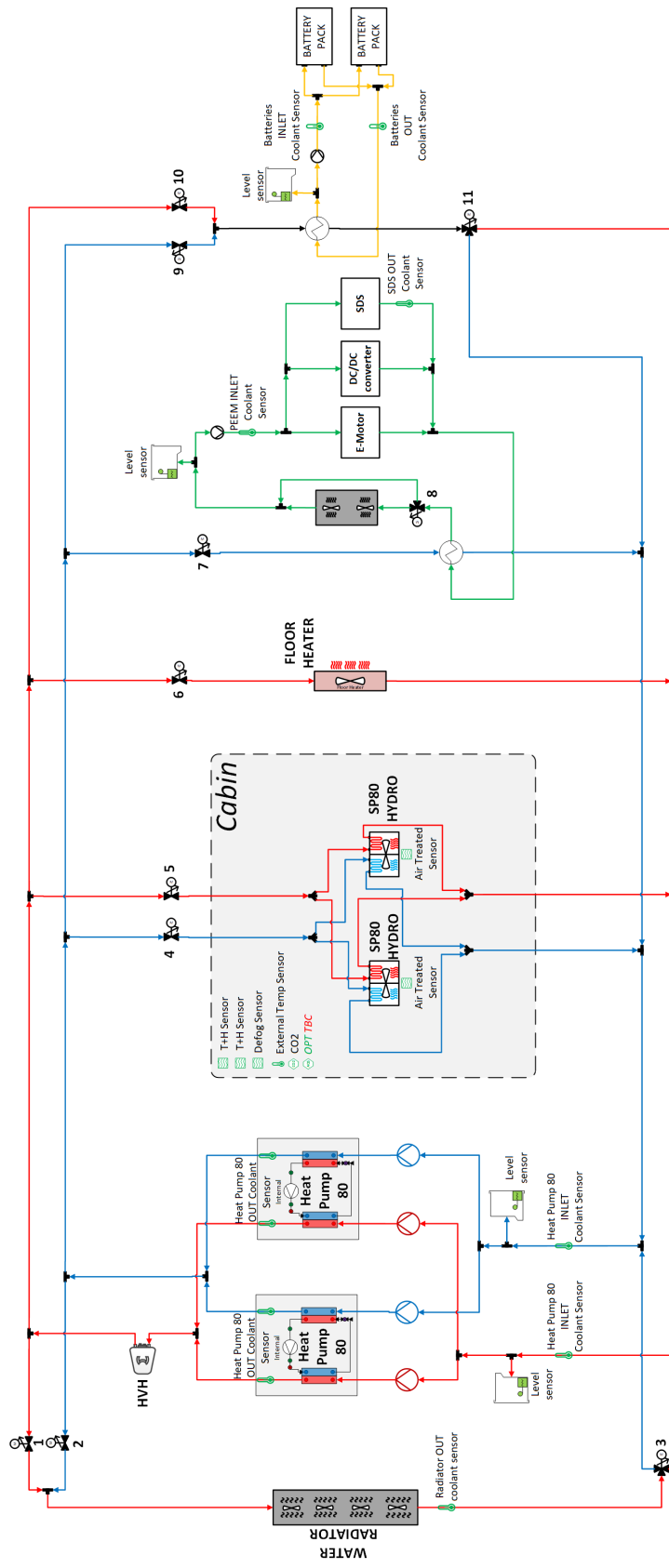


Figure 4.11: ITMS layout

5

Control strategy

5.1 WORKING MODE SELECTION

The operation of the ITMS is orchestrated through various working modes, each corresponding to a defined state of the coolant valves - essentially open or closed. The selection between these modes is governed by four primary states: the vehicle state, cabin state, battery state, and PEEM state. Here's a detailed explanation of the working mode selection based on these states:

Vehicle State:

1. Driving:

- All vehicle subsystems including the cabin, battery, and PEEM are continuously monitored and thermally managed as needed.
- The HVAC system has to maintain ventilation to comply with VDV 236 [67], ensuring CO₂ control with passengers onboard.
- PEEM and battery circuit pumps operate continuously.
- The only manual choice is whether the cabin should be managed in comfort mode or eco mode. Considering the interval of temperature allowed to be maintained within the cabin as defined by the VDV 236 standard [67], the comfort mode sets the cabin set-point temperature close to the upper limit of this interval in heating mode, and close to the bottom limit in cooling mode (therefore it aims to maintain the most comfortable environment). Contrarily the eco mode sets the cabin temperature set-point.

2. Charging:

5.1. WORKING MODE SELECTION

- Thermal management focuses solely on the battery and PEEM while the HVAC system is shut off.
 - Manual activation of cabin preconditioning in eco mode is available.
3. Parking: The ITMS is switched off, but the temperature of the battery is always monitored, and the control system can switch on the BTMS if the battery temperature falls out of the working interval, that is 10 °C – 35 °C.

Cabin State:

1. Off mode: Valves 4 and 5 (see Figure 4.11) are closed.
2. Ventilation mode: it is active when the cabin temperature error with respect to the set-point temperature is within 2.5 °C. In this mode, the coolant valves 4 and 5 are closed.
3. Cooling mode: it is initiated when the cabin temperature exceeds the set-point by 2.5 °C and, once activated, it remains active until the cabin temperature reverts to the set-point. In this scenario, the control system opens valve 4 while closing valves 5 and 6, directing cold coolant to the HVAC unit. Simultaneously, valve 1 is opened and valve 2 is closed to route the hot water to the radiator. Valve 3 establishes a connection between the radiator and the pipe returning to the condenser.
4. Heating mode: it is the exact opposite of cooling mode.
5. Dehumidification mode: it is triggered when the cabin temperature falls within the range specified for the Ventilation mode, but the relative humidity surpasses the threshold set by the VDV 236. In this control system, the maximum humidity limit has been adjusted from 70% to 60% to ensure that the relative humidity does not cross 70% during any overshoot. Once activated, this mode continues to operate until the relative humidity declines to a level that is at least 10% below the set threshold. In this mode, both valves 4 and 5 are opened to allow the circulation of both cold and hot coolant within the HVAC unit, with valve 6 remaining closed. Concurrently, valve 1 is opened and valve 2 is closed to divert a portion of the hot coolant flow to the radiator. This arrangement is necessitated by the higher thermal power exchange at the condenser compared to the evaporator, necessitating a balance between the sensible heat extracted from the air by the cold heat exchanger and the heat contributed by the hot heat exchanger within the HVAC unit. Valve 3 enables communication between the radiator and the pipe leading back to the condenser, ensuring a well-coordinated thermal management operation.
6. Dehumidification + cooling mode: it is triggered when the control system recognizes that both cooling and dehumidification are required. In this mode, the system configuration is the same as in cooling mode.

7. Dehumidification + heating mode: it is engaged when the control system identifies the need for both heating and dehumidification within the cabin. In this mode, valves 4, 5, and 6 are opened to facilitate dehumidification and heating. Conversely, valve 1 is closed and valve 2 is opened, allowing a portion of the cold coolant to flow to the radiator. This configuration ensures that the heating power within the HVAC unit surpasses the cooling power, thereby elevating the cabin temperature. Valve 3 establishes a link between the radiator and the pipe returning to the evaporator, ensuring a seamless flow of coolant.
8. Defrost mode: it is triggered when the windshield temperature dips below 0 °C. Valve-wise, this mode mirrors the Heating mode. The distinction arises in the operational dynamics of the HVAC unit, where the fans are ramped up to maximum speed and the air distribution flap is adjusted to channel hot airflow towards the windshield, aiding in ice melting. Due to the cabin being modeled as a 0-dimensional volume, it's impossible to simulate the Defrost mode (similarly, the Defogging mode), leading to its exclusion from the control system.

Battery State:

1. Off mode: it halts the battery pump and closes valves 9 and 10 to prevent coolant flow into the battery circuit's heat exchanger.
2. Equalization mode: it operates the battery pump at half speed with valves 9 and 10 closed.
3. Cooling mode: valve 9 is opened while valve 10 is closed. Valve 11 facilitates the connection between the liquid/liquid heat exchanger of the battery circuit and the pipe that returns to the evaporator (as depicted by the blue line in Figure \ref{fig:ITMS}). Valves 1, 2, and 3 are orchestrated to establish a link between the radiator and the hot coolant loop. The cooling mode is activated when the battery temperature rises above 35 °C and remains operational until the temperature descends below 30 °C.
4. Heating mode: The valve arrangement is reversed compared to the cooling mode. The heating mode kicks in when the battery temperature drops below 7°C and stays active until the temperature climbs above 10 °C.

PEEM State:

1. Off mode: In this state, valve 7 is closed, while valve 8 enables the coolant to bypass the radiator within the PEEM circuit.
2. Passive Cooling mode: Valve 7 remains closed, but valve 8 now channels the coolant to the radiator, utilizing ambient air to cool the PEEM.

5.2. HEAT PUMP CONTROL SYSTEM

3. Active Cooling mode: Here, valve 7 is opened to allow cold coolant to circulate through the liquid/liquid heat exchanger. The state of valve 8 is contingent on the operational mode of the rest of the system. If in heating mode, valve 8 directs the coolant to bypass the radiator, aiding in the recovery of all the heat dissipated by the PEEM. Conversely, if other subsystems are in cooling mode, valve 8 ensures the coolant flows through the radiator to optimize the cooling effect.

The working modes, defined by a meticulous valve management system, ensure a dynamic and responsive thermal regulation across all vehicle subsystems. Whether driving, charging, or parked, the ITMS adapts to varying conditions, balancing between maintaining comfort, ensuring safety, and optimizing energy efficiency.

5.2 HEAT PUMP CONTROL SYSTEM

If we include the cabin, the battery pack, and the PEEM in a single liquid coolant-based system [44][74], one conventional vapor compression refrigeration system can be used to manage all the components of the vehicle. Then, the thermal energy can be easily distributed where required by controlling a system of liquid coolant valves, as we explained previously. An advantage of this technology is that it is possible to switch the system between Air Conditioning (AC) and heat pump modes without inverting the refrigerant flow. To operate properly this kind of thermal management system it is essential to control the compressor speed to maintain the required target liquid coolant temperature in every working mode [75]. The varying configuration of the coolant circuit in different working modes presents a challenge for achieving optimal regulation of the compressor speed using a standard PI controller with fixed proportional and integral coefficients. In order to ensure system stability under all conditions, it becomes necessary to use conservative controller settings, often resulting in slower response times due to the small value assigned to the proportional coefficient. An example of the outcome of such a controller is shown in Figure 5.1. It illustrates a simulation of a vehicle's thermal management system operating in the cooling mode. Initially, only the cabin's temperature is regulated. However, as operations progress, the mode shifts to accommodate the battery's cooling needs, particularly when its temperature exceeds the ideal operating range. This shift places an abrupt additional thermal demand on the evaporator of the vapor compression refrigeration system. The controller, un-

able to instantly adjust the compressor's speed to this sudden demand, causes a temporary rise in the coolant temperature on the evaporator's side. This mainly impacts the HVAC system's dehumidification capability. As a result, passengers may feel a temporary discomfort due to a fluctuation in relative humidity, which can swing by approximately 10%. To address this limitation, we propose a vari-

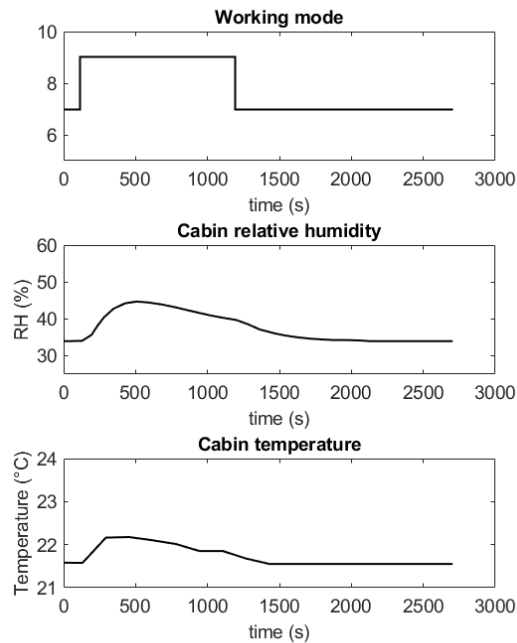


Figure 5.1: Example of a EVTMS shifting from cabin cooling to cabin and battery cooling

able PI controller where the values of the proportional and integral coefficients dynamically adjust in proportion to the output of a predefined function.

By incorporating the variable nature of the coolant circuit configuration into the controller design, the proposed approach aims to enhance the overall performance and responsiveness of the thermal management system. The variable PI controller enables more efficient and effective regulation of the compressor speed, adapting to the changing demands of the system based on the prevailing working mode. This dynamic adjustment of the controller coefficients allows for optimized control, resulting in improved stability and faster response times when compared to a standard PI controller with fixed coefficients.

Through this proposed approach, the thermal management system can achieve better adaptability and performance across different operating conditions. Further analysis and experimentation are conducted to evaluate the

5.2. HEAT PUMP CONTROL SYSTEM

effectiveness and benefits of the variable PI controller, demonstrating its potential for enhanced control accuracy and system efficiency in automotive thermal management applications.

5.2.1 METHODS

The thermal inertia of the liquid coolant loop has an important impact on the tuning of the compressors controller. But, considering that a variation in the volume of coolant moved by the pumps and in the thermal load imposed on the evaporator is observed every time the coolant valves configuration is changed, it becomes challenging to define a single optimal value for a PI controllers coefficients. It was proposed a variable PI controller in which the proportional (K_p) and integral (K_i) gains were defined proportional to the output of the following function:

$$M = \left[\frac{a \frac{1}{n+1} \sum_{i=0}^n |T_{c,out}(t - i \Delta t) - T_{c,in}(t - i \Delta t)| n \Delta t}{1 + |T_{c,out}(t) - T_{c,out}(t - n \Delta t)|} \right]^b \quad (5.1)$$

where a and b are constants, t is the time instant and Δt is an interval of time, $T_{c,in}$ and $T_{c,out}$ represent the measurements of the coolant temperature at the evaporator inlet and outlet, respectively, acquired at the specified time denoted within the parentheses. The numerator of this formula is a quantity proportional to the energy exchanged between the evaporator and the liquid coolant in the interval $n\Delta t$, while the denominator is the gradient of the evaporator outlet temperature in the same time interval, increased by 1. Finally, the proportional and integral gains of the compressors controller are computed every time instant as $K_p = cM$ and $K_i = dM$, where c and d are constants with $c > 10d$. In this way, K_p and K_i increase when there is a higher thermal load on the evaporator, making the response of the controller faster. During a transient condition, the denominator of the function M is greater than or equal to 1, meaning that K_p and K_i decrease as the faster is the variation of the evaporator outlet temperature. Therefore, K_p and K_i assume lower values during a transient condition if the thermal inertia of the liquid coolant loop is smaller. The constants a , b , c , and d were tuned in a first phase in simulation, using Simulink, and in a second phase in the test bench.

5.2.2 SET-UP

The parameter tuning process was conducted using a test layout, as depicted in Figure 1, which was implemented both in the simulation and on the test bench. The layout comprises an automotive vapor compression refrigeration system, consisting of a compressor, an expansion valve, a condenser, and an evaporator. Within this circuit, the refrigerant exchanges heat with two separate liquid coolant circuits: one on the condenser side and another on the evaporator side. The condenser-side coolant circuit includes an expansion tank, a pump, and a radiator to dissipate heat absorbed by the coolant from the condenser. Similarly, the evaporator-side coolant circuit is similar in design, except for the presence of an electric heater instead of a radiator, which serves to simulate a thermal load on the evaporator.

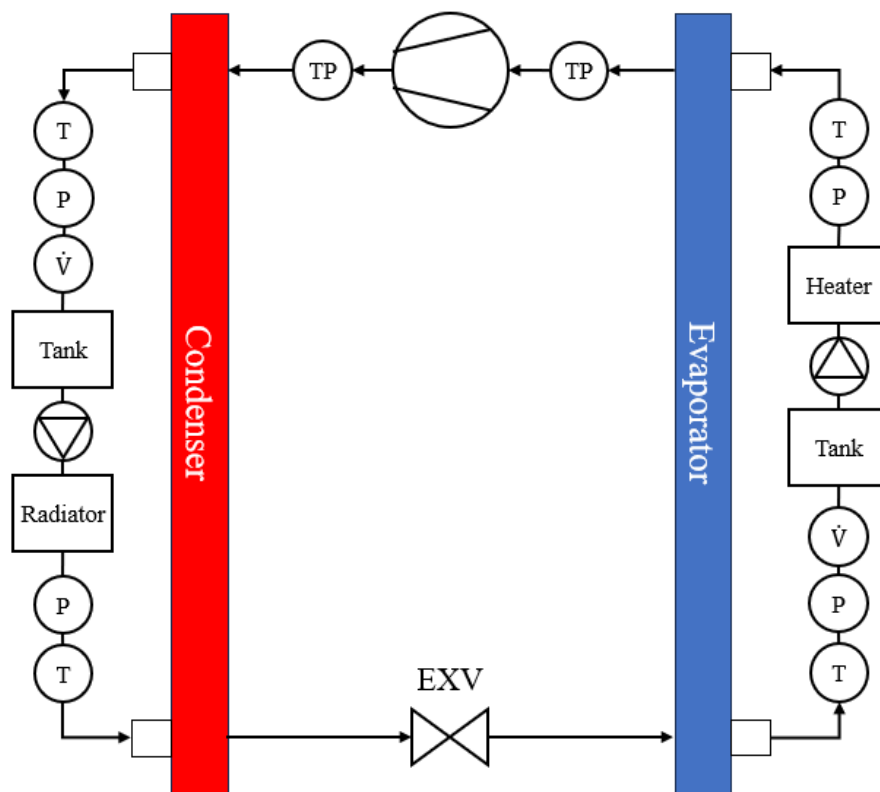


Figure 5.2: Test layout.

To facilitate control and data acquisition, a comprehensive set of sensors was installed within the test bench setup. Temperature and pressure sensors were strategically positioned in the refrigerant circuit, both upstream and down-

5.2. HEAT PUMP CONTROL SYSTEM

stream of the compressor, as well as in the coolant circuits, both upstream and downstream of the condenser and evaporator. Electromagnetic flow meters were installed in both coolant circuits to regulate the pump speeds and maintain a target coolant flow rate of 20 l/min.

To enable the communication between the test bench and the laptop, a CAN/LIN interface known as the Vector VN1670 was employed. This allowed for the acquisition of all measurements via CAN channels, which were then logged in Simulink. The control logic for each component of the test bench was designed within Simulink, which served as the control hub. Control signals were generated within Simulink and sent to the respective devices via LIN channels. Specifically, the control signals encompassed the following:

- Compressor speed to achieve the desired coolant temperature at the evaporator outlet.
- Expansion valve opening steps to achieve the desired superheat.
- Pump speed adjustments to attain the target volumetric flow rates.
- Radiator fan voltage modulation to achieve the desired coolant temperature at the condenser inlet.
- Electric power regulation absorbed by the heater to attain the desired coolant temperature at the evaporator inlet.

During all the tests, on the condenser side, the inlet coolant temperature was kept at 40 °C controlling the speed of the radiator fans, while on the evaporator side, it was maintained at 17 °C regulating the power delivered by an electric heater. To tune the parameters and verify the behavior of the controller, 6 steps were given to the target evaporator outlet temperature, [15 °C, 14 °C, 13 °C, 14 °C, 15 °C, 16 °C]. The results obtained in this test with the variable PI controller were then compared with a standard PI controller in which the coefficients K_p and K_i were constants and were tuned using the Ziegler-Nichols method. As demonstrated in figure 5.3, the outcome of this comparison was that the variable PI controller showed a faster response to the steps while maintaining a similar ability to nullify the error with respect to the target.

In the single liquid coolant-based system it is possible to control the thermal power delivered to each subsystem of the vehicle by regulating the coolant valves opening while maintaining a constant coolant temperature setpoint. Hence, the variable PI controller for the compressor speed was tested to verify its stability in maintaining a constant evaporator outlet target temperature of 15 °C, while steps

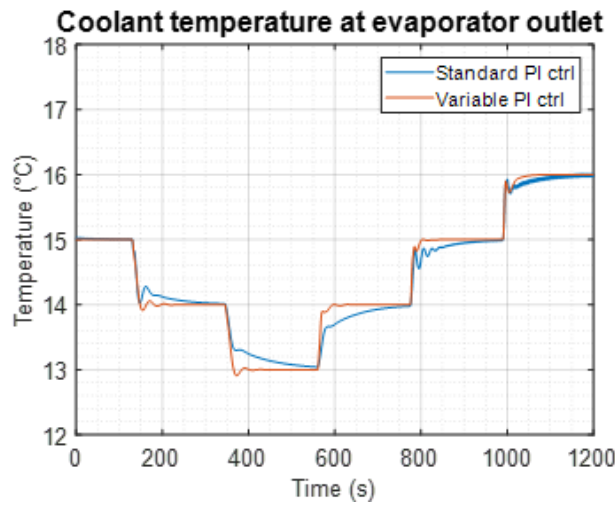


Figure 5.3: Tuning of the controller parameters imposing steps on the target coolant temperature at the evaporator outlet.

were given to the thermal load. The system's behavior was evaluated under two different conditions. In the first condition, a 1 kW step was applied to the thermal load, while in the second condition, a larger 3 kW step was applied. The thermal load imposed on the evaporator was achieved by adjusting the electrical power absorbed by the heater, as depicted in Figure 5.4a and Figure 5.4b. This study is particularly relevant as it allows us to simulate scenarios in which a vehicle's component is connected to the coolant circuit on the evaporator side for cooling purposes, or disconnected once its target temperature has been reached. For instance, we can consider a situation where both the cabin and the battery are initially being cooled, and once the battery reaches its optimal temperature range, a valve closes the pipes connected to the battery. Consequently, the only remaining thermal load on the evaporator would be from the cabin.

5.2.3 RESULTS

Figure 5.4 illustrates the performance comparison between the standard PI controller and the variable PI controller in regulating the compressor speed to maintain a consistent coolant temperature at the evaporator outlet when the system is subjected to positive and negative steps in the thermal load imposed on the evaporator. Specifically, figure 5.4a, figure 5.4c, and figure 5.4e depict the results for the 1 kW step condition, while figure 5.4b, figure 5.4d, and figure 5.4e display the outcomes for the 3 kW step condition.

5.2. HEAT PUMP CONTROL SYSTEM

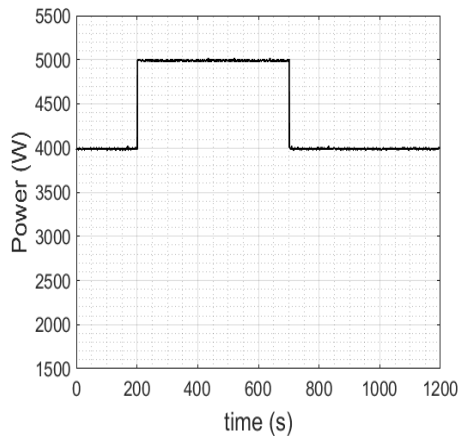
Figure 5.4a and figure 5.4b illustrate the imposed thermal load on the evaporator through the electrical power absorbed by the heater. On the other hand, figure 5.4c and figure 5.4d present the evolution of the coolant temperature at the evaporator outlet over the duration of the test, starting from a steady state condition and experiencing the described excitations for both the 1 kW and 3 kW step conditions. For the 1 kW step condition, the standard PI controller exhibits a maximum absolute error of 0.53 °C compared to the target coolant temperature, whereas the variable PI controller achieves a lower error of 0.34 °C. Similarly, for the 3 kW step condition, the standard PI controller demonstrates a maximum absolute error of 1.50 °C, while the variable PI controller achieves a reduced error of 1.06 °C. Moreover, the variable PI controller showcases notable advantages, such as a shorter time required to minimize the error in relation to the target coolant temperature and a reduced occurrence of overshooting, as compared to the standard PI controller.

In fact, as shown in figure 5.4c, the variable PI controller achieves stabilization of the coolant temperature at 15 °C in approximately 65 seconds, whereas the standard PI controller requires around 150 seconds. Similarly, for figure 5.4d, the variable PI controller achieves stabilization in approximately 120 seconds, whereas the standard PI controller takes approximately 380 seconds for the positive step of the electric power absorbed by the heater and around 290 seconds for the negative step. These results highlight the superior responsiveness of the variable PI controller, enabling a faster response of the compressor to temperature errors, as demonstrated in figure 5.4e and figure 5.4f, where the compressor speed, the output of the controller, is plotted.

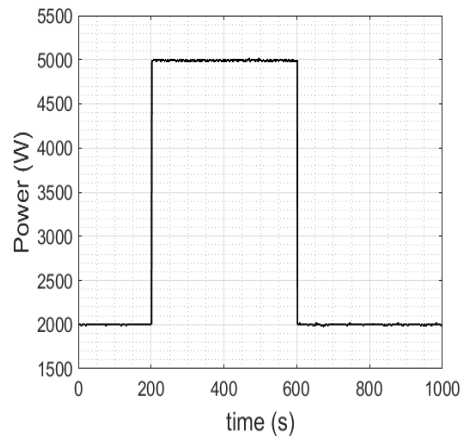
5.2.4 DISCUSSION

To optimize the regulation of the compressor speed and maintain a desired coolant temperature at the evaporator outlet during varying thermal load conditions, a variable PI controller was proposed. These thermal load variations simulated the opening and closing of valves within the liquid coolant circuit, which are responsible for distributing cold or hot coolant to different vehicle subsystems such as the cabin, battery, PEEM, and radiator.

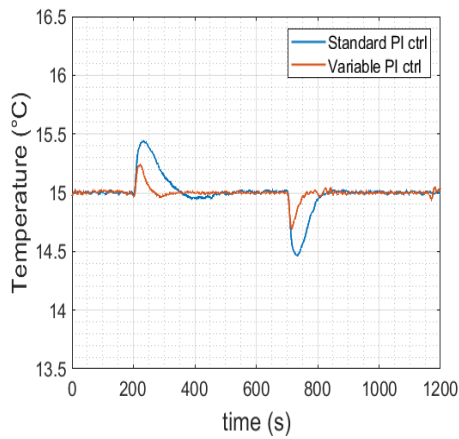
By comparing the performance of the variable PI controller with a standard PI controller, some advantages were observed. The variable PI controller demonstrated superior responsiveness in regulating the compressor speed, resulting



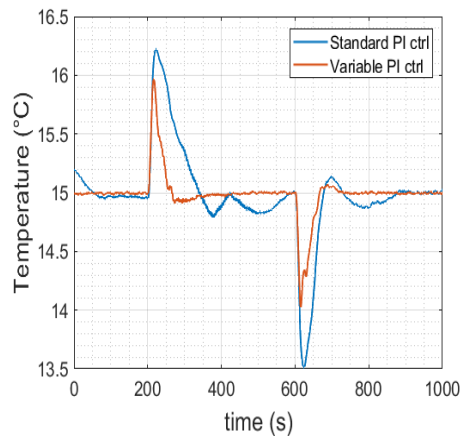
(a) Test 1: Electric power absorbed by the heater.



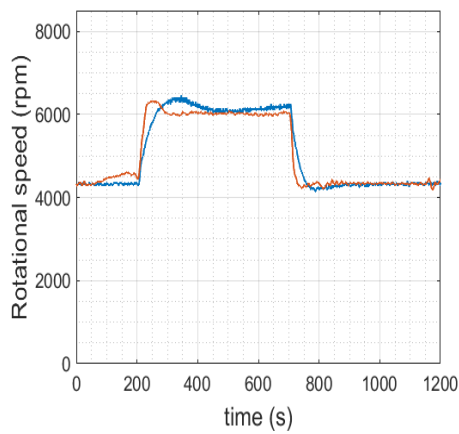
(b) Test 2: Electric power absorbed by the heater.



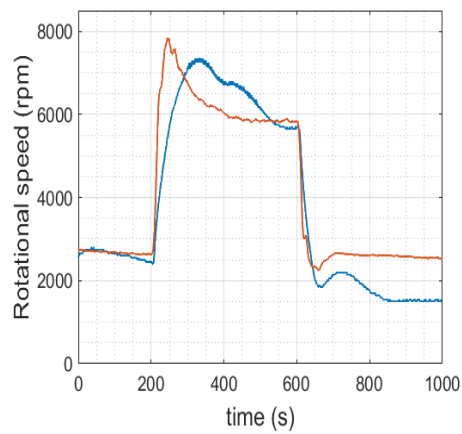
(c) Test 1: Coolant temperature at evaporator outlet.



(d) Test 2: Coolant temperature at evaporator outlet.



(e) Test 1: Compressor speed



(f) Test 2: Compressor speed

Figure 5.4: Performance comparison between the standard PI controller and the variable PI controller.

5.2. HEAT PUMP CONTROL SYSTEM

in a lower maximum absolute error, a shorter time required to minimize the error in relation to the target coolant temperature, and a reduced occurrence of overshooting.

When applied to an integrated thermal management system, particularly in scenarios where the cabin is being cooled and the cooling mode of the battery or the PEEM is activated or deactivated, the variable PI controller offers significant benefits. These benefits contribute to enhanced passenger comfort, as the reduced variation of the coolant temperature leads to a more stable and consistent thermal environment within the vehicle.



Hardware in the Loop system

In pursuit of improved energy efficiency for thermal management systems, the implementation of heat pumps instead of electric heaters, as well as integrating cabin, battery, and PEEM thermal management into a single system to recover waste heat, have emerged as viable solutions (Leighton, 2015 [44]. Ma et al., 2022 [69]. Tian et al., 2018 [70]. Muratori et al., 2022 [74]).

Given the complexity of electric vehicle thermal management systems, it becomes essential to develop accurate mathematical models that describe the physical behavior of these systems for simulation purposes. Such simulations can verify the performance of various layouts and control logics, reducing development costs and time compared to assembling and testing full vehicle prototypes. However, when dealing with systems containing numerous components, dynamic simulations with high accuracy, such as driving scenarios in defined ambient conditions, can be time-consuming. In such cases, HIL simulations offer an advantageous solution, combining simulation models with specific hardware components that exchange data in real-time.

In this chapter, we present the development of a HIL system that integrates the testing of a heat pump on a dedicated test bench with the simulation of the remaining vehicle thermal management system, encompassing models of the cabin, battery pack, and PEEM. This HIL system allows for comprehensive testing of various layouts and control logics for the vehicle's thermal management system without the need to modify the existing test bench setup. Our focus centers on simulating an electric bus operating in a summer condition to verify the HIL system's capability in maintaining consistent temperature, pressure,

6.1. HARDWARE-IN-THE-LOOP SIMULATION

and volume flow at the interfaces between the test bench and the simulation environment. Through this integrated approach, we aim to contribute to the advancement of efficient and reliable thermal management systems for electric vehicles, paving the way towards a sustainable future for transportation.

6.1 HARDWARE-IN-THE-LOOP SIMULATION

The vehicle thermal management system analyzed in this study consists in a refrigerant circuit that exchanges heat through the condenser and the evaporator with a liquid coolant loop. Figure 6.1 illustrates the schematic diagram of this system, referred to as a 'single liquid coolant loop system' because all the vehicle components are thermally managed using a liquid coolant loop. By employing a system of valves within the liquid coolant loop, heat transfer occurs between the hot and cold liquid (represented by the red and blue pipes in Figure 6.1) originating from the condenser and the evaporator, respectively, and the various vehicle devices (see Muratori et al., 2022 [74]).

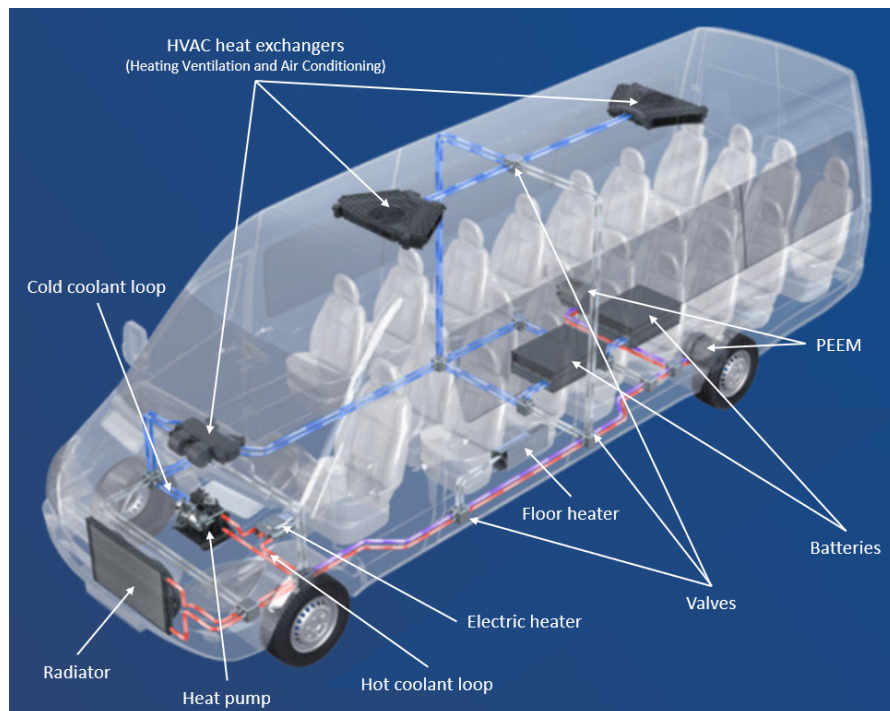


Figure 6.1: Illustration of the vehicle thermal management system

To execute the hardware-in-the-loop simulation, the integrated thermal management system of the vehicle was divided into two parts: the simulated part

and the tested part. The tested part consists of the refrigerant circuit (which can also work as a heat pump), while the simulated part comprises the remainder of the system, including the liquid coolant loop, all associated heat exchangers (excluding the condenser and the evaporator), the cabin, the battery, and the power electronics and electric motor (PEEM). The reason behind this hardware-in-the-loop system design is rooted in the fact that the performance and the control system of the refrigerant circuit (i.e. the compressor's controller and the electronic expansion valve's controller) can be tested on a real heat pump operating as if it would be installed inside a vehicle, but without the need of assembling the entire vehicle thermal management system in the testing area. If we try to study the dynamic behaviour of our vehicle thermal management system using an accurate mathematical model, it is too time-consuming to compute the results relative to a standard driving cycle. Specifically, the solution is computed at a speed approximately ten times slower than real-time. The refrigerant circuit, being a two-phase domain, contributes significantly to reducing the time step and, consequently, the simulation speed. Therefore, a test bench was constructed to test the refrigerant circuit, enabling data exchange with the simulation environment to control the thermal loads imposed on the condenser and the evaporator.

6.1.1 SIMULATION ENVIRONMENT

In the simulation environment we used the same model of the ITMS described in chapter 4. The only difference is that here we removed the heat pump model and substituted it with 4 interfaces (that will be explained in subsection 6.1.3) where we have an exchange of data between the simulation environment and the test bench in which the real heat pump is installed.

Here a summary of the settings used for each component of the model:

- Liquid coolant loop, including pipes, two-way and three-way valves, and T-joints. These elements compute the conservation of mass, momentum, and energy while neglecting fluid inertia and heat dissipation towards the ambient.
- Cabin volume, represented as a 0-D air volume where mass and energy conservation are calculated. To account for passenger presence, sources of heat, humidity, and CO₂ are imposed within the cabin volume.
- Battery pack and PEEM, modelled as thermal masses with heat generation corresponding to the driving cycle.

6.1. HARDWARE-IN-THE-LOOP SIMULATION

- Radiator and heat exchangers responsible for regulating the temperature of the cabin, battery, and PEEM. The effectiveness-NTU method is utilized to compute heat transfer between two fluids within each heat exchanger. During cooling conditions, the condensation of humidity is considered on the air side of the cabin heat exchanger.

The model for each component was calibrated to align with the data provided in the datasheet or experimental test reports from suppliers.

The system functionalities and, consequently, the configuration of coolant valves are defined to meet the requirements of each vehicle subsystem:

- Heating, cooling, ventilation, or dehumidification to maintain the cabin condition within the comfort curve defined in the VDV Nr. 236 standard [67].
- Heating, cooling, or equalization of the battery pack to maintain the temperature within the optimal range (10 °C - 35 °C). Equalization refers to a mode where no cooling or heating is required, but untreated coolant flows through the battery to ensure temperature uniformity.
- Active cooling of the PEEM when any of its components exceed the maximum working temperature (typically around 65 °C) or to utilize the dissipated energy for heating the cabin or battery pack. Otherwise, the PEEM is passively cooled using a radiator.

Finally, we verified that the model is capable of computing solutions at a speed faster than real-time, enabling real-time simulation synchronized with the refrigerant circuit test bench.

6.1.2 TEST BENCH

The experimental setup used for testing the refrigeration circuit is illustrated in Figure 6.2. The refrigeration unit comprises five components: a compressor, a condenser, an expansion valve, an evaporator, and a receiver (not shown in Figure 6.2 as it is integrated into the condenser). Two liquid coolant loops are employed to control the operating conditions of the refrigeration unit, with one connected to the condenser and the other to the evaporator.

Each loop includes a pump that is regulated to maintain a target liquid volume flow rate, measured using an electromagnetic flowmeter. The electromagnetic flowmeter is equipped with a measuring range of 0 - 10 m/s and an accuracy of $0.2\% \pm 1$ mm/s. Upstream of each pump, an expansion tank is positioned to accommodate coolant expansion resulting from temperature and pressure increases. In the coolant loop on the right side of Figure 6.2, a radiator is installed to dissipate heat transferred to the coolant by the condenser.

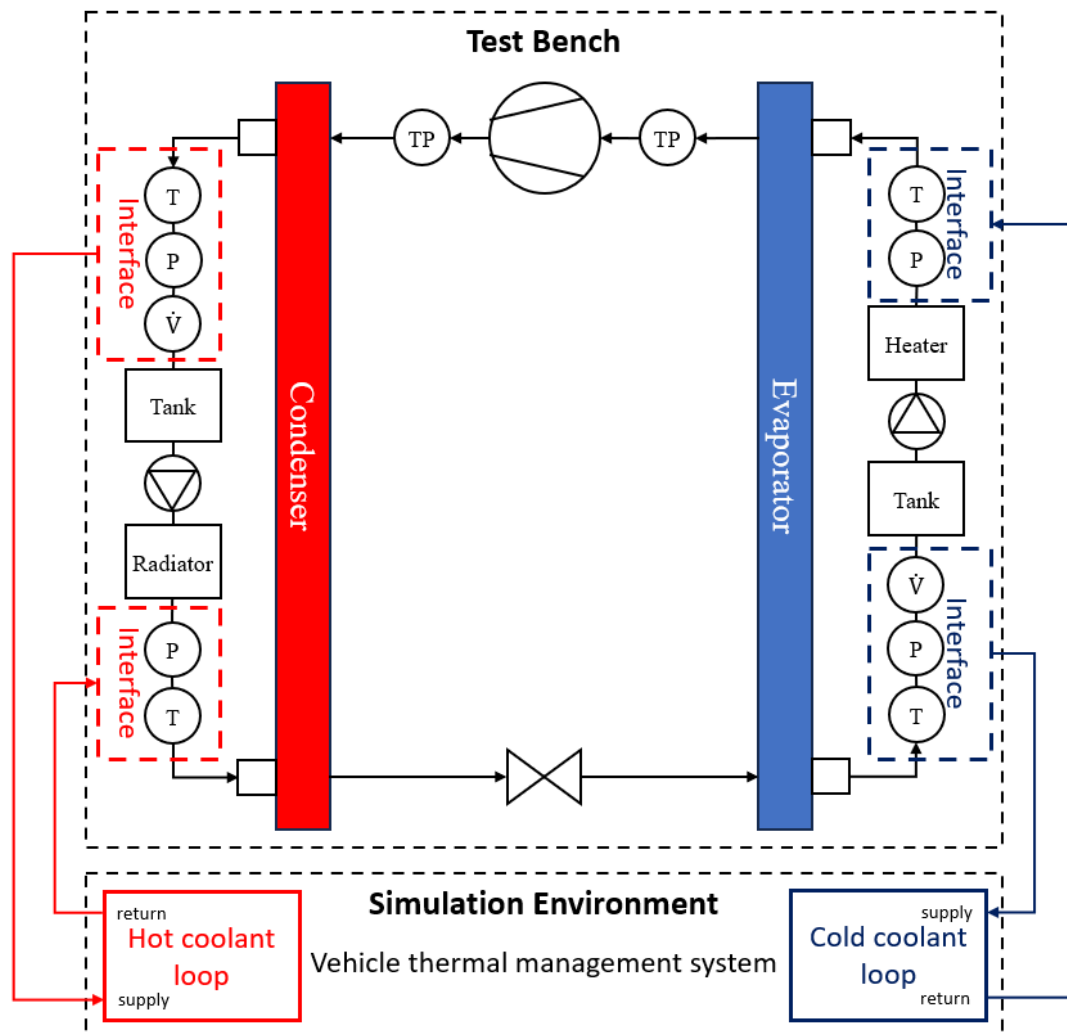


Figure 6.2: Layout of the HIL system. The sensors are identified as T = temperature, P = pressure, V = volume flow rate, TP = temperature and pressure (a single sensor that measures both quantities).

The rotational speed of the condenser fans is controlled using a PI controller for voltage regulation, thereby maintaining a target coolant temperature at the condenser inlet. In the other coolant loop, a high-voltage electric heater is incorporated to compensate for the heat absorbed by the evaporator from the coolant. The power of the electric heater is regulated to achieve a target temperature at the evaporator inlet. The electric heater includes a built-in temperature sensor to measure the liquid temperature within it, enabling automatic control of the absorbed power within a range of 0 W to a maximum value defined by the user, in order to attain the desired coolant temperature. To enhance the regulation of the coolant temperature at the evaporator inlet, the internal controller of the

6.1. HARDWARE-IN-THE-LOOP SIMULATION

heater is not utilized, and instead, an external PI controller is employed. Consequently, a very high target temperature is set for the electric heater to operate at maximum power, while the PI controller regulates the limit to the maximum power to achieve the target coolant temperature measured by a sensor installed at the evaporator inlet. This approach is adopted for two reasons. Firstly, heat is absorbed by the fluid from the external ambient along the pipe connecting the heater to the evaporator, making the temperature measured by the built-in sensor not precisely representative of the evaporator inlet temperature. Secondly, the temperature sensor installed at the evaporator inlet provides higher accuracy. This PT100 sensor measures temperatures in the range of -50 - 450 °C with an accuracy of 0.25 °C. The same type of temperature sensor is utilized at the evaporator outlet and at the condenser inlet and outlet. Pressure sensors are also installed at these four locations, allowing the use of Coolprop (a thermophysical property database developed by Bell et al. [76]) to determine density and specific heat based on both pressure and temperature readings. By combining these measurements with the coolant volume flow rate, the thermal power exchanged in the condenser and evaporator can be assessed using the following equation:

$$W = \rho \dot{V} (c_o T_o - c_i T_i) \quad (6.1)$$

Where:

- W = Heat transfer rate (kW)
- ρ = density of coolant calculated at the heat exchanger outlet as a function of temperature and pressure (kg/m³)
- V = volumetric flow rate of the coolant measured at the heat exchanger outlet (m³/s)
- c_i = specific heat of the coolant at the heat exchanger inlet (kJ/kg K)
- c_o = specific heat of the coolant at the heat exchanger outlet (kJ/kg K)
- T_i = coolant temperature at the evaporator/condenser inlet (K)
- T_o = coolant temperature at the evaporator/condenser outlet (K)

6.1.3 DATA EXCHANGE AND CONTROL LOGIC

The hardware employed to enable data exchange between the simulation environment and the test bench is the Vector VN1670 CAN/LIN interface and

the software that allows the interaction between the Simulink model and the Vector Hardware is CANoe. The simulation running on the laptop establishes communication with the Vector interface via an Ethernet bus. Subsequently, data are exchanged with the test bench, including sensors, data acquisition hardware, ECU (electronic control unit), and controlled devices, through CAN and LIN buses, as depicted in Figure 6.3.

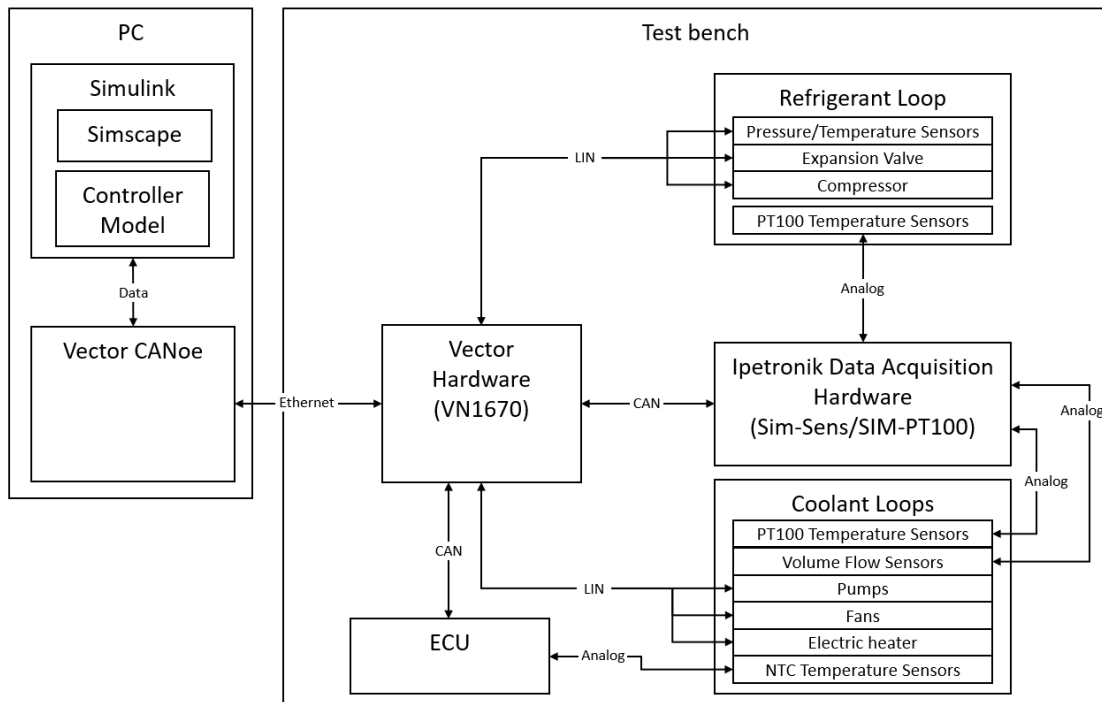


Figure 6.3: Communication scheme of the HIL system

The following data are exchanged between the simulation environment and the test bench:

- Compressor speed.
- Expansion valve opening steps.
- Radiator fans' voltage.
- Electric heater voltage limit and target temperature of the coolant inside it.
- Pump speeds.
- Temperature and pressure measurements in the refrigerant at the compressor inlet and outlet.
- Temperature and pressure measurements in the coolant at the evaporator inlet and outlet.

6.1. HARDWARE-IN-THE-LOOP SIMULATION

- Temperature and pressure measurements in the coolant at the condenser inlet and outlet.
- Coolant volumetric flow rates in the condenser and evaporator.

The interfaces for this system are the temperature, volume flow rate, and pressure of the coolant (as shown in Figure 6.2) at the:

- Condenser inlet
- Condenser outlet
- Evaporator inlet
- Evaporator outlet

The coolant temperature measured in the test bench at the condenser outlet and at the evaporator outlet is the result of the regulation of the compressor speed, through a PI controller. These two values are imposed in the physical model, using a "Controlled Reservoir" block, to the coolant supply of the thermal management system in the hot coolant loop and cold coolant loop respectively. Then, thanks to the CANoe software that synchronizes the computation speed with the data acquisition, the physical model computes in real-time, every 0.1 s, the temperature of the coolant return from the thermal management system in both coolant loops. Consequently, these two values are used in the controller model as set-points for the regulation of the radiator fans speed and of the electrical power absorbed by the heater, respectively. In this way, we can achieve the same temperature values at the condenser inlet and at the evaporator inlet on the test bench.

In the physical model, the volumetric flow rate is controlled in the two coolant loops using a "Controlled Volumetric Flow Rate Source" block positioned immediately after the "Controlled Reservoir" block. The volumetric flow rate is set equal to the measurements acquired in the two liquid coolant circuits of the test bench. To achieve this, the pumps installed in the test bench are controlled using a PI controller, ensuring a constant flow rate of 20 l/min in each loop. The pressure is set as a constant value in the "Controlled reservoir" blocks, where the temperature of the coolant supply and return are also defined. The pressure value is determined based on measurements obtained from the test bench pipes when a coolant flow rate of 20 l/min is maintained. This simplification assumes that the variations of coolant pressure during the test are minimal due to the constant coolant flow. Consequently, when computing the energy flow using equation 6.1, the effects of density and specific heat variations with respect to pressure can be considered negligible [77].

6.2 TEST CONDITIONS

The test was run setting in the physical model the simulation of the same electric bus described in the previous chapter, with 10 passengers onboard, driving in summer climatic conditions, as described in the VDV Nr. 236 standard [67]. The ambient temperature, relative humidity, and solar radiation are set at 35 °C, 50%, and 1000 W/m² respectively, while the target condition to be maintained in the cabin environment is 27 °C with a relative humidity < 50% and a CO₂ concentration < 1100 ppm, which corresponds to the comfort mode defined in the standard. The battery cooling is activated if the temperature of the cells is > 35 °C and then it is switched off, triggering the state of equalization, when the temperature reaches 30 °C. The PEEM in this simulation remains within the allowed working temperatures, therefore the request for active cooling is not triggered. The thermal generations inside the battery pack and PEEM are imposed equal to the quantities declared by the vehicle manufacturer, which are characteristic of a typical driving cycle. The heat generations are 450 W, 727 W, 364 W, 585 W and 850 W respectively for the battery pack, electric motor, inverter, DC/DC converters, and Advanced Driver Assistance System (ADAS). Within the cabin, for each passenger 3 sources are imposed: 70 W of sensible heat, 0.01 g/s of CO₂, and 0.04 g/s of moisture at 30 °C.

The simulation was carried out in a dynamic situation of the thermal management system to better verify the performance of the interface between the test bench and the physical model. In particular, we want to observe if the regulation of the radiator fans and of the electric heater is able to reproduce thermal loads on the condenser and evaporator, respectively, that make the heat pump work as if it was really installed inside the vehicle thermal management system. This point is assessed by checking if the coolant temperatures measured at the two refrigerant-liquid heat exchangers inlet follow closely the values computed for the coolant return temperatures in the physical model.

The simulation began with the vehicle being hot-soaked in the sun and concluded once all the vehicle's subsystems reached their target conditions, and the coolant temperature in both loops stabilized.

6.3 RESULTS

Figures 6.4 and 6.5 display the 6.4 temperature interfaces of the Hardware-in-the-Loop (HIL) system. In Figure 6.4, the dynamic profile of the coolant temperature at the outlet of the condenser and evaporator is depicted. The curves for the values measured on the test bench and those computed by the physical model in the simulation environment are perfectly superimposed. This agreement is expected since the simulation imposes identical coolant supply line temperatures as those acquired from the test bench. Figure 6.5 shows the same curves for the interfaces at the inlet of the condenser and evaporator. This plot demonstrates the effective performance of the controller model in regulating the heat exchanged through the radiator and electric heater to achieve consistent temperatures at the inlet of the condenser and evaporator in both the test bench and simulation environment. The controller model performs well throughout the entire test duration.

As the battery temperature reaches 30 °C (Figure 6.6), and the battery thermal management subsystem shifts from cooling to equalization mode, the controller faces a sudden variation in the thermal load imposed on the evaporator and condenser, as represented in Figure 6.7. In this scenario, the temperature profiles (Figure 6.5) measured in the test bench closely follow the simulated profiles. The electric heater exhibits slightly better responsiveness compared to the radiator, with a maximum error of approximately 0.9 °C at the condenser inlet and about 0.5 °C at the evaporator inlet.

Figure 6.5 and Figure 6.7 also reveal two limitations of the test bench in terms of hardware. Initially, during the test's early stages, the measured coolant temperature is lower than the simulated one. Investigation reveals that the electric heater saturates during this phase (Figure 6.8), meaning it is not powerful enough to replicate the thermal load calculated in the simulation. Additionally, toward the end of the test, after the battery enters equalization mode, the temperature measured at the condenser inlet oscillates around the target with an amplitude of about 0.7 °C. This behaviour results from the radiator expelling excessive heat from the coolant when the fans are operating at minimum speed. The controller frequently switches the fan voltage supply between 0 V and the minimum value of 2.4 V to maintain the target coolant temperature (Figure 6.9).

Although the volume flow rate and pressure interfaces are not plotted, it is

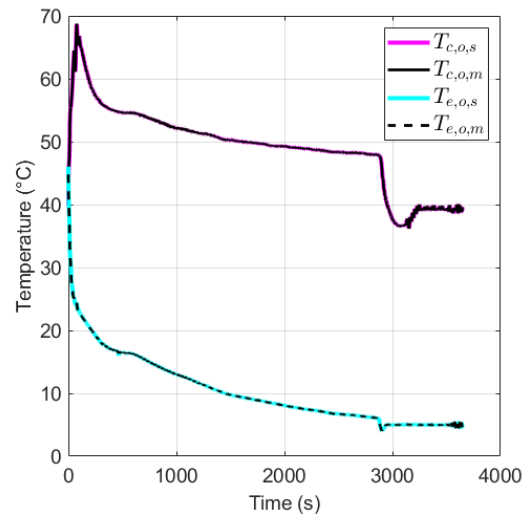


Figure 6.4: Interface between the test bench and the simulation environment at the outlet of the condenser and evaporator. $T_{c,o,s}$ and $T_{c,o,m}$ are respectively the coolant temperature at the condenser outlet computed in the simulation environment and measured on the test bench. $T_{e,o,s}$ and $T_{e,o,m}$ are respectively the coolant temperature at the evaporator outlet computed in the simulation environment and measured on the test bench.

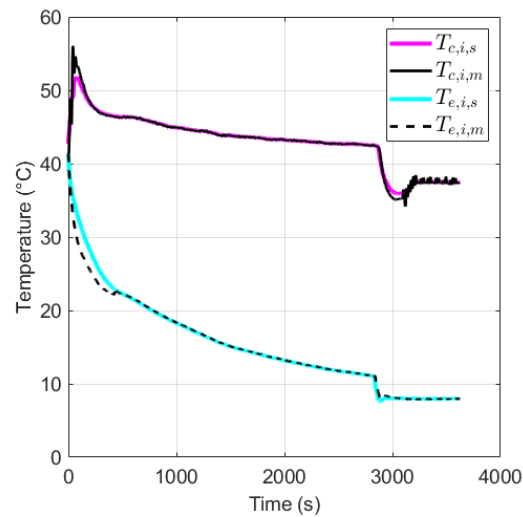


Figure 6.5: Interface between the test bench and the simulation environment at the inlet of the condenser and evaporator. $T_{c,i,s}$ and $T_{c,i,m}$ are respectively the coolant temperature at the condenser inlet computed in the simulation environment and measured on the test bench. $T_{e,i,s}$ and $T_{e,i,m}$ are respectively the coolant temperature at the evaporator inlet computed in the simulation environment and measured on the test bench.

6.3. RESULTS

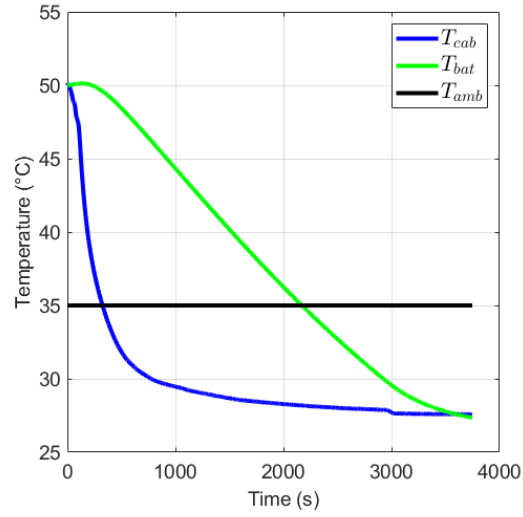


Figure 6.6: Evolution during the test of the cabin temperature (T_{cab}) and battery temperature (T_{bat}). T_{amb} represents the ambient temperature considered in the simulation environment.

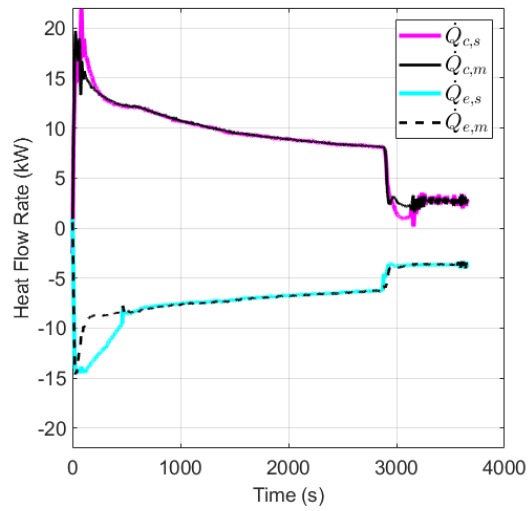


Figure 6.7: Comparison between the thermal power exchanged computed in the simulation environment and measured on the test bench through the condenser ($W_{c,s}$ and $W_{c,m}$) and the evaporator ($W_{e,s}$ and $W_{e,m}$).

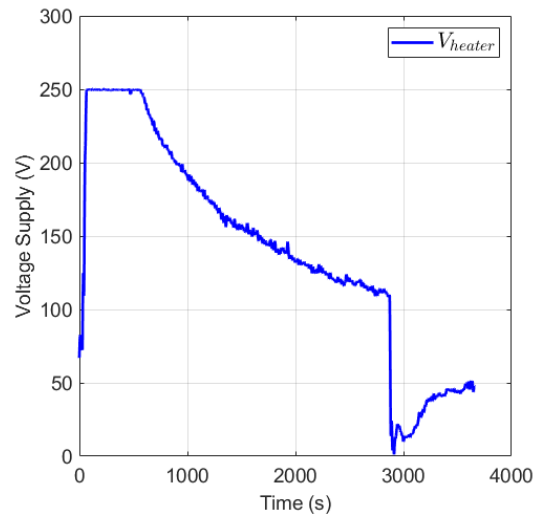


Figure 6.8: Regulation of the electric heater to maintain the target coolant temperature at the evaporator inlet on the test bench.

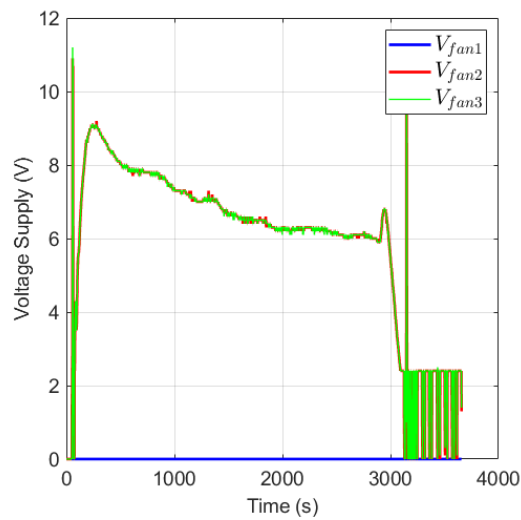


Figure 6.9: Regulation of the radiator fans to maintain the target coolant temperature at the condenser inlet on the test bench.

6.4. DISCUSSION

important to note that the volume flow rate is directly imposed in the simulation environment, matching the measured one at each time step. On the other hand, the pressure value is defined in the simulation as a constant, which is not updated during the test. While this value is close to the pressure measured in the test bench, it may not be exactly the same. Nevertheless, Figure 6.7 validates the hypothesis that the heat transfer at the heat exchangers is negligibly affected by small variations in pressure. The curves for the thermal power exchanged, computed in the simulation, align well with those obtained from measurements in the test bench when the simulated and measured coolant temperatures match.

Finally, Figure 6.6 showcases the performance of the heat pump in cooling down the cabin and battery pack when the ambient temperature is 35 °C, and the vehicle is exposed to significant solar radiation. Notably, the large thermal capacity of the bus battery pack is evident, as it takes nearly an hour to cool it down from 50 °C to 30 °C. Therefore, it is advisable to continually monitor the battery temperature and activate the cooling or heating mode even when the vehicle is parked, if the temperature falls outside the optimal working range.

6.4 DISCUSSION

The thermal management system for battery electric vehicles presents greater complexity compared to traditional internal combustion engine vehicles due to the need to manage more components. As a result, simulation tools are increasingly adopted to streamline development processes and reduce costs. In this chapter, we presented a Hardware-in-the-Loop (HIL) system that enables us to thoroughly test the performance and control logic of a real heat pump as if it were integrated into the thermal management system of an electric bus.

In our HIL system, the heat pump is connected to a radiator and an electric heater, while the vehicle cabin, battery pack, power electronics and electric motor (PEEM), and the overall vehicle thermal management system are modelled in Simscape. This comprehensive thermal management system encompasses two liquid coolant loops: a hot loop, heated by the condenser, and a cold loop, cooled by the evaporator. These loops distribute cold and hot coolant to the relevant heat exchangers through a system of valves.

We established interfaces before and after the condenser and evaporator on the liquid side, allowing us to exchange temperature, pressure, and volumetric flow rate data in real time between the HIL test bench and the simulation envi-

ronment. A controller model effectively utilizes this data to regulate the thermal power exchanged through the radiator and heater, accurately reproducing the computed thermal load in the simulation for both coolant loops.

Our results demonstrate the overall efficacy of the controller model, indicating that it can effectively manage the thermal load. However, we also identified two limitations in terms of hardware for our HIL system. Firstly, the electric heater's power proved insufficient during certain phases of the test, suggesting the need for a more powerful alternative. Secondly, the radiator exhibited some limitations during the final phases of the test, with temperature oscillations occurring around the target temperature, implying the requirement for a smaller version of the radiator.

In conclusion, by addressing the identified hardware limitations, future iterations of the system could lead to more efficient and accurate testing, aiding in the advancement of thermal management systems for electric vehicles. The integration of HIL testing with advanced simulation models offers an effective and cost-efficient approach for ensuring the robustness and performance of such systems in the transition to a sustainable future of transportation.



Conclusions

Given the scope of information and analysis presented, it's imperative to acknowledge the multi-faceted aspects of managing thermal loads in electric vehicles, especially when considering the holistic approach of the Electric Thermal Management (e.TM) system. The fusion of individual thermal regulation systems into an integrated mechanism significantly enhances the efficiency and operational performance of the vehicle, ensuring a balanced coexistence between passenger comfort and the thermal needs of critical vehicular subsystems like the battery and PEEM.

The innovative approach of e.TM embodies a shift from traditional frameworks by leveraging the synergies between different thermal demands, thereby reducing the overall energy consumption, and facilitating an optimized thermal regulation. Key functionalities like passenger compartment HVAC, battery thermal management, and thermal control of PEEM and ECUs highlight the comprehensive nature of the e.TM system, presenting a progressive path towards better energy management in electric vehicles.

One of the pivotal observations from this study revolves around the impact of air recirculation within the cabin, especially concerning the CO₂ concentration levels. The implementation of a control strategy aimed at reducing HVAC system energy consumption, while maintaining a safe cabin CO₂ concentration, underlines a nuanced approach towards ensuring both energy efficiency and the well-being of the occupants. The examination of CO₂ sensor placements within the cabin further elucidates the critical nature of accurate monitoring and control in achieving the desired objectives of the air recirculation strategy. Results

suggested placing sensors near the driver's head level and away from vents for accurate readings. The study also presented a methodology to determine the quantity of CO₂ sensors required for attaining the desired level of measurement precision within the cabin.

The development and simulation of different layouts for the secondary loop, specifically focusing on the PEEM's positioning and its implications on waste heat recovery, provide valuable insights into optimizing the thermal management system. Two layouts for the secondary loop were investigated. In the first layout, the PEEM was positioned parallel to the heat pump condenser along the hot coolant circuit. In the second layout, it was connected in series to the radiator. The study simulated the heating mode of an e.TM system under three different environmental conditions (0 °C, 5 °C, and 10 °C) and tested its performance in terms of electric energy consumption and time needed to heat the battery and cabin to 10 °C and 20 °C, respectively. Results indicated that in layout 1, heat recovery from the PEEM was not feasible during driving cycles due to the hot coolant circuit's temperature being higher than that of the PEEM subsystems. Conversely, layout 2 allowed for heat recovery from the PEEM, particularly evident at 0°C. Implementing layout 2 led to improved system performance, resulting in reduced electric energy consumption and heating time to reach target temperatures for both the cabin and battery. The comparative analysis between different environmental conditions and the consequent performance of the e.TM system accentuates the significance of adaptive and flexible thermal management strategies.

The introduction of an Intelligent Valve system, orchestrated through various working modes based on the operational state of the vehicle, marks a noteworthy advancement in managing the coolant loop configuration dynamically. The variable PI controller, proposed for optimizing the regulation of compressor speed, demonstrates heightened responsiveness and accuracy in managing the coolant temperature, contributing to enhanced passenger comfort and efficient thermal management. The controller was developed considering the variable configuration of the coolant circuit. When compared to a standard PI controller, our design exhibited a reaction speed 2 to 3 times faster.

In this thesis we introduced a HIL system designed to comprehensively evaluate the performance and control logic of a real heat pump within the thermal management system of an electric bus. This HIL system integrates the heat pump with a radiator and an electric heater, while simulating other compo-

nents such as the vehicle cabin, battery pack, power electronics and electric motor (PEEM), and the overall vehicle thermal management system using Simscape. Interfaces before and after the condenser and evaporator allow real-time exchange of temperature, pressure, and flow rate data between the HIL test bench and the simulation environment. A controller model utilizes this data to regulate thermal power exchanged through the radiator and heater, accurately reproducing computed thermal loads in the simulation for both coolant loops. Results demonstrate the controller model's effectiveness in managing thermal loads, with temperature differences between the test bench and simulation environment consistently below 1°C at the interfaces. Combining HIL testing with advanced simulation models provides a cost-effective and efficient method for analyzing and enhancing the control logic of thermal management systems, facilitating the transition towards a sustainable future in transportation.

The future endeavors encompassing the investigation of CO₂ sensor accuracy and exploring cost-effective sensor solutions underscore an ongoing commitment towards evolving the e.TM system. The exploration into reducing costs while retaining or even enhancing the measurement accuracy could potentially pave the way for more affordable and efficient thermal management solutions.

In wrapping up, the comprehensive analysis presented herein not only highlights the complex nature of thermal management in electric vehicles but also underscores the potential for innovative solutions like the e.TM system. As the automotive industry continues to evolve towards more sustainable and electric solutions, the findings and methodologies discussed in this thesis contribute to a growing body of knowledge that is paramount for the development of efficient, comfortable, and safe electric vehicles.

References

- [1] Jacqueline S. Edge et al. "Lithium ion battery degradation: what you need to know". In: *Phys. Chem. Chem. Phys.* 23 (14 2021), pp. 8200–8221. DOI: 10.1039/D1CP00359C.
- [2] Jong Tae Lee et al. "Effect of Air-Conditioning on Driving Range of Electric Vehicle for Various Driving Modes". In: *Asia Pacific Automotive Engineering Conference*. SAE International, Mar. 2013. DOI: <https://doi.org/10.4271/2013-01-0040>. URL: <https://doi.org/10.4271/2013-01-0040>.
- [3] Ludovic Horrein et al. "Impact of Heating System on the Range of an Electric Vehicle". In: *IEEE Transactions on Vehicular Technology* 66.6 (2017), pp. 4668–4677. DOI: 10.1109/TVT.2016.2615095.
- [4] R Farrington and J Rugh. "Impact of Vehicle Air-Conditioning on Fuel Economy, Tailpipe Emissions, and Electric Vehicle Range". In: *Earth Technologies Forum*. Washington, D.C., Oct. 2000.
- [5] Bozhi Yang et al. "Impact of Thermal Architecture on Electric Vehicle Energy Consumption/Range: A Study with Full Vehicle Simulation". In: *SAE WCX Digital Summit*. SAE International, Apr. 2021. DOI: <https://doi.org/10.4271/2021-01-0207>.
- [6] Kunfeng Liang et al. "Advances and challenges of integrated thermal management technologies for pure electric vehicles". In: *Sustainable Energy Technologies and Assessments* 46 (2021), p. 101319. ISSN: 2213-1388. DOI: <https://doi.org/10.1016/j.seta.2021.101319>.
- [7] Shuai Ma et al. "Temperature effect and thermal impact in lithium-ion batteries: A review". In: *Progress in Natural Science: Materials International* 28.6 (2018), pp. 653–666. ISSN: 1002-0071. DOI: <https://doi.org/10.1016/j.pnsc.2018.11.002>.

REFERENCES

- [8] Jiedong Ye, Abdallah Yousef Mohammad Aldaher, and Gangfeng Tan. "Thermal performance analysis of 18,650 battery thermal management system integrated with liquid-cooling and air-cooling". In: *Journal of Energy Storage* 72 (2023), p. 108766. ISSN: 2352-152X. DOI: <https://doi.org/10.1016/j.est.2023.108766>.
- [9] *Self-regulating heater*. https://en.wikipedia.org/wiki/Self-regulating_heater. Accessed: 22-Oct-2023.
- [10] Sourav Chowdhury et al. "Total Thermal Management of Battery Electric Vehicles (BEVs)". In: *CO₂ Reduction for Transportation Systems Conference*. SAE International, May 2018. DOI: <https://doi.org/10.4271/2018-37-0026>.
- [11] Kang Li et al. "Investigation on the performance and characteristics of a heat pump system for electric vehicles under extreme temperature conditions". In: *Case Studies in Thermal Engineering* 27 (2021), p. 101308. ISSN: 2214-157X. DOI: <https://doi.org/10.1016/j.csite.2021.101308>.
- [12] Binbin Yu et al. "Energy consumption and increased EV range evaluation through heat pump scenarios and low GWP refrigerants in the new test procedure WLTP". In: *International Journal of Refrigeration* 100 (2019), pp. 284–294. ISSN: 0140-7007. DOI: <https://doi.org/10.1016/j.ijrefrig.2019.01.033>. URL: <https://www.sciencedirect.com/science/article/pii/S0140700719300490>.
- [13] Hai-Jiao Yin et al. "Experimental research on a novel cold storage defrost method based on air bypass circulation and electric heater". In: *Energy* 37.1 (2012). 7th Biennial International Workshop Advances in Energy Studies, pp. 623–631. ISSN: 0360-5442. DOI: <https://doi.org/10.1016/j.energy.2011.10.040>.
- [14] Pradeep Bansal, David Fothergill, and Ryan Fernandes. "Thermal analysis of the defrost cycle in a domestic freezer". In: *International Journal of Refrigeration* 33.3 (2010), pp. 589–599. ISSN: 0140-7007. DOI: <https://doi.org/10.1016/j.ijrefrig.2009.11.012>.
- [15] Alois Steiner and René Rieberer. "Simulation based identification of the ideal defrost start time for a heat pump system for electric vehicles". In: *International Journal of Refrigeration* 57 (2015), pp. 87–93. ISSN: 0140-7007. DOI: <https://doi.org/10.1016/j.ijrefrig.2015.04.018>.

- [16] Seong Ho Hong et al. "Performance improvement of heat pumps using novel microchannel heat exchangers with plain-louver fins during periodic frosting and defrosting cycles in electric vehicles". In: *Energy Conversion and Management* 223 (2020), p. 113306. ISSN: 0196-8904. DOI: <https://doi.org/10.1016/j.enconman.2020.113306>.
- [17] Wei Chen et al. "Design and optimization of dual-cycled cooling structure for fully-enclosed permanent magnet motor". In: *Applied Thermal Engineering* 152 (2019), pp. 338–349. ISSN: 1359-4311. DOI: <https://doi.org/10.1016/j.applthermaleng.2019.02.070>.
- [18] Kang Li et al. "Investigation on reverse cycle defrosting strategy of an outdoor heat exchanger in air conditioning heat pump system for electric vehicles". In: *Case Studies in Thermal Engineering* 27 (2021), p. 101281. ISSN: 2214-157X. DOI: <https://doi.org/10.1016/j.csite.2021.101281>.
- [19] Anci Wang et al. "Research on efficient defrosting control logic for transcritical CO₂ electric vehicle heat pump air-conditioning system". In: *International Journal of Refrigeration* 138 (2022), pp. 13–22. ISSN: 0140-7007. DOI: <https://doi.org/10.1016/j.ijrefrig.2022.03.028>.
- [20] Kang Li et al. "An experimental investigation on the frosting and defrosting process of an outdoor heat exchanger in an air conditioning heat pump system for electric vehicles". In: *Applied Thermal Engineering* 201 (2022), p. 117766. ISSN: 1359-4311. DOI: <https://doi.org/10.1016/j.applthermaleng.2021.117766>.
- [21] Huiming Zou et al. "Experimental Study on Heating Performance of an R1234yf Heat Pump System for Electric Cars". In: *Energy Procedia* 142 (2017). Proceedings of the 9th International Conference on Applied Energy, pp. 1015–1021. ISSN: 1876-6102. DOI: <https://doi.org/10.1016/j.egypro.2017.12.348>.
- [22] Anci Wang et al. "Pseudo-optimal discharge pressure analysis of transcritical CO₂ electric vehicle heat pumps due to temperature glide". In: *Applied Thermal Engineering* 215 (2022), p. 118856. ISSN: 1359-4311. DOI: <https://doi.org/10.1016/j.applthermaleng.2022.118856>.
- [23] B.V. Ratnakumar, M.C. Smart, and S. Surampudi. "Effects of SEI on the kinetics of lithium intercalation". In: *Journal of Power Sources* 97-98 (2001). Proceedings of the 10th International Meeting on Lithium Batteries, pp. 137–

REFERENCES

139. ISSN: 0378-7753. DOI: [https://doi.org/10.1016/S0378-7753\(01\)00682-6](https://doi.org/10.1016/S0378-7753(01)00682-6).
- [24] S.S. Zhang, K. Xu, and T.R. Jow. "The low temperature performance of Li-ion batteries". In: *Journal of Power Sources* 115.1 (2003), pp. 137–140. ISSN: 0378-7753. DOI: [https://doi.org/10.1016/S0378-7753\(02\)00618-3](https://doi.org/10.1016/S0378-7753(02)00618-3).
- [25] Sachin Bhide and Taehyun Shim. "Development of improved Li-ion battery model incorporating thermal and rate factor effects". In: *2009 IEEE Vehicle Power and Propulsion Conference*. 2009, pp. 544–550. DOI: [10.1109/VPPC.2009.5289800](https://doi.org/10.1109/VPPC.2009.5289800).
- [26] Ahmad A. Pesaran. "Battery thermal models for hybrid vehicle simulations". In: *Journal of Power Sources* 110.2 (2002), pp. 377–382. ISSN: 0378-7753. DOI: [https://doi.org/10.1016/S0378-7753\(02\)00200-8](https://doi.org/10.1016/S0378-7753(02)00200-8).
- [27] Zhonghao Rao et al. "Experimental investigation on thermal management of electric vehicle battery with heat pipe". In: *Energy Conversion and Management* 65 (2013). Global Conference on Renewable energy and Energy Efficiency for Desert Regions 2011 GCREEDER 2011, pp. 92–97. ISSN: 0196-8904. DOI: <https://doi.org/10.1016/j.enconman.2012.08.014>.
- [28] Jaewan Kim, Jinwoo Oh, and Hoseong Lee. "Review on battery thermal management system for electric vehicles". In: *Applied Thermal Engineering* 149 (2019), pp. 192–212. ISSN: 1359-4311. DOI: <https://doi.org/10.1016/j.applthermaleng.2018.12.020>.
- [29] Maria Sarmiento-Carnevali, Ashley Fly, and Pascal Piecha. "Electric Vehicle Cold Start Range Estimation through Battery-in-Loop Simulations within a Virtual Driving Environment". In: *WCX SAE World Congress Experience*. SAE International, Apr. 2020. DOI: <https://doi.org/10.4271/2020-01-0453>.
- [30] Yutian Wang, Haoyu Li, and Decheng Ren. "Characteristics of BLDC motor drive system at high temperature". In: *2016 IEEE 8th International Power Electronics and Motion Control Conference (IPEMC-ECCE Asia)*. 2016, pp. 856–862. DOI: [10.1109/IPEMC.2016.7512398](https://doi.org/10.1109/IPEMC.2016.7512398).
- [31] Antti Lajunen, YinYe Yang, and Ali Emadi. "Recent Developments in Thermal Management of Electrified Powertrains". In: *IEEE Transactions on Vehicular Technology* 67.12 (2018), pp. 11486–11499. DOI: [10.1109/TVT.2018.2876315](https://doi.org/10.1109/TVT.2018.2876315).

- [32] Pedram Asef, Ramon B. Perpina, and M.R. Barzegaran. “An innovative natural air-cooling system technique for temperature-rise suppression on the permanent magnet synchronous machines”. In: *Electric Power Systems Research* 154 (2018), pp. 174–181. ISSN: 0378-7796. DOI: <https://doi.org/10.1016/j.epsr.2017.07.031>.
- [33] Seounghwan Hyeon, Chiwon Kim, and Kwan-Soo Lee. “Thermal enhancement of an air-cooled motor with a flow guide”. In: *International Journal of Heat and Mass Transfer* 183 (2022), p. 122228. ISSN: 0017-9310. DOI: <https://doi.org/10.1016/j.ijheatmasstransfer.2021.122228>.
- [34] Stefan Ulbrich, Jeanette Kopte, and Jens Proske. “Cooling Fin Optimization on a TEFC Electrical Machine Housing Using a 2-D Conjugate Heat Transfer Model”. In: *IEEE Transactions on Industrial Electronics* 65.2 (2018), pp. 1711–1718. DOI: [10.1109/TIE.2017.2748051](https://doi.org/10.1109/TIE.2017.2748051).
- [35] Chiwon Kim, Kwan-Soo Lee, and Se-Jin Yook. “Effect of air-gap fans on cooling of windings in a large-capacity, high-speed induction motor”. In: *Applied Thermal Engineering* 100 (2016), pp. 658–667. ISSN: 1359-4311. DOI: <https://doi.org/10.1016/j.applthermaleng.2016.02.077>.
- [36] Ge Baojun, Zhang Jiong, and Dajun Tao. “Temperature prediction and cooling structure optimization of explosion-proof high pressure water-cooled double speed motor”. In: *Energy Reports* 8 (2022), pp. 3891–3901. ISSN: 2352-4847. DOI: <https://doi.org/10.1016/j.egyr.2022.02.281>.
- [37] Changbo Guo et al. “Electromagnetic-thermal coupling analysis of a permanent-magnet in-wheel motor with cooling channels in the deepened stator slots”. In: *Case Studies in Thermal Engineering* 35 (2022), p. 102158. ISSN: 2214-157X. DOI: <https://doi.org/10.1016/j.csite.2022.102158>. URL: <https://www.sciencedirect.com/science/article/pii/S2214157X2200404X>.
- [38] Amitav Tikadar et al. “Comparison of electro-thermal performance of advanced cooling techniques for electric vehicle motors”. In: *Applied Thermal Engineering* 183 (2021), p. 116182. ISSN: 1359-4311. DOI: <https://doi.org/10.1016/j.applthermaleng.2020.116182>.
- [39] Tanguy Davin et al. “Experimental study of oil cooling systems for electric motors”. In: *Applied Thermal Engineering* 75 (2015), pp. 1–13. ISSN: 1359-4311. DOI: <https://doi.org/10.1016/j.applthermaleng.2014.10.060>.

REFERENCES

- [40] Dong Hyun Lim and Sung Chul Kim. "Thermal performance of oil spray cooling system for in-wheel motor in electric vehicles". In: *Applied Thermal Engineering* 63.2 (2014), pp. 577–587. ISSN: 1359-4311. DOI: <https://doi.org/10.1016/j.applthermaleng.2013.11.057>.
- [41] Arslan Saleem et al. "Optimization of oil flow distribution inside the in-wheel motor assembly of electric vehicles for improved thermal performance". In: *Applied Thermal Engineering* 201 (2022), p. 117753. ISSN: 1359-4311. DOI: <https://doi.org/10.1016/j.applthermaleng.2021.117753>.
- [42] Shang Shi et al. "Non-steady experimental investigation on an integrated thermal management system for power battery with phase change materials". In: *Energy Conversion and Management* 138 (2017), pp. 84–96. ISSN: 0196-8904. DOI: <https://doi.org/10.1016/j.enconman.2017.01.069>.
- [43] Michael Schmitt and Mounir Nasri. "Thermal management concept for next generation vehicles". In: *2015 Tenth International Conference on Ecological Vehicles and Renewable Energies (EVER)*. IEEE. 2015, pp. 1–8.
- [44] Daniel Leighton. "Combined Fluid Loop Thermal Management for Electric Drive Vehicle Range Improvement". In: *SAE International Journal of Passenger Cars - Mechanical Systems* 8.2 (Apr. 2015), pp. 711–720. ISSN: 1946-3995. DOI: <https://doi.org/10.4271/2015-01-1709>.
- [45] Gene Titov et al. "MATLAB/Simulink Framework for Modeling Complex Coolant Flow Configurations of Advanced Automotive Thermal Management Systems". In: *SAE 2016 World Congress and Exhibition*. SAE International, Apr. 2016. DOI: <https://doi.org/10.4271/2016-01-0230>.
- [46] Chengguo Li et al. "Reducing Mobile Air Conditioner (MAC) Power Consumption Using Active Cabin-Air-Recirculation in A Plug-In Hybrid Electric Vehicle (PHEV)". In: *World Electric Vehicle Journal* 9.4 (2018). ISSN: 2032-6653. DOI: [10.3390/wevj9040051](https://doi.org/10.3390/wevj9040051). URL: <https://www.mdpi.com/2032-6653/9/4/51>.
- [47] URL: <https://www.epa.gov/vehicle-and-fuel-emissions-testing/dynamometer-drive-schedules>.
- [48] Jonathan L. Scott, David G. Kraemer, and Randal J. Keller. "Occupational hazards of carbon dioxide exposure". In: *Journal of Chemical Health & Safety* 16.2 (2009), pp. 18–22. DOI: [10.1016/j.jchas.2008.06.003](https://doi.org/10.1016/j.jchas.2008.06.003). URL: <https://doi.org/10.1016/j.jchas.2008.06.003>.

- [49] Katarzyna Gladyszewska-Fiedoruk. "Concentrations of carbon dioxide in a car". In: *Transportation Research Part D: Transport and Environment* 16.2 (2011), pp. 166–171. ISSN: 1361-9209. DOI: <https://doi.org/10.1016/j.trd.2010.07.003>. URL: <https://www.sciencedirect.com/science/article/pii/S1361920910001021>.
- [50] Chun-Fu Chiu, Ming-Hung Chen, and Feng-Hsiang Chang. "Carbon Dioxide Concentrations and Temperatures within Tour Buses under Real-Time Traffic Conditions". In: *PLOS ONE* 10.4 (Apr. 2015), pp. 1–12. DOI: [10.1371/journal.pone.0125117](https://doi.org/10.1371/journal.pone.0125117). URL: <https://doi.org/10.1371/journal.pone.0125117>.
- [51] Eon S. Lee and Yifang Zhu. "Application of a High-Efficiency Cabin Air Filter for Simultaneous Mitigation of Ultrafine Particle and Carbon Dioxide Exposures Inside Passenger Vehicles". In: *Environmental Science & Technology* 48.4 (2014). PMID: 24471775, pp. 2328–2335. DOI: [10.1021/es404952q](https://doi.org/10.1021/es404952q). eprint: <https://doi.org/10.1021/es404952q>. URL: <https://doi.org/10.1021/es404952q>.
- [52] Yifang Zhu et al. "In-Cabin Commuter Exposure to Ultrafine Particles on Los Angeles Freeways". In: *Environmental Science & Technology* 41.7 (2007). PMID: 17438754, pp. 2138–2145. DOI: [10.1021/es0618797](https://doi.org/10.1021/es0618797). eprint: <https://doi.org/10.1021/es0618797>. URL: <https://doi.org/10.1021/es0618797>.
- [53] Usha Satish et al. "Is CO₂ an Indoor Pollutant? Direct Effects of Low-to-Moderate CO₂ Concentrations on Human Decision-Making Performance". In: *Environmental Health Perspectives* 120.12 (2012), pp. 1671–1677. DOI: [10.1289/ehp.1104789](https://doi.org/10.1289/ehp.1104789). eprint: <https://ehp.niehs.nih.gov/doi/pdf/10.1289/ehp.1104789>. URL: <https://ehp.niehs.nih.gov/doi/abs/10.1289/ehp.1104789>.
- [54] American Society of Heating Refrigeration and Air-Conditioning Engineers. *ANSI/ASHRAE Standard 62.1–2016 - Ventilation for Acceptable Indoor Air Quality*. 2016.
- [55] D.H.E.H. Services et al. *NIOSH Pocket Guide to Chemical Hazards*. DHHS (NIOSH) Publication. CreateSpace Independent Publishing Platform, 2007. ISBN: 9781489501509. URL: <https://books.google.it/books?id=2A-8nAEACAAJ>.

REFERENCES

- [56] Luca Muratori et al. "Assessment of energy saving due to a flexible indoor air quality control". In: *2021 IEEE International Workshop on Metrology for Automotive (MetroAutomotive)*. 2021, pp. 175–180. DOI: [10.1109/MetroAutomotive50197.2021.9502848](https://doi.org/10.1109/MetroAutomotive50197.2021.9502848).
- [57] Leyan Pan et al. "Energy-saving effect of utilizing recirculated air in electric vehicle air conditioning system". In: *International Journal of Refrigeration* 102 (2019), pp. 122–129. ISSN: 0140-7007. DOI: <https://doi.org/10.1016/j.ijrefrig.2019.03.018>. URL: <https://www.sciencedirect.com/science/article/pii/S0140700719301173>.
- [58] Gen Pei et al. "Effect of sensor position on the performance of CO₂-based demand controlled ventilation". In: *Energy and Buildings* 202 (2019), p. 109358. ISSN: 0378-7788. DOI: <https://doi.org/10.1016/j.enbuild.2019.109358>. URL: <https://www.sciencedirect.com/science/article/pii/S0378778819305377>.
- [59] Luca Muratori et al. "Measurement methods and evaluation techniques of indoor CO₂ in a cabin for an electric crane". In: *2021 IEEE International Workshop on Metrology for Automotive (MetroAutomotive)*. 2021, pp. 163–168. DOI: [10.1109/MetroAutomotive50197.2021.9502887](https://doi.org/10.1109/MetroAutomotive50197.2021.9502887).
- [60] *ISO/IEC Guide 98-3/Suppl. 1:2008. Evaluation of Measurement Data – Supplement 1 to the Guide to the Expression of Uncertainty in Measurement – Propagation of Distributions Using a Monte Carlo Method*. Standard. Geneva, Switzerland: International Standardization Organization, 2008.
- [61] Luca Muratori et al. "Optimal Control of Air Conditioning Systems by Means of CO₂ Sensors in Electric Vehicles". In: *Sensors* 22.3 (2022). ISSN: 1424-8220. DOI: [10.3390/s22031190](https://doi.org/10.3390/s22031190). URL: <https://www.mdpi.com/1424-8220/22/3/1190>.
- [62] Heejung Jung. "Modeling CO₂ Concentrations in Vehicle Cabin". In: *SAE 2013 World Congress & Exhibition*. SAE International, Apr. 2013. DOI: <https://doi.org/10.4271/2013-01-1497>. URL: <https://doi.org/10.4271/2013-01-1497>.
- [63] Heejung S. Jung et al. "Simultaneously reducing CO₂ and particulate exposures via fractional recirculation of vehicle cabin air". In: *Atmospheric Environment* 160 (2017), pp. 77–88. ISSN: 1352-2310. DOI: <https://doi.org/10.1016/j.atmosenv.2017.04.030>.

- 10.1016/j.atmosenv.2017.04.014. URL: <https://www.sciencedirect.com/science/article/pii/S1352231017302522>.
- [64] *Sensirion*. <https://www.sensirion.com/en/>. Accessed: 11-Oct-2023.
- [65] *Telaire | CO₂, Humidity & Dust Sensors*. <https://www.amphenol-sensors.com/en/telaire/co2>. Accessed: 11-Oct-2023.
- [66] Jane Hodgkinson et al. "Non-dispersive infra-red (NDIR) measurement of carbon dioxide at 4.2m in a compact and optically efficient sensor". In: *Sensors and Actuators B: Chemical* 186 (2013), pp. 580–588. ISSN: 0925-4005. DOI: <https://doi.org/10.1016/j.snb.2013.06.006>. URL: <https://www.sciencedirect.com/science/article/pii/S0925400513006862>.
- [67] *VDV-Schrift, Nr. 236. Air Conditioning of Buses of the Classes I (Urban Bus) and II (Suburban Bus), for Conventional Diesel and Gas Buses as Well as for Hybrid, Fuel Cell and Electric Buses*. Standard. Berlin, Germany: Verband Deutscher Verkehrsunternehmen e.V., Nov. 2018.
- [68] *ISO/IEC Guide 98-3:2008; Uncertainty of Measurement—Part 3: Guide to the Expression of Uncertainty in Measurement (GUM:1995)*. Standard. Geneva, Switzerland: International Standardization Organization, 2008.
- [69] Jing Ma et al. "Experimental study on the performance of vehicle integrated thermal management system for pure electric vehicles". In: *Energy Conversion and Management* 253 (2022), p. 115183. ISSN: 0196-8904. DOI: <https://doi.org/10.1016/j.enconman.2021.115183>.
- [70] Zhen Tian et al. "Investigation on an integrated thermal management system with battery cooling and motor waste heat recovery for electric vehicle". In: *Applied Thermal Engineering* 136 (2018), pp. 16–27. ISSN: 1359-4311. DOI: <https://doi.org/10.1016/j.applthermaleng.2018.02.093>.
- [71] Zhen Tian and Bo Gu. "Analyses of an integrated thermal management system for electric vehicles". In: *International Journal of Energy Research* 43.11 (2019), pp. 5788–5802. DOI: <https://doi.org/10.1002/er.4679>. eprint: <https://onlinelibrary.wiley.com/doi/pdf/10.1002/er.4679>.
- [72] Tibor Kiss, Jason Lustbader, and Daniel Leighton. "Modeling of an Electric Vehicle Thermal Management System in MATLAB/Simulink". In: *SAE 2015 World Congress & Exhibition*. SAE International, Apr. 2015. DOI: <https://doi.org/10.4271/2015-01-1708>.

REFERENCES

- [73] Monica Tutuianu et al. “Development of the World-wide harmonized Light duty Test Cycle (WLTC) and a possible pathway for its introduction in the European legislation”. In: *Transportation Research Part D: Transport and Environment* 40 (2015), pp. 61–75. ISSN: 1361-9209. DOI: <https://doi.org/10.1016/j.trd.2015.07.011>.
- [74] Luca Muratori et al. “A vehicle integrated thermal management system for electric busses”. In: *2022 IEEE International Workshop on Metrology for Automotive (MetroAutomotive)*. 2022, pp. 139–144. DOI: [10.1109/MetroAutomotive54295.2022.9855156](https://doi.org/10.1109/MetroAutomotive54295.2022.9855156).
- [75] Dominik Dvorak, Daniele Basciotti, and Imre Gellai. “Demand-Based Control Design for Efficient Heat Pump Operation of Electric Vehicles”. In: *Energies* 13.20 (2020). ISSN: 1996-1073. DOI: [10.3390/en13205440](https://doi.org/10.3390/en13205440).
- [76] Ian H. Bell et al. “Pure and Pseudo-pure Fluid Thermophysical Property Evaluation and the Open-Source Thermophysical Property Library CoolProp”. In: *Industrial & Engineering Chemistry Research* 53.6 (2014). PMID: 24623957, pp. 2498–2508. DOI: [10.1021/ie4033999](https://doi.org/10.1021/ie4033999).
- [77] F. P. Incropera et al. *Fundamentals of Heat and Mass Transfer – 6th Edition*. 111 River St, Hoboken, NJ 07030: John Wiley & Sons, Inc., 2007.

Acknowledgments

Ringrazio di cuore il Prof. Peretto, la Prof.ssa Pulvirenti e la Prof.ssa Di Sante per avermi offerto l'opportunità di intraprendere il percorso del dottorato e per avermi guidato con pazienza e competenza lungo questo cammino di crescita personale e professionale. Un ringraziamento speciale va anche a Webasto Thermo & Comfort Italy s.r.l. per il loro sostegno e contributo al mio percorso accademico. Sono grato a tutti voi per la fiducia, il supporto e l'ispirazione che mi avete donato.

Ringrazio inoltre la mia famiglia per il costante sostegno, l'amore incondizionato e la comprensione durante tutto il mio percorso accademico. Senza il vostro incoraggiamento e il vostro affetto, non avrei potuto raggiungere questo importante traguardo. Siete stati la mia fonte di forza e di motivazione in ogni momento.

Ringrazio calorosamente i dipendenti di Webasto, in particolare Giovanni e Federico, per il loro prezioso supporto tecnico e morale durante il mio percorso. La vostra competenza e disponibilità sono state fondamentali per affrontare le sfide e superare gli ostacoli. È stato un privilegio poter stringere con voi un legame di amicizia così significativo, che ha reso il mio tempo in Webasto un'esperienza ancora più gratificante. Vi sono profondamente grato anche per avermi accompagnato personalmente nei primi giorni a Gilching e per avermi presentato al nuovo team di colleghi con cui ho poi collaborato. La vostra gentilezza e accoglienza hanno reso il mio ingresso nell'ambiente lavorativo molto più agevole e piacevole. Grazie di cuore per tutto.

Infine, desidero esprimere un sentito ringraziamento ai miei amici e colleghi dottorandi. La vostra preziosa presenza e il vostro sostegno reciproco hanno reso il percorso del dottorato un'esperienza ancor più ricca e significativa. Grazie per le lunghe ore trascorse insieme a discutere di ricerca, per gli incoraggiamenti nei momenti di difficoltà e per le risate condivise che hanno reso più leggero il

REFERENCES

peso degli impegni accademici. Indimenticabili sono state anche le conferenze a cui abbiamo partecipato insieme, momento in cui non solo abbiamo arricchito le nostre conoscenze, ma abbiamo anche condiviso momenti di gioia.